UTILIZATION OF INTERDIGITATED MICROELECTRODES AND DIELECTROPHORESIS FOR BIOSENSING, BIO MOLECULE MANIPULATION AND BIOMANUFACTURING THERAPEUTIC CELLS

A Dissertation
Submitted to the Graduate Faculty
of the
North Dakota State University
of Agriculture and Applied Science

By

Vidura Dhananjaya Jayasooriya

In Partial Fulfillment of the Requirements
for the Degree of
DOCTOR OF PHILOSOPHY

Major Department:
Electrical and Computer Engineering

July 2020

Fargo, North Dakota

North Dakota State University
Graduate School

Title

UTILIZATION OF INTERDIGITATED MICROELECTRODES AND DIELECTROPHORESIS FOR BIOSENSING, BIO MOLECULE MANIPULATION AND BIOMANUFACTURING THERAPEUTIC CELLS

By

Vidura Dhananjaya Jayasooriya

The Supervisory Committee certifies that this ***disquisition*** complies with North Dakota State University's regulations and meets the accepted standards for the degree of

DOCTOR OF PHILOSOPHY

SUPERVISORY COMMITTEE:

Dr. Dharmakeerthi Nawarathna
Chair

Dr. Ivan T. Lima

Dr. Benjamin Braaten

Dr. Halis Simsek

Approved:

08/07/2020
Date

Dr. Benjamin Braaten
Department Chair

ABSTRACT

Microelectrode arrays (MEA) and microfluidic systems are two of the most used technologies in Lab-on-a-chip (LOC) applications. These integrated and miniaturized systems are said to offer significant advantages in medical applications due to their high sensitivity, high throughput, lower material consumption, low cost, and enhanced Spatio-temporal control. Further, the physical laws at the micro-scale offer certain advantages in terms of the control of physical, biological and chemical properties in diagnostics or therapeutics at the cellular or molecular level. Moreover, these platforms are portable and can be easily designed for point-of-care diagnostics. Unfortunately, among various microelectrode and microfluidic technologies available today, only a few have been proven to be useful in clinical applications. One of the reasons behind this issue is the lack of efficient and sensitive methods to integrate the handling of biological materials in microfluidic devices. This has created a gap between real-world clinical applications and this emerging technology.

To address this issue, in this work, externally applied electric fields have integrated with MEA and microfluidics systems. Moreover, this work has centered on dielectrophoresis, which is a result of the interaction between biological materials (e.g., DNA, RNA and cells) and external electric fields. Dielectrophoretic force (DEP force) was used to selectively manipulate biological materials within microfluidics devices. This capability opened up avenues for biosensing and biomanufacturing. This work was organized in the following manner: first, we investigated the production of DEP force, selectivity and limits. Second, the new knowledge learned from dielectrophoresis experiments was used to develop novel biomarker sensing technologies or sensors. Third, dielectrophoretic cell purification methods needed for the production of safe chimeric antigen receptor (CAR) T-cells for treating cancer, was investigated. Finally, a novel

method for the manufacturing of viral vector-free CAR T-cells was developed. Results from these studies have shown that integration dielectrophoresis with MEA and microfluidics provides a new class of tools for unmet needs in clinical applications. Finally, fundamental studies on dielectrophoresis provide new insights into its origin and limits. Developed technologies could be used in clinical applications after validation.

ACKNOWLEDGEMENTS

At the outset, I would like to thank my advisor, Dr. Dharmakeerthi Nawarathna, for providing me the concept of this research as well as for the constant supervision and excellent guidance. I am also grateful for the exemplary mentorship that he provided, which has a very positive influence on my life and career.

Further, I would like to acknowledge my committee members, Dr. Ivan Lima, Dr. Benjamin Braaten and Dr. Halis Simsek, for their valuable inputs and goodwill.

I would also like to thank the NDSU Graduate School and the Department of Electrical and Computer Engineering, for providing me with a platform to showcase my skills.

I would not have been able to achieve my targets without the support of many individuals and organizations. I convey my gratitude to all those parties, who helped me in many ways to be successful in this journey.

DEDICATION

I dedicate this Ph.D. dissertation to my dearest parents,

Dhammika Singhesena and Premalatha Wijerathna

for their prayers of day and night, which provided me the most essential good luck and guidance to complete this hard journey;

To my beloved wife,

Heshani Mahalaksha,

for her affection, love, encouragement and patience which enabled me to get this honor.

TABLE OF CONTENTS

LIST OF TABLES

LIST OF FIGURES

CHAPTER 1. INTRODUCTION

1.1. Overview

Miniaturization of traditional technologies has shown significant advantages over the macro scale devices in different fields of engineering [1]–[3]. Since the attempts of miniaturizing the transistor technologies in the late 1960s, microfabrication technologies have gained rapid growth [1],[4],[5]. Along with evolving microfabrication techniques, the healthcare sector was one of the first industries to demand miniaturization. Medical device designers in the healthcare industry have been interested in utilizing these miniaturization techniques in the bulk medical apparatus, which have many drawbacks such as high-power consumption, low speed of action, non-portability and difficulties in handling on certain occasions. These efforts for a few decades have resulted in devices with added functionality than the conventional apparatus. Modern implantable pace-makers, Apple watch with ECG recording and handheld PCR machines are few of the examples of advances of the medical devices with miniaturization technologies.

As a result of the driving force of miniaturization, micro-fluidics and micro-electrodes systems were introduced as a biological tool to replace the bulk equipment used in the biochemical analysis in the early 1990s [6],[7]. During the last decade, this micro-electrode and micro-fluidic based technology evolved from focusing just on replacing the existing bulk conventional instruments, into the innovation of novel integrated devices in the healthcare sector to perform different tasks together to do combined processes [1],[5],[8]. These integrated systems are called “lab on a chip” (LOC) systems as it replicates a set of integrated, expensive bench-top laboratory instruments with just a microchip. These are designed to perform different processes such as biomolecule manipulations, sample delivery, cell sorting or simulating on-chip reactions, which can be useful in diagnostic and therapeutic applications [1],[7],[9].

Many techniques like filtration, centrifugation, magnetic fields, acoustic forces, chromatography, electrophoresis, or dielectrophoresis (DEP) are used in these LOC devices. Compared to other technologies used in these devices, DEP can be considered as one of the most significant techniques. This is because it integrates easily with any other LOC technique, in terms of speed, efficiency, sensitivity, selectivity, and most importantly with it's a label-free nature in manipulating particles [10],[11]. This report describes the studies that have been conducted to explore the utilization of DEP, along with the micro-electrode and micro-fluidic technologies to solve some of the unmet practical needs in biosensors, biomolecule manipulation and biomanufacturing cells for therapy.

1.2. Dielectrophoresis

Dielectric materials are electrical insulator materials that can be polarized by an externally applied electric field [12],[13]. Once a dielectric material is placed in an external electric field, charges shift slightly from the equilibrium position, rather than freely passing through the material [12],[14]. These shifted charges cause the material to be polarized and produce electric dipoles [15]–[19]. Dielectrophoresis (DEP) is a phenomenon that explains the relative motion of these dielectric particles in a liquid medium, resulting from polarization forces produced by inhomogeneous electric fields [20]–[23]. Since biological entities like cells, tissues, nucleic acids (DNAs, RNAs, etc.) are made of dielectric materials, DEP has been identified as a promising technology for bioparticle manipulation with the advantages of strong controllability, easy operation, high efficiency and slight damage to biological targets [24]–[26]. In recent years, DEP has made great development in the medical field collectively with micro-engineering technology [27],[28].

1.2.1. Theory of dielectrophoresis

Mathematically, the time-averaged DEP force acting on a spherical particle in a non-uniform AC electric field can be represented by

$$F_{DEP} = \frac{1}{2}\alpha \nabla(E^2) \tag{1.1}$$

where α is the polarizability of the dielectric particle, ∇ is the vector operator, and E is the RMS electric field [29]–[32]:

$$\alpha = 4\pi\varepsilon_m r^3 \boldsymbol{Re}\{f_{CM}(\omega)\} \tag{1.2}$$

where r is the radius of the spherical particle, ε_m is the suspending medium permittivity, ω is the frequency of the applied electric field, and $\boldsymbol{Re}\{f_{CM}(\omega)\}$ the real part of the Clausius-Mossotti(CM) factor defined as:

$$f_{CM}(\omega) = (\varepsilon_p^* - \varepsilon_m^*)/(\varepsilon_p^* + 2\varepsilon_m^*), \tag{1.3}$$

where ε_p^* is the complex permittivity of the particle and ε_m^* is the complex permittivity of the suspending medium [31]–[34]. The complex permittivity is given by $\varepsilon^* = \varepsilon - j(\frac{\sigma}{\omega})$ with σ being the real conductivity, ε being the real permittivity, and ω being the frequency [31]–[33]. The real part of the CM factor is theoretically bounded between -1/2 and 1, which determines the direction and the relative strength of the DEP force [35],[36]. If the magnitude of $\boldsymbol{Re}\{f_{CM}(\omega)\}$ is negative, then the particles move towards the lowest field strength region (negative DEP). If the magnitude of $\boldsymbol{Re}\{f_{CM}(\omega)\}$ is positive, the particles are repelled from the lowest field strength region and move to regions of the highest field strength (positive DEP) [37],[38]. Figure 1.1 shows how to manipulate particles using positive and negative DEP with different electrode configurations.

According to equations (1.1), (1.2) and (1.3), the DEP force exerted on a particle depends on its dielectric parameters (conductivity and the permittivity). Since these parameters are functions of the applied electric field, the CM factor varies distinctively for different types of

particles. This enables us to distinctively sort particles using DEP by changing the frequency of the applied electric field. The magnitude of the DEP force exerted on the particle depends on the size of the particle and the shape of the particle. Therefore, in certain instances, DEP is used to distinguish between particles of different sizes.

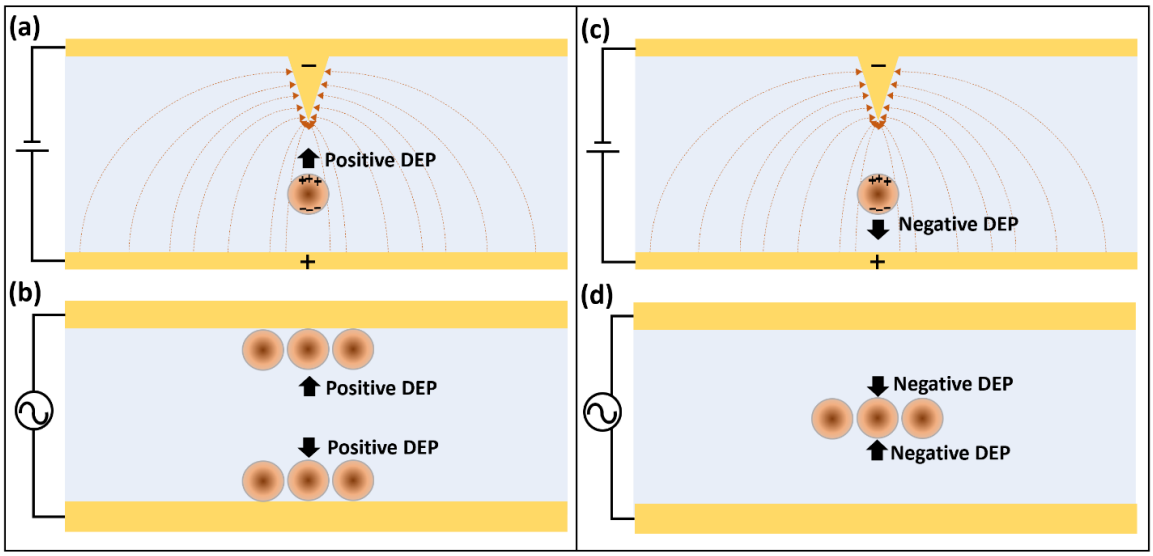

Figure 1.1. Different electrode configurations to manipulate particles using dielectrophoresis. (a) An electrode configuration to attract particles towards a tip using DC electric field, (b) an electrode configuration to attract particles to edges of planar electrodes using AC or DC electric fields, (c) an electrode configuration to repel particles away from a tip using DC electric field, (d) an electrode configuration to repel particles away from planar electrodes and concentrate in the center using AC or DC electric fields.

Due to the capability of selectively manipulating particles based on the dielectrophoretic properties using DEP, it has been used in various medical applications. Initially, DEP studies were conducted on cells to understand the physicochemical properties of cells by observing how cells are responding to DEP force [23],[36],[39],[40]. Since then, DEP has been used in various cellular applications including cell sorting [23],[36], cell patterning in tissue engineering applications [41]–[43] and separation of cell types from a cellular mixture [44]–[46]. Both Positive DEP and Negative DEP are being used in these cellular applications [10],[47],[48]. In positive DEP applications, a selected frequency is applied to the cell samples, where the cells are trapped in the

electrodes. The non-target particles are repelled from the electrodes with negative DEP [49],[50], or combined with microfluidics to be pushed away from electrodes using viscous drag force [51],[52]. The negative DEP applications are mostly used in patterning applications, where specially designed electrodes made with different configurations are used to make nice patterns of cells in between electrodes [43],[53].

Additionally, DEP is used in some applications for detection and biosensing systems, as DEP can be used in separation and concentration of specific biomolecules (DNA, RNA, or proteins) for downstream laboratory analysis [23],[54]. Many detection techniques are based on the immobilization of target biomolecules using proper probes on the sensor surface for detection [54],[55]. Most of these techniques suffer from insufficient molecular interaction due to the low concentration of biological particles in the sample and current state of art technologies have detection limits only in pM range or above [54],[56]. DEP can be utilized as an important component of such devices to selectively concentrate the desired biological particle and increase the local concentration of target particles [54],[57]. Therefore, vital parameters for sensing and detection like sensitivity, specificity and limit of detection can be significantly enhanced by combining DEP with other detection methods [54],[57].

1.3. Research objectives

This dissertation research was conducted by exploring a few potential applications of utilizing the MEAs and DEP in diagnosis as well as therapeutics related biomedical applications to achieve three objectives.

1. To investigate quantitative measurements of DEP and insulator-based DEP technologies for biomolecule manipulation.

2. To develop a potential impedimetric based biosensor technology to be used at the point of care settings for diagnostics purposes.
3. To develop a non-viral, personalized, low-cost CAR T-cell manufacturing methodology with an enhanced CAR-expressing period.
4. To develop a label-free purification technique to remove dead cells from an electroporated cell sample.
5. To develop a methodology to high purity isolation of primary T-cells in samples contaminated with leukemia cells, for biomanufacturing of therapeutic car T-cells.

1.3.1. To investigate quantitative measurements of DEP and insulator-based DEP technologies to biomolecule manipulation

Even though DEP is used widely, quantification methods of measuring DEP force on individual particles are lacking [58],[59]. Still, there is no standard method used in measuring the DEP force and most of the experiments are being conducted based on simulation based approximations [59]. These measurements are a necessity to assess the dominance of DEP among the competitive forces in micro-scale to be used in biomolecular applications. The viscous drag force, Brownian forces, and hydrodynamic forces are governing the movements of biomolecules in a free or flowing solution [15],[60]. Therefore, to effectively use DEP to manipulate, trap, or separate biomolecules in desired high or low electric field gradient areas, one must overcome all these forces. As such, quantitative measurements of DEP force would help to design the nano-electronic devices as well as tune the operating parameters to achieve strong DEP force. The design parameters include the electrode shapes, gap between electrodes and electrode height, which determines the magnitude and the span of the DEP force to effectively manipulate target biomolecules in the desired manner.

To address the issue, we report on the use of atomic force microscopy (AFM) for analysis of the DEP force and the span of DEP force in a conventional interdigitated microelectrode array (MEA). A non-contact, dynamic AC lift-mode AFM method similar to the typical electric or magnetic force measurement methods was used in investigating the DEP force exerted on AFM probe tip[61],[62]. The capability of precise movement of the AFM probe tip was then utilized in mapping out the force variation along the vertical direction to investigate the span of the DEP force.

Upon investigating the conventional DEP force, we investigated insulator-based dielectrophoresis (iDEP) which is an alternative method of carrying out DEP [63],[64]. In iDEP, an electric field is applied using two electrodes with insulator constrictions/structures in the middle, blocking the regular electric field lines [63],[65]. These distorted electric field lines create regions of higher and lower field strength near the edges of the insulator structures [66],[67]. iDEP systems are becoming popular because of less fouling effects like electrolysis and biomolecule degradation at insulator edges, which makes them more suitable for biological applications[64],[68]. We report an investigation on a novel approach to use micro manufactured glass needles and a conventional MEA to generate iDEP which allows us to selectively trap and manipulate DNA fragments and nanoparticles.

1.3.2. To develop a potential impedimetric based biosensor technology to be used at the point-of-care-settings for diagnostics purposes

According to the World Health Organization, “biomarker” stands for any substance, structure, or process that can be measured in the body or its products and influence or predict the incidence of outcome or disease [69]. Among biomarker categories, proteins, DNAs, RNAs and miRNAs, which are usually containing in blood, saliva, serum, or tissue, can be used as an effective

pointer of any disease states. Biosensors are commonly used to quantify these disease states [70]–[73]. In particular, quantification of biomarkers that are related to disease states are important because they can detect infections and other diseases such as cancer, myocardial infarction or schizophrenia [74]–[76].

To this end, the enzyme-linked immunosorbent assay (ELISA) is the gold standard for detecting and quantifying biomarker proteins [77]. ELISA has a minimum detection limit of 250 pg of target biomarkers in 1 mL of a sample [78]. This detection limit is not sufficient for many cancers, especially in the early stages of tumor development. The popular nucleic acid molecules detection method in the diagnosis field is quantitative real-time polymerase chain reaction (qRT-PCR) [79],[80]. This method is time-consuming (>7 hours), requires stable genes and safe handling, which requires highly trained labor. Further, the reported detection limits are above the pM range, which is not sufficient in the detection of many cancers [79],[81],[82] and it is necessary to detect and quantify biomarkers much lower than the current limit [74].

To address this issue, several other methods have been proposed and tested [79],[83],[84]. Among the techniques that are proposed for biomolecule detection in clinical settings, electrical impedance-based biosensing (biomarker detection) can be identified as a low-cost, label-free and highly-sensitive technique [85]–[87]. We report a study conducted on utilizing conventional MEAs to be utilized in impedimetric biosensing to detect proteins in a label-free manner that resulted in a better detection limit (0.25fM detection limit) compared with current technologies. The report further discusses the design considerations of MEAs for a higher sensitive and accurate quantification. Then, another study was conducted to enhance the capabilities of the conventional MEA-based impedimetric using DEP. Utilizing DEP enabled detecting and quantifying both nucleic acids and proteins (antigen-antibody) complexes using the same MEA device, with less

processing steps and less processing time. The capabilities of the technology reported a competitive detection level (75fM for nucleic acids and 84fM for antigen-antibody complexes), with the potential to be used at the point-of-care settings.

1.3.3. To develop a non-viral, personalized, low-cost CAR T-cell manufacturing methodology with an enhanced CAR-expressing period.

Cancer has been one of the leading causes of death all around the world [88],[89]. The American cancer society has predicted 1.8 million new cancer cases and 606,520 cancer deaths in the United States in 2020 [88],[90]. Numerous treatment methods have been used since the 18th century in treating cancer including, surgery, radiotherapy, cytotoxic chemotherapy and molecularly targeted therapy [91]–[93]. Those have been called the four pillars of cancer therapy, and recently the fifth pillar of cancer therapy was introduced, which is immunotherapy [94]–[96].

In immunotherapy, unlike other treatment methods that use external drugs or tools to fight cancers, a patient's immune system is modified or strengthened to fight cancers. So far, many of the cancer immunotherapy methods have been utilized effectively, including immune checkpoint inhibitors, monoclonal antibodies, treatment vaccines, immune system modulators, and cell-based therapies [97]–[99]. Among all the immunotherapies, cell-based therapies, especially adoptive cell therapy, has shown a promising pathway in treating cancer [100]–[102].

Adoptive T-cell has gained attention in treating cancer. Out of the available methods used in adoptive cell therapy, CAR (chimeric antigen receptor) has emerged as a powerful therapeutic method, with evident striking responses in treating acute lymphoblastic leukemia (ALL) and diffuse large B-cell lymphoma (DLBCL) [103]–[105]. Today, these therapies are improving consistently and are being used alone and in combination with other cancer treatment methods [101],[106],[107]. Currently, two of these CAR T-cell therapies, called KYMRIAH and

YESCARTA targeting CD19 antigen on cancer cells, have been approved by the Food and Drug Administration (FDA), to be used in clinical settings [108]–[110]. CARs are a type of molecule that combines antibody-based specificity for tumor-associated surface antigens with T-cell receptor-activating intracellular domains, which demonstrate specific antitumor cellular immune activity [111]–[113]. These CARs allow a T-cell to achieve major histocompatibility complex (MHC)–independent primary activation through single-chain variable fragment (scFv) antigen-specific extracellular regions [114],[115]. These regions are fused to intracellular domains that provide T-cell activation and costimulatory signals [111]–[113].

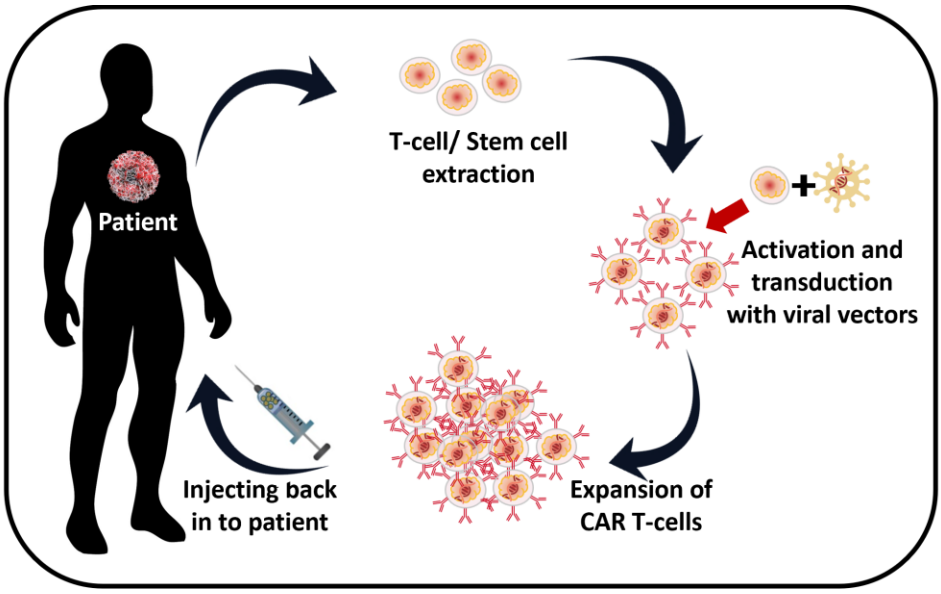

Figure 1.2 The CAR T-cell manufacturing process using viral vectors.

Both, FDA approved treatment technologies are used in certain types of B cell lymphomas. CD19 is a B-cell surface protein expressed during B-cell development which is expressed on almost all B-cell malignancies. Chronic lymphocytic leukemia (CLL), ALL, and many non-Hodgkin lymphomas are few of the diseases associated with these B cell malignancies [103],[105],[116]. This near-universal expression and specificity for a single cell lineage have made CD19 an attractive target for CAR-modified T-cell therapies for B cell malignancies

[103],[105],[116]. Treatments conducted with CAR T-cells targeting B-cell specific antigen CD19 have reported a higher complete remission rate like 90% in children and adults with relapsed and refractory ALL [104]. Additional B-cell–specific cell-surface molecules, such as CD22, may hold similar promise and are under active investigations [104],[116].

The most widely used gene transfer method in delivering these CAR genes is using viral vector-based transduction as shown in Figure 1.2 [117]–[120]. Retroviruses or HIV derived lentiviruses are the most used types of vectors which has proven successful transfer [111],[121]. Also, the vector treated CAR T-cells have long term expression of CAR across multiple cell cycles [122],[123]. Both FDA approved KYMRIAH and YESCARTA methods use viral vectors [124],[125]. These treatments cannot be afforded by many, as the cost per treatment lies within $373,000-475,000 range as in May 2019 [106]. In addition, despite being used in clinical settings, viral vectors have issues due to permanent genetic modifications incurring on cells [117],[118],[122]. There are reports which indicate the risk of insertional mutagenesis, which has been observed during the trials for severe combined immunodeficiency and wiskott-aldrich syndrome, that is treated using transduced viral vectors to hematopoietic stem cells [122],[126],[127]. As per the most recent reports, the cytokine release syndrome (CRS) has been identified as one of the major side effects of using viral vectors. In CRS, over-activated T-cells are said to increase cytokine production by the native immune system [122],[128],[129]. This excessive cytokine production can result in even organ failures and death [122],[128],[129].

Considering the facts, a great effort has been made to develop non-viral methods for gene transfer into molecules. Out of these efforts, electroporation mediated mRNA transfection has emerged as one of the potential approaches that have successfully demonstrated antitumor activity [117],[130]. In vitro transcribed (IVT) mRNA encoding, CAR molecules are being used in this

method and the synthesis details are mentioned elsewhere [131],[132]. These mRNAs offer huge advantages in cost for transfection and can be done within a few thousands of dollars. Also, the transient nature of these mRNA mitigates the risk of permanent cell modification and T-cell activity [101],[133]. Although the transient nature of the mRNA addresses the huge downfall of the viral-based method that increases the chance for CRS, a patient has to go through several blood infusions during the treatment when mRNA is used [122],[134]. Also, due to the novel approaches in expanding CAR T-cell therapy to be used in solid tumor based therapies [114],[135], this mRNA transfected cells get exhausted quickly due to their transient nature [122]. Therefore, mRNA base CAR T-cell therapy is still not a popular choice in clinical settings.

Several studies have been conducted to improve the lifetime of CAR expression on tumor cells, which include adding modifications to the mRNA structure to last longer [136],[137], or having more controlled delivery through transfection. There are reports which show that the amount of initial transfected genes can determine the lifetime of the CAR expression [123]. Thus, if we could transfect more mRNA into cells in a controllable manner, it will be a big step towards the mRNA-based CAR T-cells to be used in clinical settings as an affordable and safe therapeutic. However conventional electroporation methods used for mRNA transfection do not possess the capability of controlled mRNA injection. Also, those methods report a very low throughput (30%-40% out of cells used), high cell death (60%-70% out of cells used) and inefficient transfection (20%-30%) [110],[138],[139].

To address these issues, here we report a microelectrode array-based miniaturized technology utilized with DEP, for controllable and effective electroporation. The technology was successfully utilized in CAR mRNA transfection. Results show an improved transfection

efficiency, controllable transfection, improved CAR-expressing time, faster target cell lysing, and higher viability, upon electroporation, over the conventional methods.

1.3.4. To develop a label-free purification technique to remove dead cells from an electroporated cell sample

As mentioned in the above section 1.3.3, existing mRNA electroporation methods produce about 60%-70% of dead T-cells during the CAR T-cell engineering process [110],[138],[139]. Recently, it has been found that these dead or dying cells not only reduce the yield of the engineered T-cell sample but also can cause serious complications by interacting with live cells and tissues [140],[141]. The compensatory proliferation and rapid stem cell differentiation are two of the examples [140],[141]. Compensatory proliferation is a process that dead cells can stimulate the proliferation of adjacent cells, which eventually can lead to enhanced growth of tumor cells [140]. There are reports that the mitogens released by the dead cells can cause stem cell differentiation and become cancer cells [141]. The effects of the above-mentioned issues will not only contribute to the rapid growth of tumors but also can contribute to seeding metastases[140].

Therefore, It is an immense requirement to remove dead or dying cells from engineered CAR T-cell samples before infusing back into the patient. Although widely used cell purification methods like fluorescence-activated cell separation (FACS) and magnetic-activated cell separation (MACS) exist, they cannot be used in clinical settings for therapeutics [142],[143]. Both these methods have some issues; first, they need additional labels during the purifying steps, and these labels need to be completely removed from cells after they have been purified. Second, MACS requires magnetic labels, but there are no known labels that can be attached to cells that have died through necrosis. Finally, FACS is not approved by the FDA due to the possibility of cross-contamination with the fixed tubing [142],[143]. To address these critical issues, we have reported

a label-free cell purification method, combining microfluidics with DEP. In this method, when an electroporated cell sample flows through the microfluidic device, dead cells will be trapped in the device using positive DEP and the live cells can be collected at the outlet. The device was successfully utilized to obtain a purity (live cells) of ~99% at the output upon purification.

1.3.5. To develop a methodology to high purity isolation of primary T-cells in samples contaminated with leukemia cells, for biomanufacturing of therapeutic CAR T-cells

A recent clinical study has reported a male patient who suffered from B cell Acute Lymphoblastic Leukemia (B-ALL) relapsed after 9 months from his treatment of CD19-targeted CAR T-cell therapy in an eccentric manner [144]. According to the study, the patient was in complete remission on the 28 days post-infusion. But later, when the patient was checked on 252nd day post-infusion, an expanded B-cell population was observed. This B-cell population has shown the CAR antibody molecules on cell surfaces and has developed immunity to CAR T-cells [144]. In the study, it was found that the expression of the CAR antibody on B-cells was caused by unintentional introduction on the CAR gene into a single leukemic B-cell during T-cell manufacturing [144]. Eventually, it developed a secondary tumor and the patient died. The report from the clinical study claims that the mentioned case is a rare event, but still, it holds a great threat towards patients who go through CAR T-cell therapies without knowing the odds [144]. Therefore, it is evident that reliable cell purification methods are needed to prevent tumor cell contamination for effective CAR T-cell therapy.

Here, we report a DEP based microfluidic device to selectively trap contaminating cancer cells in isolated CD8 T cell samples from the blood. The microfluidic device we used in this study was the same as the study mentioned in section 1.3.5. Therefore, the purification using our method is label-free and can be utilized in clinical settings. In this method, DEP parameters and the flow

rates were fine-tuned to selectively trap contaminating large cancer cells from an isolated primary human T-cell sample. We were able to trap all the contaminating tumor cells in the device with 100% purity value. Therefore, this technology can be successfully utilized in addressing the issue of contaminating cells which can develop resistance against the CAR T-cell therapy.

CHAPTER 2. QUANTITATIVE MEASUREMENTS OF DIELECTROPHORESIS IN A NANOSCALE ELECTRODE ARRAY WITH AN ATOMIC FORCE MICROSCOPY[1]

Recent advances in biotechnology have allowed capturing individual biomolecules including disease-markers and cancer cells and monitoring their biological activities [43],[145]–[147]. The ultimate goal of this field would be to completely control and manipulate the biomolecules for practical diagnostic applications. Among a number of techniques developed for the detection and manipulation of biomolecules, Dielectrophoresis (DEP)-based methods have demonstrated the feasibility of a remote control of target molecules to trap and dissect for highly sensitive screening. For example, DEP has been used for the separation of yeast cells,[148]viruses,[149] and cancer cells [43],[150], as well as to trap particular DNA molecules [151],[152], providing tremendous potential in biomedical applications. In principle, DEP is a force exerted on a polarizable particle such as biomolecules and cells in the presence of nonuniform AC electric fields in liquid medium [38]. Depending on the dielectric responses of the particle and the surrounding medium, the external fields induce an effective dipole moment p on the particle and an instantaneous force F_{DEP} acting on the dipole [153],[154]. For the particle suspended in the non-uniform fields, the net force does not vanish. Thus, spatially asymmetric force due to the inhomogeneous field gradient in the medium drives the movement of the particle. In general, the force can be used to selectively attract (attractive F_{DEP}) or repel (repulsive F_{DEP}) biomolecules of interest from a complex medium to regions of strong electric fields. For example,

[1] The material presented in this chapter was co-authored by Froberg, J.; Jayasooriya, V.; You, S.; Nawarathna, D.; Choi, Y. Jayasooriya V. designed electrodes, defined the experimental conditions, participated in calculations, simulated the finite element models, co-drafted and revised all versions of this chapter. Reprinted with permission, from Froberg, J.; Jayasooriya, V.; You, S.; Nawarathna, D.; Choi, Y. Quantitative Measurements of Dielectrophoresis in a Nanoscale Electrode Array with an Atomic Force Microscopy. *Appl. Phys. Lett.* **2017**, *110* (20), 203701. https://doi.org/10.1063/1.4983785.)

cancer cells,[155] cellular components, and biomarkers [156],[157] can be collected, separated, concentrated, and transported using DEP-based micro-fluidic devices.

Although such non-invasive, non-contact DEP manipulation is a promising platform for biomedical applications, measuring and determining the strength of F_{DEP} on biomolecules in nano electronic devices are challenging problems. In addition, several issues associated with DEP limit its applicability in practice. First, the external AC field intensity and its frequency to generate bipolar DEP can cause unwanted electrochemical reactions such as water electrolysis at metal electrodes [151], destroying both the biological sample and the nano electronic devices. Second, F_{DEP} may not be uniformly distributed in the electrodes patterned on the devices due to the high sensitivity of the field variations near the sharp corners or edges of the electrodes at the nanoscale [158]. Effective solutions to the problems, on the other hand, would help to design the nanoelectronic device and tune the operating parameters to achieve strong F_{DEP} to effectively manipulate target biomolecules in a desired manner under physiological conditions.

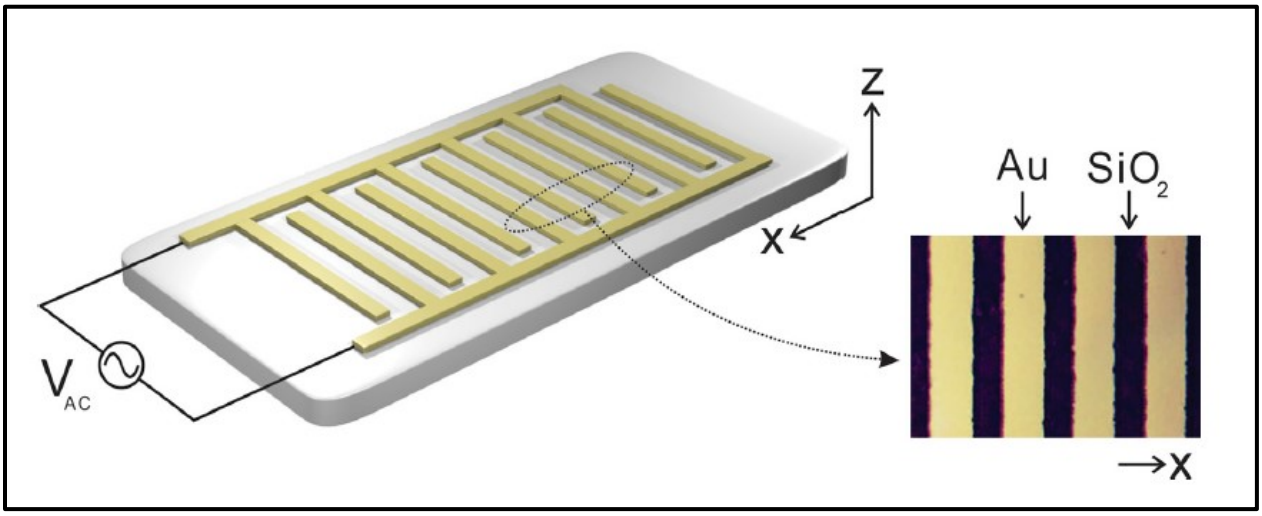

Figure 2.1. Schematic of an interdigitated metal (Au) electrode array connected to the AC voltage source.

Here, we show that F_{DEP} in the nanoelectronic devices can be experimentally measured and quantitatively evaluated by atomic force microscopy (AFM). A non-contact, dynamic AC lift-mode AFM method similar to the typical electric or magnetic force measurement methods [61],[62] as used to investigate the force between an AFM probe tip and the nanoelectronics devices including both the smooth surface and the sharp edges of electrodes. The measurements allowed mapping out the force variation along the direction (z) normal to the electrode surface in the device. In this work, the conventional interdigitated electrode array that has proven to be quite useful for dielectrophoretic separation and travelling wave dielectrophoresis in previous research studies [159],[160] was examined as shown in Figure 2.1 The device consists of planar metallic electrode arrays on a SiO_2 substrate. With a pre-patterned mylar mask, gold electrodes were defined by the standard optical lithography, similar to the previous study [161]. The width of electrodes, gaps between the electrodes, and the height of the electrodes were 16 μm, 10 μm, and 140 nm, respectively. Devices were mounted in a liquid-compatible commercial AFM (NT-MDT NTEGRA AFM), and the AFM imaging was performed in an ionic buffer solution without evaporation while measuring. Conventional silicon AFM probe tips without a coating (force constant: 2.7 N/m, Budget sensors) were used for the imaging. The external AC voltage between the two metal electrodes was applied by a commercial function/arbitrary waveform generator (Agilent 33220A), which was filtered and synchronized with the AFM scanning. A multi-pass scanning technique was employed for the precise measurements of both surface topography and the force gradient. The first-pass scanning was performed in the typical semi-contact mode to obtain the surface topography characteristics. During the second pass measuring the force gradient, the probe was raised above the surface at a distance z followed by the surface topography contour. Such lift-mode scanning in the second pass prevents any influence of surface features on the measurement. The

second-pass measurement depends solely on the force gradient along the z direction based on the point probe approximation assuming that the probe tip has a dipole moment located in the center of the tip end. The AC lift mode operates with a lock-in feedback loop to keep driving the probe oscillation at the nearly resonance frequency [61],[162]. When a force acts on the probe tip, it causes the resonance frequency of the tip to shift, depending on the force gradient and the direction. Additionally, such changes in resonance frequency result in an amplitude and phase shift. Thus, although the three parameters serve as an indicator of the force measurement, the force gradient is mainly detected by measuring the probe tip's phase vibration in the amplitude modulation mode using a simple lock-in amplifier. A mathematical relationship between the phase shift and the force gradient when $\partial F/\partial z$ is very small in magnitude compared to k is given by

$$\Delta\phi = \frac{Q}{k}\frac{\partial F}{\partial z} \tag{2.1}$$

where Q is the Q-factor of the resonance peak, k is the force constant of the probe tip, and $\partial F/\partial z$ is the force gradient in the direction normal to the surface [163],[164]. When $\partial F/\partial z$is measured according to z, F can be obtained by integrating $\partial F/\partial z$, For example, the negative shift of the measured phase corresponds to the attractive F and negative $\partial F/\partial z$ along the z direction. The AFM measurements were carried out in a phosphate buffer (1–10 μM KH_2PO_4, pH 7) at room temperature. The ionic strength of the buffer and the amplitude and frequency of the applied AC voltage were determined by the classical Maxwell-Wagner (MW) theory [38],[153]. Specifically, the complex Clausius-Mossotti (CM) factor depending on the complex permittivities of the particle and suspending medium and a depolarizing factor of the particle allow estimating the frequency dependent effective dipole moments of the particles as well as the magnitude and polarity of F_{DEP}.

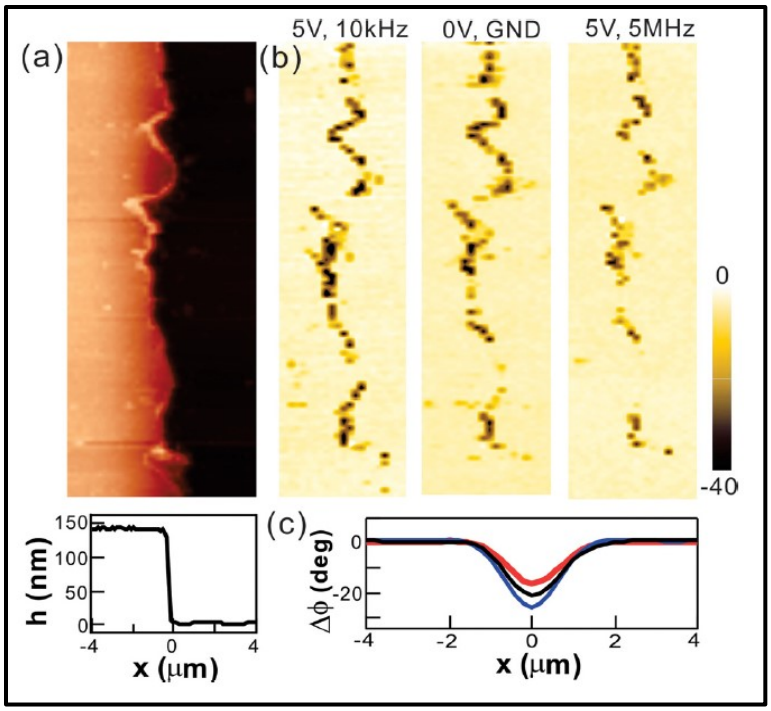

Figure 2.2. Multi-pass AFM measurements.
(a) A topography image of the metal electrode (red color) and the SiO_2 (black color) substrate and a height profile of line-cuts of the cross-section. (b) Phase images of (a) at three V_{ac} fields. (c) The averaged phase shifts along the electrode step edge. Blue, black, and red curves correspond to 10 kHz, GND, and 5MHz fields, respectively.

Figure 2.2 depicts typical multi-pass AFM images of the device in the absence and in the presence of the external AC fields (V_{ac}). Figure 2.2(a) presents a topography image and the corresponding height profile of the device acquired during the first-pass scanning, while the V_{ac} was in the off-mode. The metal electrodes and SiO_2 substrates were relatively flat and smooth compared to the sharp edge of the electrodes in the image. The edge line of the electrode is highly disordered at the nanoscale, producing additional non-uniform electric field distributions due to the lighting rod effects [153]. During the second-pass, lift-mode scanning at a particular z, a sinusoidal wave form of V_{ac} with a peak to peak potential of 5V is applied through the two electrodes (Figure 2.1) to examine the AC field effects. Figure 2.2 (b) shows the phase images of the same electrode [Figure 2.2 (a)] under three different conditions: V_{ac} (5 V_{pp}, 10 kHz); V_{ac} (0 V, GND); and V_{ac} (5 V_{pp}, 5MHz) at z.20 nm. In the control measurements performed without the

external AC field (V_{ac}.0 V), the phase shift was observed along the electrode edge direction. Such a phase shift is attributed to a geometry effect at the sharp step edge. When the AFM scans over the step edge, the distance z between the tip and the sample instantly decreases and brings the tip into a more negative force gradient until the feedback loop restores the initial distance z, [162] Therefore, the negative force gradient due to the attractive force variations is shown in the dark color phase image only at the edge. When the AC electric fields were applied with different frequencies, further phase shifts were observed as depicted in Figure 2.2(b). In the presence of V_{ac} (10 kHz), the features along the edge line in the phase image were unchanged, but their color was revealed to be darker, reflecting additional attractive forces acting on the AFM tip. Thus, the low frequency AC fields generated the attractive F_{DEP} and negative $\partial F_{DEP}/\partial z$. In contrast, repulsive F_{DEP} generated by the high frequency (5MHz) fields reduced the net force, resulting in the brighter edge line in Figure 2.2 (b). Figure 2.2 (c) compares the mean phase shift along the edge direction for each measurement. Taken together, the frequency dependent, binary F_{DEP} effects were able to be measured by our multi-pass AFM experiments.

To examine the spatial distribution of F_{DEP} and $\partial F_{DEP}/\partial z$ along the x and z directions, the AFM measurements were carried out by varying z across the electrodes with two fixed frequencies of 10 kHz (attractive F_{DEP}) and 5MHz (repulsive F_{DEP}). Figure 2.3 (a) displays pure $\partial F_{DEP}/\partial z$ components and their z dependence, where the background component without the AC fields was removed at each z. Both positive and negative $\partial F_{DEP}/\partial z$ peaked at the edge of the electrode (x=0) for all z. The magnitude of $\partial F_{DEP}/\partial z$ fell off along the x axis regardless of the sign of $\partial F_{DEP}/\partial z$ and z, suggesting the reduction in the field strength variations along the x axis. Finally, the magnitude of $\partial F_{DEP}/\partial z$ approached minimum values when the tip was away from the edge ($|x|>0$), indicating minimum points in the field strength at the top of the electrode and a point equidistant between

two electrodes. Such observations are in excellent agreement with the strong dependence of F_{DEP} on the strength of field gradients (F_{DEP}/rE_2).[153]

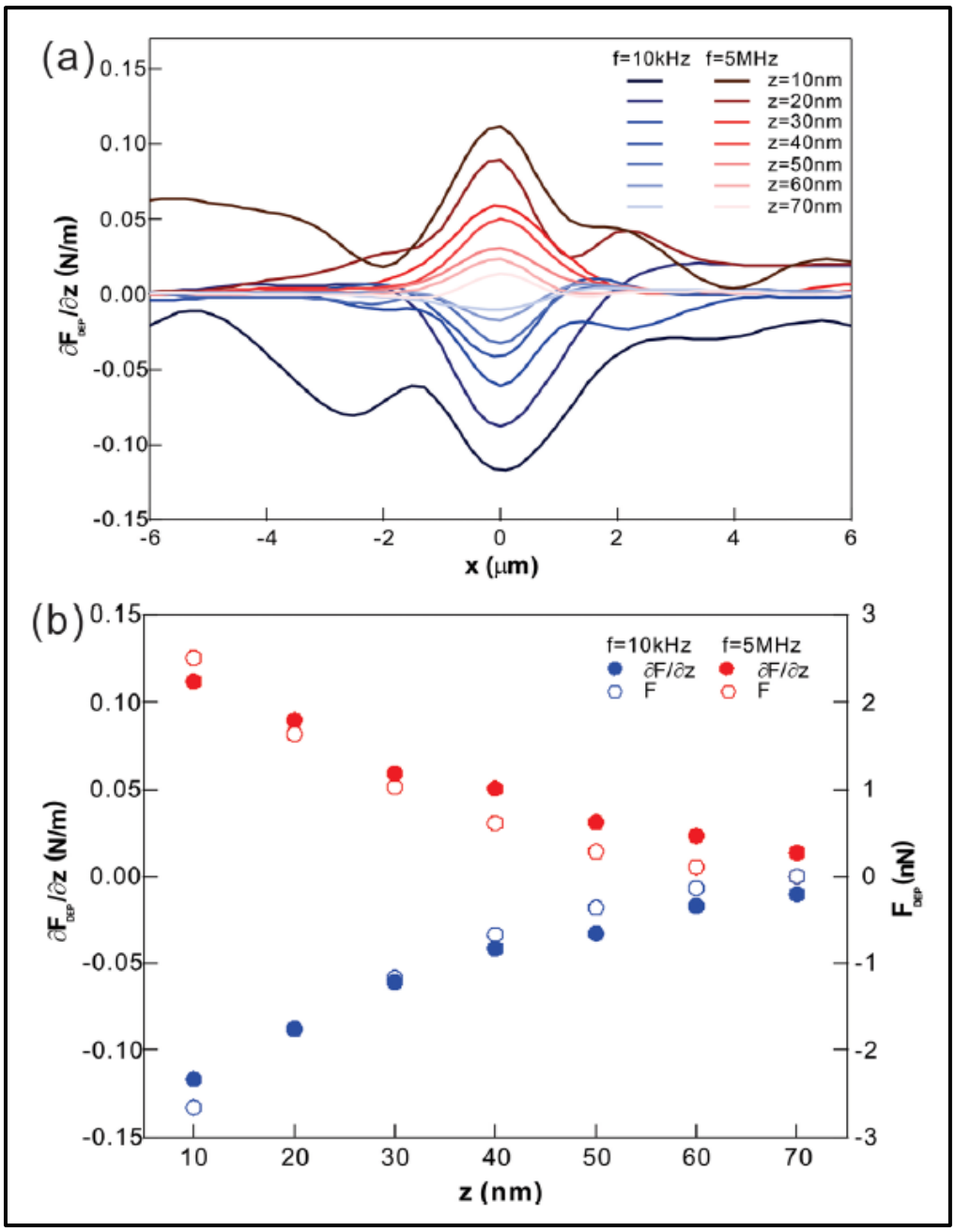

Figure 2.3. The spatial distribution of $\partial F_{DEP}/\partial z$.
(a) The average $\partial F_{DEP}/\partial z$ versus two driving (10 kHz and 5 MHz) frequencies, demonstrating attractive F_{DEP} with 10 kHz and repulsive F_{DEP} with 5 MHz (b) The average $\partial F_{DEP}/\partial z$ and F_{DEP} versus the separation distance z. F_{DEP} was obtained by integrating $\partial F_{DEP}/\partial z$.

Figure 2.3 (b) displays the peak values of $\partial F_{DEP}/\partial z$ and F_{DEP} calculated from the measured $\partial F_{DEP}/\partial z$ as a function of z [61]. The values were nonlinearly decreased upon increasing the separation distance z between the tip and the electrode edge. The shape of these curves suggests the non-linear changes in the intensity of the field gradient at the edge. Furthermore, the magnitude of F_{DEP} and $\partial F_{DEP}/\partial z$ was almost identical for two different frequencies at the same z. The results indicate that the CM factors for the low (10 kHz) and high (5 MHz) frequencies are nearly identical. When the tip was further away from the edge (>80 nm), F_{DEP} approached nearly zero, providing an upper limit for the working distance of the short-range F_{DEP}.

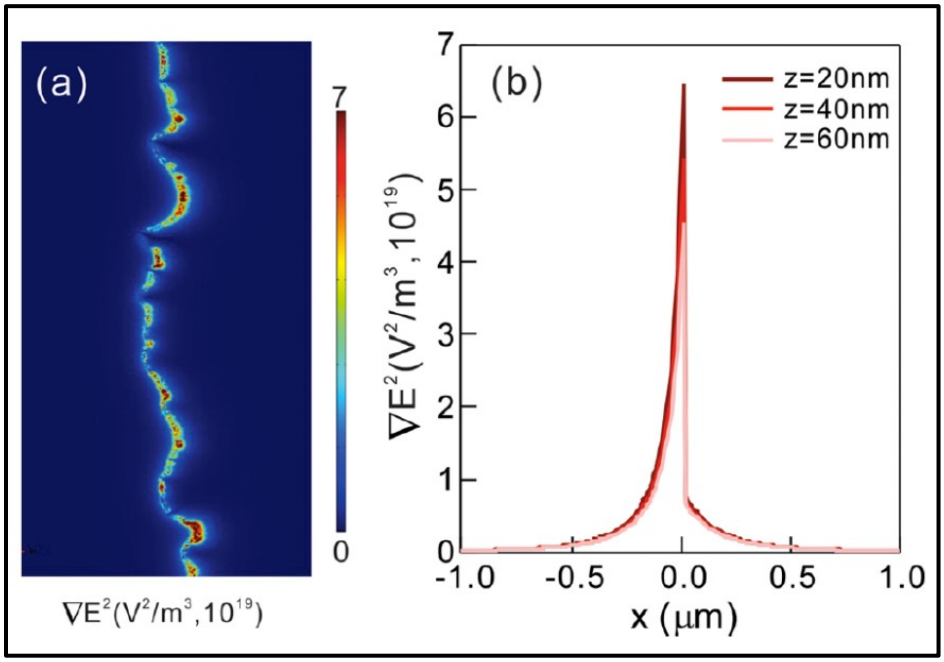

Figure 2.4. (a) A two-dimensional plot of the strength of the gradient fields and (b) its profile along the x direction at various z values generated by COMSOL Multiphysics simulations.

To further support our experimental observations, the fields and the field gradients were generated using commercial finite element software, COMSOL Multiphysics (COMSOL Inc.),[161] under identical conditions used in the experimental measurements. Figure 2.4 presents the spatial distributions of the fields and the strength of the gradient of the fields rE_2 over and across

the electrode. The large variations in the fields appeared at the sharp edge, which was in strong agreement with our experimental observations. An asymmetric shape of the gradient of the field is due to the non-uniform charge distribution near the electrode edge. Furthermore, the magnitude of field gradients decreases as z increases, confirming the separation distance-dependent, short-range DEP that is observed experimentally. Previous studies performed with both micro-scale particles and electrodes have revealed that F_{DEP} was sufficient to drive motions of the particles [165]–[167]. When the particle size decreases to the nanoscale, however, F_{DEP} substantially decreases due to the particle volume dependence of F_{DEP} ($F_{DEP} \propto R^3$). Thus, although F_{DEP} can be either repulsive or attractive by the driving frequency of the fields, our results proved that the strength and the apparent working distance of F_{DEP} were strongly dependent on both particles' dimension and electrodes' fine structure.

2.1. Conclusion

In conclusion, we achieved quantitative measurements of F_{DEP} and $\partial F_{DEP}/\partial z$ in conventional, nanoscale, electronic devices using the multi-pass AFM methods. The results provided the spatial distribution of DEP and its strong dependence on the nanoscale structure of the electrode and the nanoscale separation distance from the electrode edge. On this scale, precise measurements of DEP are more important for quantitative comparisons among the competing forces such as viscous drag, Brownian, and hydrodynamic forces to determine the dominant forces governing the movements of biomolecules. The development of techniques like in cell therapy, demands precise knowledge of DEP to design micro/nano electronic devices and tune the operating parameters associated with other interfering forces for the effective manipulation of the target particles.

CHAPTER 3. SELECTIVE MANIPULATION OF BIOMOLECULES WITH INSULATOR-BASED DIELECTROPHORETIC TWEEZERS[2]

3.1. Introduction

As mentioned in chapter 2, In principle, traditional DEP techniques utilize the geometry of metal electrodes to create nonuniform electric fields (Figure 3.1 (a)), which induces motion of polarizable objects from the medium to regions of strong electric fields by either attracting (positive DEP, pDEP) or repelling (negative DEP, nDEP) them [38],[153]. The electrokinetic-driven, selective trapping and separating of target objects from the medium to the electrodes have been demonstrated previously using DNA [168],[169], cancer cells [25],[155], and bacteria [170],[171], along with microfluidic configurations. Alternatively, insulator-based DEP (iDEP) or electrodeless DEP techniques have been developed to trap target objects with insulating obstacles rather than metal electrodes [64],[151],[172], eliminating potential fouling, electrolysis, and joule heating issues caused by the applied high electric field at the metal electrodes of the traditional DEP method. In these devices, a constriction or channel in an insulating material deforms the electric field in a solution, creating a high electric field gradient with a local maximum (Figure 3.1b). Thus, the insulating obstacles can trap target objects including DNA and cells [63],[172]. Moreover, iDEP provides a nonuniform electric field over the entire depth of the channel, increasing the effective trapping area without the issues [64],[172]. The advantage of iDEP is that it can be easily fabricated and integrated with microfluidic systems to improve

[2] The material presented in this chapter was co-authored by Oh, M.; Jayasooriya, V.; Woo, S. O.; Nawarathna, D.; Choi, Y. Jayasooriya V. conducted experiments with Oh. M., simulated the finite element models, manufactured micro needles and co-drafted and revised all versions of this chapter. Reprinted with permission, from Oh, M.; Jayasooriya, V.; Woo, S. O.; Nawarathna, D.; Choi, Y. Selective Manipulation of Biomolecules with Insulator-Based Dielectrophoretic Tweezers. *ACS Appl. Nano Mater.* **2020**. https://doi.org/10.1021/acsanm.9b02302.).

detection efficiency and enhance biomolecule mixing, separation, and concentration, which is not possible with other manipulation techniques, such as optical and magnetic trapping [169],[173].

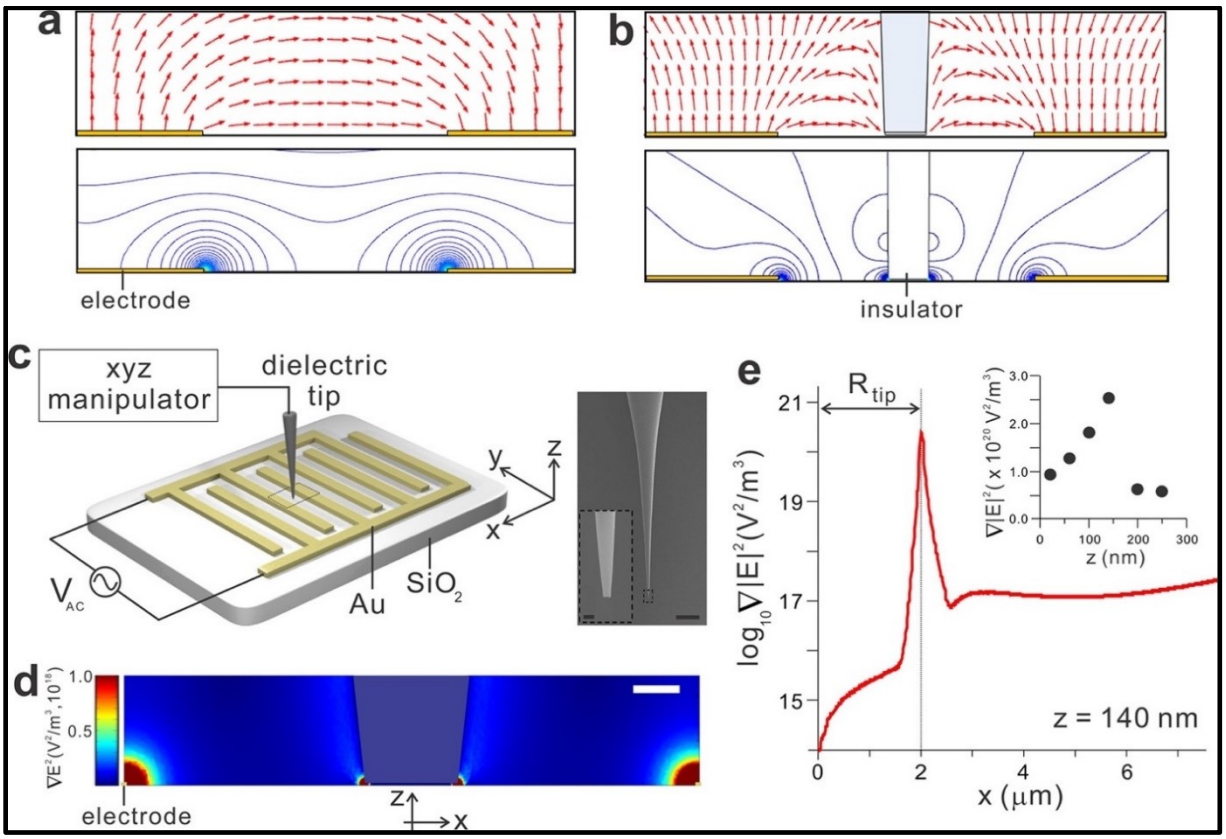

Figure 3.1. Insulator-based dielectrophoretic (iDEP) tweezers.
(a) Electric field lines (red arrow) and contour plot of the field created by the metal electrodes. (b) Deformation of the field by the insulating obstacle in the center generates the additional iDEP trap. (c) Schematic diagram of the device and zoomed-in SEM images of the insulating tip controlled by the xyz manipulator. The scale bars are 500 and 2 μm (inset). (d) The distribution and the strength of the electric field gradient around the tip calculated by the finite element COMSOL simulation, predicting the strong field gradient at the electrode edges and the tip end. The scale bar is 5 μm. (e) The line profile of the electric field gradient along the x-axis at the tip height z of 140 nm, showing a very sharp peak of the field gradient at the rim of the tip. The inset presents the peak values of the field gradient's strength as a function of z.

Although several DNA manipulation techniques have been improved and used to measure DNA unzipping,[174] hybridization,[175] and digestion of DNA by λ-exonuclease,[176] no effective methods have been developed for spatial control of DNA. For instance, fixed-position-based approaches, such as atomic force microscope (AFM), micropipette, and optical tweezers, and fixed-force-based approaches, such as a magnetic trap, allow limited control of DNA, since

DNA ends are fixed at the beads, AFM and micropipette cantilevers, and glass surfaces [177],[178]. Furthermore, those techniques suffer from the high force noise and drift associated with high bandwidth of the cantilevers and bead size [178],[179]. Thus, three-dimensional control of DNA using conventional manipulation techniques, including DEP and iDEP methods is not feasible. For the spatial manipulation capabilities, such as picking up, repositioning, and releasing, several nanoscale metallic tip- based DEP methods have been introduced. For example, conductive AFM probe tips [180]–[183] and nanoscale pipet tips coated with metal [168],[184],[185] have been used to create the nonuniform electric field and field gradient at the end of the tip, demonstrating as an alternative technique for manipulating biomolecules and biopolymers. However, the metallic tip based DEP methods in which a working principle is the same as the traditional DEP suffer from the drawbacks associated with electrochemical reactions at the metal DEP electrodes [151]. To overcome this limitation, we demonstrate insulator based, electrodeless, mobile DEP tweezers that provide spatial control and manipulation of biomolecules without the issues of fouling and electrolysis. In this work, we used nonmetal, unbiased tips that squeeze the electric field in the medium and create a strong, localized field and its gradients at the end of the tip. Thus, the tip acts like iDEP tweezers capable of three dimensional trapping, placing, and releasing biomolecules, such as DNA. Furthermore, this technique eliminates the complex fabrication of DEP devices, such as coaxial or triaxial nanoscale tips, and the requirements of specialized operating instruments like AFM.

3.2. Results

3.2.1. Modeling of the electric fields and the field disturbance

Our iDEP tweezers exploit the interdigitated electrode array, which has proven to be quite useful for dielectrophoretic separation in previous studies [159],[186],[187]. The device consists

of planar gold electrode arrays defined by the standard optical lithography technique on a SiO_2 substrate, similar to our previous work [186],[188] (Figure 3.1(c)) and an insulator tip controlled by an xyz manipulator between a pair of interdigitated electrodes. The strength of the electric field intensity gradient ∇E^2 in the proximity of the tip was examined using the COMSOL Multiphysics. Figure 3.1(d) and e depict the spatial distributions of ∇E^2 over and across the electrodes when an external AC voltage V_{ac} (7 V_{pp}, f = 50 kHz) is applied between two electrodes. Without the tip, the strong ∇E^2 were formed only at the sharp electrode edges because of the inhomogeneity of the electric field created by the external AC voltage, which agrees with our previous experimental observations [161],[186]. In the presence of the tip between the two electrodes, an additional strong ∇E^2 around the tip end was created (Figure 3.1(d)). The insulator tip deformed the electric field in the conducting solution and generated inhomogeneous field gradients with a local maximum surrounding it, suggesting strong DEP at the tip end ($F_{DEP} \propto \nabla E^2$).

The distribution of ∇E^2 along the x-axis demonstrates that ∇E^2 increases near the tip and maximizes at the tip edge (Figure 3.1(e)). Compared to the flat surface of the tip end, the edge line of the tip end is highly disordered, which produces additional nonuniform electric field distribution. The ∇E^2 peak sharply drops to the relatively flat ∇E^2 along the x-axis, demonstrating that the effective iDEP site is physically smaller than the tip. The effective trapping volume at the tip depends on the tip diameter because the distribution and centration of ∇E^2 around the tip varies with the tip dimension. Therefore, the unbiased insulator tip producing an additional localized iDEP trap is able to serve as a spatially mobile and remotely tunable biomolecule tweezers, in order to trap, relocate, and release the nanoscale objects.

3.2.2. Fluorescence imaging of the submicron particles with the iDEP tweezers.

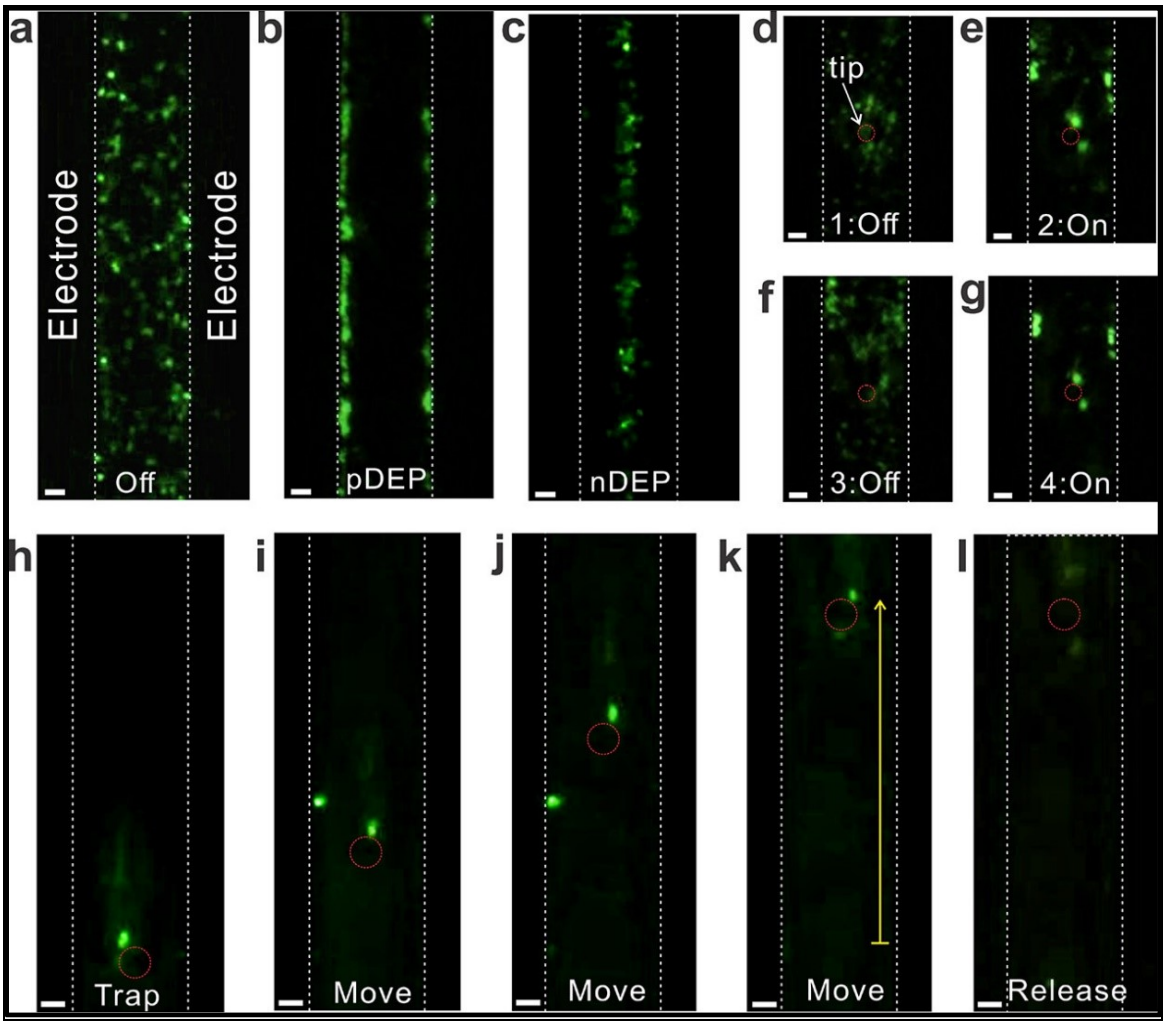

Figure 3.2. The IDEP manipulation of fluorescently labeled polystyrene nanoparticles. (a−c) DEP acting on the nanoparticles without the tip: (a) No AC field between the electrodes, (b) low-frequency AC voltage (5 V, 20 kHz) attracts the nanoparticles to the electrodes (pDEP), and (c) high frequency AC voltage (5 V, 2 MHz), in contrast, repels the nanoparticles to the center of the electrodes (nDEP). (d−g) In the presence of the tip, the nanoparticles were trapped around the tip when the AC voltage was applied (5 V, 20 kHz), and the trapped nanoparticles were instantly released from the tip after turning the AC voltage off. (h−l) The iDEP tweezers trap the nanoparticles, hold them while repositioning, and release them by turning off the AC voltage (5 V, 20 kHz). The yellow arrow is 80 μm. All scale bars are 5 μm.

To demonstrate the feasibility of the iDEP tweezers in relation to transport and mobility, we initially examined the polystyrene particles (Figure 3.2). First, the capability of traditional DEP acting on the particles was measured in the absence of the tip (Figure 3.2 a-c). In the absence of

both AC voltage and the tip, the particles were freely diffusive in the buffer (Figure 3.2 a). When the low frequency AC voltage (5 V_{pp}, f = 20 kHz) was applied, the particles were attracted to the electrode edge due to the positive DEP (pDEP, Figure 3.2 b). In contrast, the high frequency AC voltage (5 V_{pp}, f = 2 MHz) repelled the particles, so the particles were accumulated in the center between the two electrodes, where the electric field gradient is minimum. (nDEP, Figure 3.2 c). These frequency-dependent, bipolar DEP results were in excellent agreement with the classical Maxwell−Wagner (MW) theory,[38],[153] where the Clausis−Mossotti (CM) factor and the cross over frequency f_{co} of 0.7 MHz allow for the estimation of the frequency dependent F_{DEP} polarity.

Next, the particle trapping at the tip placed in the center of two electrodes was investigated. Figure 3.2 d−g demonstrate a series of measurements regarding the trapping of the particles at the tip by turning on and off the AC voltage between the electrodes. By turning on the pDEP trap bias, the particles were attracted to the high electric field near the tip and trapped at the tip end (Figure 3.2e). The trapped particles were immediately released and diffused away from the tip after turning off the pDEP trap bias (Figure 3.2 f). When the trap bias was reapplied, the particles were trapped again in similar fashion at the tip (Figure 3.2 g). Such trapping and releasing of particles were reproducible. After trapping particles, the tip was spatially manipulated. Figure 3.2 h−k are a sequence of images that show the motion of the tip and particles along the y-axis (yellow arrow). During the tip manipulation, the position and shape of the trapped particles were almost identical without further interferences from the electrodes. Following the repositioning of the tip and particles, the trap bias at the electrodes was turned off (Figure 3.2(l)). The particles were immediately released from the trap and freely diffused away from the tip. Thus, the iDEP at the tip is strong enough to trap and hold the particles while repositioning, in order to use the tip as nanoscale mobile tweezers. Please note that the particles drawn into the pDEP trap at the electrode

were not shown in Figure 3.2 h−k because some electrodes have smooth edges. Although the particles were still trapped on the electrodes, the particles on the Au electrodes could not be seen by the objective placed under the devices.

3.2.3. Spatial manipulation of DNA with the iDEP tweezers

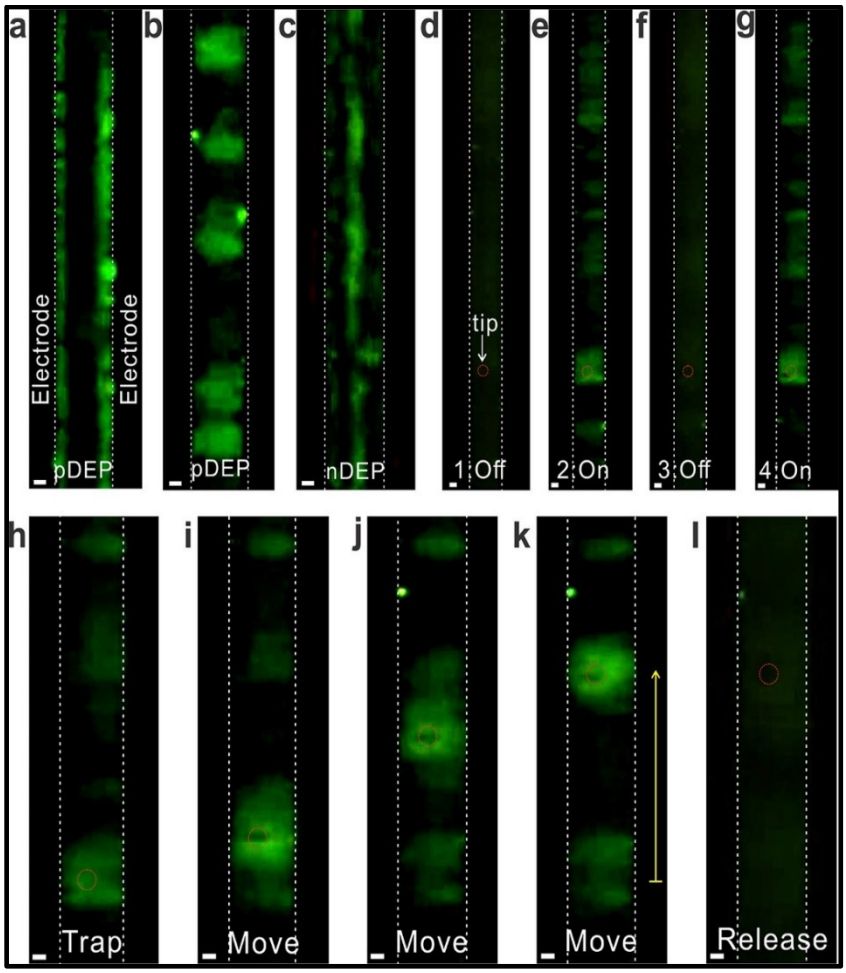

Figure 3.3. Spatial manipulation of DNA using the iDEP tweezers.
(a)-(c) DEP acting on DNA without the tip: (a) Low-frequency AC voltage (7 V, 50 kHz) strongly attracts DNA to the electrodes (strong pDEP). (b) By increasing the frequency of AC voltage (7 V, 200 kHz), DNA were trapped in the middle of two electrodes, forming the DNA clouds (weak pDEP). (c) High-frequency AC voltage (7 V, 10 MHz) repels DNA to the center of the electrodes (nDEP). (d−g) In the presence of the tip, the iDEP tweezers picked up DNA around the tip under the weak pDEP condition (7 V, 200 kHz), and trapped DNA were immediately released from the tip after turning the AC voltage off. (h−l) The iDEP tweezers trap DNA, hold them while repositioning, and release them by turning of the applied AC voltage (7 V, 200 kHz). The yellow arrow is 70 μm. All scale bars are 5μm.

Following the examination of the particles with the iDEP tweezers, we further investigated the capability of the iDEP tweezers in manipulating DNA (Figure 3.3). Compared to the particles, prediction of DEP strength and fco, determining polarity of DEP for DNA is very complicated [168],[189]. Several models including the CM factor [26],[182], quantitative measurement of the DNA polarizability α, [190]–[193] and the counterion fluctuation (CIF) [168],[189],[194] have been proposed to estimate DEP strength and polarity acting on DNA (see the Discussion section for further details). Although f_{co} is not exactly defined in those models, the polarity of DEP could be reversed at reasonably separated upper and lower frequency limit.

Similar to the particle manipulation, we first examined bipolar DEP acting on DNA (Figure 3.3 a−c). When a low frequency AC voltage was applied (7 V_{pp}, f = 50 kHz), DNA was attracted to the edge of electrodes (Figure 3.3(a)). After increasing the frequency of the applied AC voltage (7 V_{pp}, f = 200 kHz), DNA moved off from the electrode and trapped between two electrodes, forming stretched-DNA clouds (Figure 3.3 b). Such DNA cloud observation at the interelectrode gaps by the weak pDEP trap agrees with previous observation with the DNA plasmid [189],[191]. At a sufficiently high frequency (7 V_{pp}, f = 10 MHz), the DNA was repelled from the electrodes and aligned at the center of the two electrodes (Figure 3.3 c). Therefore, the low and high frequency AC voltages yield both pDEP and nDEP on DNA, suggesting bipolar CM factors. By placing the tip between a pair of interdigitated electrodes, the utility of the iDEP tweezers in trapping DNA was subsequently examined (Figure 3.3 d−g). When the bias of pDEP trap (7 V_{pp}, f = 200 kHz) was turned on, DNA was attracted to the tip, forming a broad, cloud-like structure surrounding the tip. Compared to the particles which are solid spheres, DNA is a long polymer chain, so the structure of DNA varies under different environments (e.g., pH, ionic strength, force acting on DNA). Thus, such broadening could be attributed to the stretched structure of DNA [193],[195].

When the pDEP trap vanished by turning off the applied AC bias, the DNA clouds completely disappeared around the tip, indicating that the iDEP tweezers can instantly trap and release DNA without any permanent attachment at the tip or damage due to the direct contact of the metal electrodes applied at a high AC voltage. Finally, the trapped DNA was manipulated by moving the tip along the y-axis (Figure 3.3 h−k). The DNA clouds initially formed around the tip and followed the direction of the moving tip. Throughout the manipulation, the volume and shape of the clouds were almost identical. These results suggest that our iDEP tweezers can tightly hold DNA, and that the trapping strength is consistent in the devices. Such capabilities are prerequisite for the precise measurements of protein properties and activities while controlling and manipulating proteins [179]. Following the repositioning the DNA clouds, the AC bias of the pDEP trap was turned off. DNA were completely released from the tip as shown in Figure 3.3 l. Such trapping and manipulating of DNA with iDEP tweezers were reproducible with both homogeneous DNA (48 502 base pairs) and nonhomogeneous mixed DNA containing 6 fragments from 3550 to 21 226 base pairs.

3.3. Discussion

Taken together, results from fluorescence imaging of the submicron particles and DNA demonstrate the effective control and manipulation of objects using the iDEP tweezers. In principle, our iDEP tweezers enable us to manipulate nanoscale particles (R > 11 nm) by comparing them to the competing thermal force ($F_{th} = \frac{K_B T}{2R}$).[26],[196] Here, we briefly discuss the physical mechanisms of the iDEP of DNA to guide design rules for creating effective iDEP tweezers for general use of other biomolecule control and manipulation measurements.

Depending on the dielectric responses of the objects and the surrounding medium, the external fields induce an instantaneous force $F_{DEP} = 1/4\alpha\nabla|E|^2$ acting on the objects with the

effective polarizability α of the object, which is associated with the frequency-dependent CM factor [38],[153]. For the spherical particles, spatially asymmetric force due to the inhomogeneous field gradient in the medium drives the movement of the polarized particles either by attracting or repelling them from the medium to regions of strong electric fields, such as the electrode edge or the tip end. Such frequency-dependent CM factors, polarizability, and DEP are in excellent agreement with many experimental observations and computational simulations, ours included [25],[186].

Unlike the dielectric particles, precise identification of α values for DNA and the influence of DEP on DNA are not completely understood, [197] since DNA is not a spherical particle but rather a long biopolymer where the negative charges of DNA are fixed at the backbone. Taking into account the DNA shape, the real part of α values of DNA could be estimated using either the traditional CM factor approach,[26],[182] the recent CIF model,[168],[189],[194] or experimental measurements[190]–[193]. By assuming the stretched DNA is an ellipsoid, the axis-dependent α of the CM factor model is given by $\alpha = 6v\varepsilon_m Re[K]$, where $K = \frac{\varepsilon_p^* - \varepsilon_m^*}{3[L_n(\varepsilon_p^* - \varepsilon_m^*) + \varepsilon_m^*]}$, L_n, ε_m^*, and ε_p^* are the complex CM factor, depolarizing factor, volume of the particle, and complex permittivity of the medium and particle, respectively.[198] The polarizability values found from the CM factor model were 6.53×10^{-28} Fm^2 at f = 50 kHz, 2.87×10^{-28} Fm^2 at f = 200 kHz, and -2.59×10^{-31} Fm^2 at f = 10 MHz, which yielded the DEP strength of 41.5 nN at f = 50 kHz, 18.3 nN at f = 200 kHz, and nDEP −16.5 pN at f = 10 MHz under constant AC voltage (7 Vpp).

Alternatively, the CIF model, in which the redistribution of counterions surrounding DNA under the AC fields is responsible for the movements of DNA, enables an estimate of the total polarizability given by $\alpha = \frac{z^2 q^2 L_s^2 n_{cc} A_{st}}{12 K_B T} \frac{l_{DNA}}{L_s}$, where z, q, L_s, n_{cc}, A_{st}, l_{DNA}, k_B, and T are the valence of counterion, the electric charge, the subunit length, the number of condensed counterions, the

stability factor of the ionic phase, the contour length of DNA, the Boltzmann constant, and the temperature, respectively [168],[189]. The total polarizability of the CIF model varies from 1.52 $\times 10^{-29}$ to 1.52 $\times 10^{-28}$ Fm^2 depending on the dielectric increment $\Delta\varepsilon$ values [194],[199]. For the 48 502 bp DNA, the polarizability per base pair yields values from 3.12 $\times 10^{-34}$ to 3.12 $\times 10^{-33}$ Fm^2/ bp, which agree with those determined by the experimental measurements and are within the range quoted in the literature [190],[200]. Thus, the CIF model predicts the DEP strength of 0.962−9.62 nN. Unfortunately, the CIF model does not allow the reasonable estimation of both pDEP and nDEP since the α values were remarkably insensitive to the frequency range, with only a 3-fold difference for a frequency that differs by 103-fold [191],[199]. Although previous DEP measurements with DNA have demonstrated the pDEP trap around the electrode or obstacles, no experiments have discussed nDEP, or the strength of nDEP that was simply assumed to be identical to pDEP with the reversed sign (i.e., nDEP = −|pDEP|) [201]. However, the observations of both pDEP and nDEP rely on the experimental limitations associated with either the DEP operating parameters (e.g., AC voltage, frequency, buffer, DNA fragment, and concentration) or the design of the DEP device. In addition to the polarity of DEP from those models, there is disagreement about the magnitude of DEP between them. First, the strength of pDEP, compared to the nDEP values obtained by the CM factor calculation, is substantially increased by almost 3 orders of magnitude. The overestimation of pDEP is originated by the ellipsoidal assumption of DNA in which the effective polarization is different along each axis. In particular, a prolate spheroid or highly elongated (needle shaped) object tends to align itself with its longest axis parallel to the external fields regardless of positive or negative DEP, [153] which resulted in highly asymmetric CM factor values at a low frequency regime (Figure 3.4). Such alignment behavior of the DNA could further lead to stretching them between two electrodes under the weak pDEP as shown in

Figure 3.3 b. Second, the pDEP values estimated from the two approaches differ by nearly a factor of 2−40. This difference is attributed to the assumption of DNA as a rigid rod in the CM factor model, which enhances its polarizability in a longitudinal direction and increases subunit length Ls in the CIF model. The CM factor calculation allows us to estimate f_{co} = 6.5 MHz and bipolar DEP (Figure 3.4), which confirms our experimental observations of pDEP and nDEP behaviors. Despite such valuable information from the CM factor model, the charge redistribution under the AC fields is inapplicable to DNA because the negative charges are fixed to the DNA backbone. While the CIF model considers the counterion fluctuation and its contribution to the polarizability of DNA under the AC fields, the polarity and frequency-dependence of nDEP cannot be derived from the model. Thus, further studies are needed to address the polarization mechanism for DNA under the influence of the nonuniform AC fields.

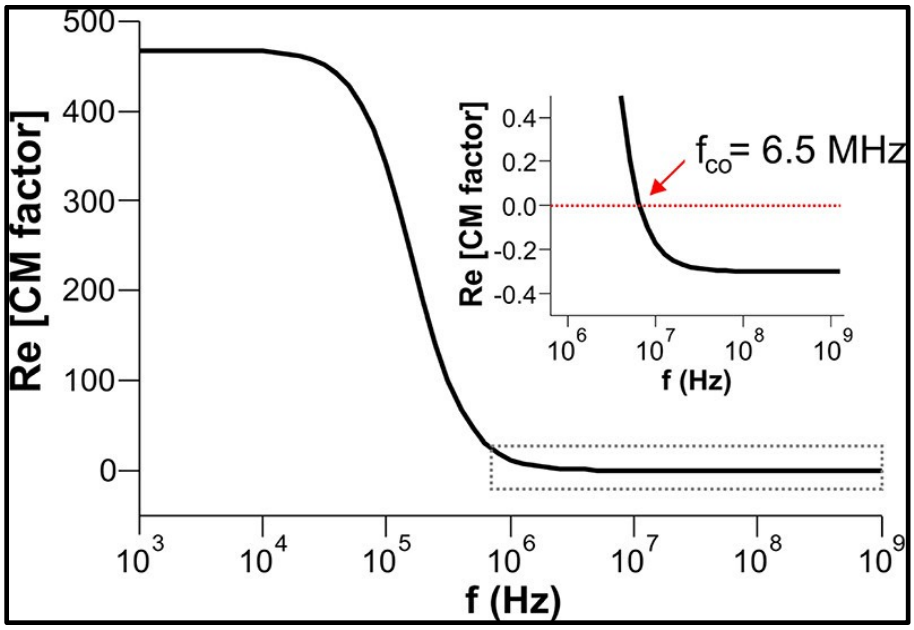

Figure 3.4. Asymmetric, frequency dependent real part of the CM factor assuming DNA as an ellipsoidal particle.
The inset shows the negative values of the CM factor at f > fco, which lead to negative DEP. In calculating this plot, the following parameters were used: a = b = 2 nm, c = 22 μm, εp = 8εo, εm = 78εo, σp = 1 S/m, σm = 5 × 10−4S/m.

In any case, the theoretical evaluation of the DEP must be stronger than the thermal force ($F_{th} = \frac{K_B T}{2R_H}$), driving the Brownian motion of particles with a hydrodynamic radius R_H at room temperature T because of its interference with the DEP manipulation [26]. Using the worm-like chain model,[202] the radius of gyration ($R_g \approx 1.54R_H$) of DNA was estimated to be 606 nm, which resulted in F_{th} of 5.23 fN. These results also suggest a minimum strength of ∇E^2 of 8.08×1016 V^2/m^3 at the trapping site to overcome the thermal diffusion.

Finally, the effective volume and trapping pattern of DNA are examined. The effective trapping distance from the tip end to the end of the trapped particles and DNA was measured to be approximately 3−8 μm, depending on the direction of the measurements. Considering the R_H of 393 nm and the contour length of 22 μm, the trapping distance and pattern suggest that the individual DNA is neither randomly coiled nor perfectly stretched. Instead, the DNA could be partially stretched under the AC fields, forming widely spread cloud structures around the tip end (Figure 3.3). Such cloud effects due to the partial stretching of DNA trapping was also observed when the pDEP conditions were changed (Figure 3.4). After increasing the frequency from 80 kHz to 200 kHz of the applied AC voltage (9 Vpp), DNA formed like clouds between two electrodes. In general, high frequency lowers the strength of DEP due to the decrease of the frequency-dependent CM factor in the CM factor model (Figure 3.4) and the total polarizability of the DNA in the CIF model [193],[200] and the experimental observations [191],[199]. Thus, the DNA cloud effects could be partially stretched DNA molecules due to the weak pDEP, which has been also previously observed [189],[191]. The experimental observation of the DNA trapping pattern manifests the strong dependence of DNA's α value on the frequency of the AC fields.

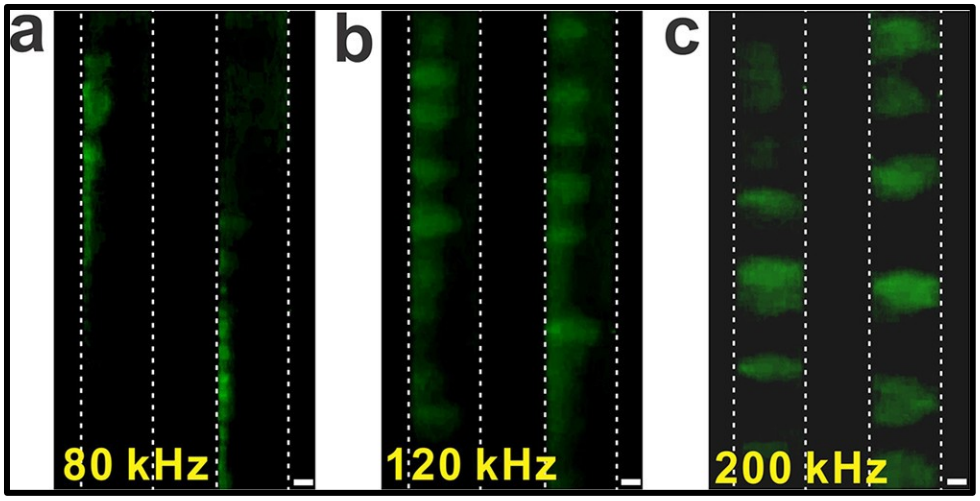

Figure 3.5. Frequency dependent DEP and the DNA trapping pattern.
(a) The low-frequency AC voltage generates strong pDEP, attracting DNA to the electrode (9 V, 80 kHz). (b) After increasing the frequency of the AC voltage (9 V, 120 kHz), DNA experiences slightly reduced pDEP, which causes the trapped DNA to partially move off from the electrode. (c) After further increasing the frequency of the AC voltage (9 V, 200 kHz), the DNA were fully stretched between the electrodes, indicating a significant dependence of the DEP strength and the DNA polarizability on the frequency of the applied AC voltage. The scale bar is 10 μm.

3.4. Conclusion

By linking an insulator tip and conventional dielectrophoretic method, we have demonstrated that our iDEP-based molecular tweezers can trap, carry, reposition, and release the submicron particles and DNA. The technique allows a simple and effective separation in a fluid environment without potential issues, such as fouling, electrolysis, and joule heating, associated with traditional metal-based DEP methods. We have compared two polarization models of DNA and demonstrated that either model could not fully describe iDEP behaviors of DNA. However, the strength of iDEP tweezers estimated by both models was strong enough to overcome the competing forces acting on a particle or DNA in a fluid, including thermal force and viscous drag. These results enable other researchers to design and determine operating parameters to successfully perform iDEP-based manipulation experiments with a range of biomolecules and biopolymers.

CHAPTER 4. DESIGN OF MICRO-INTERDIGITATED ELECTRODES AND DETAILED IMPEDANCE DATA ANALYSIS FOR LABEL-FREE BIOMARKER QUANTIFICATION[3]

4.1. Introduction

Biosensors are commonly used to quantify the levels of biomarkers, bacteria and DNA in biological samples[70]–[73]. In particular, quantification of biomarkers that are related to diseases is important because they indicate important biological states of diseases[203]. In medicine, biomarkers are utilized to detect infections and other diseases such as cancer, myocardial infarction and schizophrenia [74]–[76]. In addition, biomarkers are also used to evaluate prognosis and treatments [74]. In the context of cancer, the ability to measure specific cancer biomarker proteins in patients' serum or saliva with high accuracy will be leading to revolutionize the treatments [74]. To this end, Enzyme-linked immunosorbent assay (ELISA) is the gold standard for detecting/quantifying biomarker proteins [77]. The ELISA has a minimum detection limit of 250 pg. of target biomarkers in 1mL of sample [78]. This detection limit is not sufficient for many cancers, specially, in the early stage of tumor development, it is required to detect/quantify biomarkers much lower than the current limit [74]. To address this issue, number of other methods have been proposed and tested.

Among the techniques that are proposed for biomolecule detection in clinical and point-of-care settings, electrical impedance based biosensing (biomarker detection) is a low-cost, label-free and high-sensitive technique [85]–[87]. In electrical impedance based biomarker detection,

[3] The material presented in this chapter was co-authored by Jayasooriya, V. and Nawarathna, D. Jayasooriya conducted experiments and co-drafted and revised all versions of this chapter. Reprinted with permission, from Jayasooriya V. and Nawarathna, D., "Design of Micro-Interdigitated Electrodes and Detailed Impedance Data Analysis for Label-Free Biomarker Quantification". *Electroanalysis* **2017**, *29* (2), 330–338. https://doi.org/10.1002/elan.201600364.).

typically, the change of electrical impedance when biomarker protein is conjugated to the complementary antigen/antibody is measured [70]. Moreover, in biomarker protein detection, an antigen that has an affinity towards to target biomarker protein is, first, immobilized on the solid surface between electrodes, and impedance is measured. Second, serum or saliva sample is introduced, and target biomarker proteins conjugate with the antigens on the solid surface[70]. The impedance with and without biomarker protein is measured by applying a small sinusoidal voltage (<10mV) with a specific frequency or range of frequencies across electrodes and measuring current. The voltage to current ratio is used to calculate the complex impedance at a frequency. Finally, change of impedance, when target biomarker proteins present is calculated.

To quantify biomarker protein levels of a sample, the change of impedance is converted to the corresponding biomarker protein concentration (typically in g/mL or moles) using a standard curve [70]. The standard curve is generated using known concentrations of biomarker proteins and corresponding change of impedance. Since impedance of biomarker protein (change of impedance values) is frequency dependent, impedance experiments are carried out in range of frequencies. It has been demonstrated that target bio-molecules show very strong frequency dependent impedance variations in low frequency (<1MHz) [86]. Using the impedance data, the frequency or range of frequencies that has a linear relationship between molarity of biomarker protein and impedance (change of impedance) is determined. Various biomarker protein molecules, DNA and RNA have been successfully quantified using this technique [70],[204],[205]. However, electrical impedance at a given frequency is complex number ($Z=R+jX$; R is the resistance and X is the reactance) with magnitude ($|Z|$) and phase ($\phi = \tan^{-1}(X/R)$). In-depth analysis of impedance data using both $|Z|$ and ϕ will provide valuable information about the interactions between antigens, target biomarker proteins and electrolyte solution with externally applied AC voltage signals (AC electric fields).

This information on the physical phenomenon is needed to develop sensitive impedance based biosensing. Further, designing of sensitive IDE electrode arrays that can detect desired levels of biomarker levels are needed in the medical diagnosis. Unfortunately, there are no proper scientific investigations to address those questions.

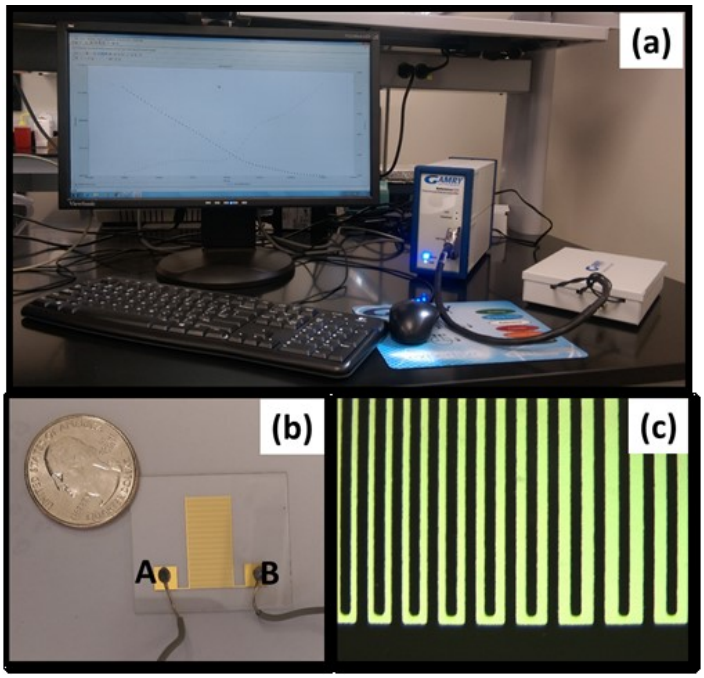

Figure 4.1. Components of the experimental set-up utilized in measuring impedance of biotin-avidin complexes.
(a) A picture of the experimental set-up showing the impedance analyzer, sample holder and software program to collect data. (b) A picture showing the micro-fabricated interdigitated electrode array with 166 electrode pairs (30µm gap between electrodes and 30µm width of each electrode). The impedance analyzer was connected to the A and B. (c) Close-up view of the interdigitated electrodes showing the gap between electrodes and density of electrodes.

To fill this critical need in impedance based biosensing, we have conducted a systematic study. In this study, we have designed, fabricated and utilized micro-interdigitated electrodes for our experiments. These electrodes are capable of generating high electric fields to excite target molecules and produce target molecule dependent impedance. Therefore, first, we investigated electric fields produced by the interdigitated electrodes and discussed the design of interdigitated electrodes for impedance measurement experiments. Second, we used biotin-avidin system as the

model and measured the electrical impedance (1Hz-1MHz) of 0-100pM avidin molecules. We then systematically analysed impedance data by decomposing measured impedance into real part (Re (Z)), imaginary part (Im (Z)) and phase (ϕ) of the measured impedance data. Finally, we have utilized theoretical Warburg electric circuit model to calculate sensitivity of the IDE array in quantifying avidin molecules.

4.2. Materials and methods

Figure 4.1(b) and (c) show pictures of the interdigitated electrode array (IDE) that we have designed and used in our experiments. In designing IDEs, first, to quantitatively understand the electric fields on individual IDEs, we have calculated the electric fields using COMSOL software (COMSOL, Inc.) in the frequencies from 1 Hz to 1 MHz. To set-up COMSOL calculations, briefly, IDEs were drawn to a scale using AutoCAD (Autodesk) software and imported into COMSOL software. We then used the AC/DC electric current (ec) module and frequency domain studies to calculate electric fields. Furthermore, we assumed that a buffer solution (σ=1.67 S/m and ε_r =80.3 at 0 Hz)) was filled over the IDEs and also assumed that an external sinusoidal potential (10 mV_{pp}) with a known frequency was applied on the electrodes. In addition, we assumed that the IDEs were connected to the external function generator (impedance analyzer) at A and B (Figure 4.1(b)). Finally, the IDEs were meshed using free triangular extremely fine mesh with maximum element size of 10 μm and minimum element size of 0.21 μm. Using this information, we calculated the magnitude of the electric field (|E|) in the frequencies 1, 100, 100000 and 1000000 Hz (Figure 4.2(a)) across the entire IDE array (from pair 1 to 166). These frequencies were selected to study the variation of electric fields in very low, medium and high frequencies and study how target biomolecules will interact with AC electric fields. Our COMSOL calculations indicate that there is a constant electric field established in each pair of IDEs below

10 Hz (Figure 4.2 (a)). Therefore, below 10 Hz, all the biomolecules including target biomarker protein and immobilized antigen complexes that are in the IDE array will experience constant electric field of 380 V/m.

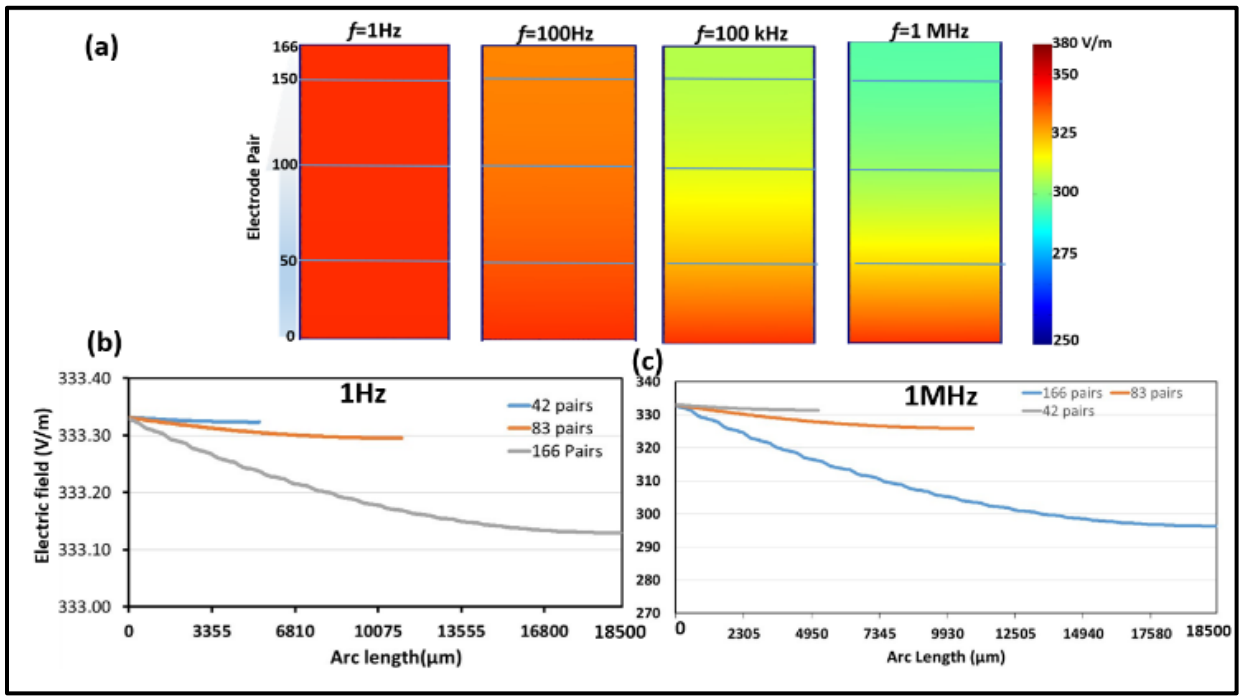

Figure 4.2. Design of electrodes of the IDE array using electric fields.
(a) Calculated variations of the AC electric fields from 0 electrode pair to 166 electrode pair. (b) and (c) Variation of the electric fields across the IDE arrays in 1 Hz and 1MHz respectively.

After 10 Hz, as the frequency increases from 10 Hz-1MHz, the magnitude of the electric field continue to decrease across IDE array (from pair 1 to 166). The pair 1 has the highest electric field because it is the closest to the points where the external potential was applied (A and B). For example, at 1MHz, pair 1 has about 340 V/m electric field and pair 50 has electric field value of 320 V/m. Similarly, 100 and 160 the IDE pairs have electric field values of 300 and 290 V/m respectively. The magnitude of the electric field generated over a pair of IDEs is important because the electric field must be large enough to electrically polarize all the biomarker proteins and produce impedance across IDE electrode pairs [154],[206]. These electric field values are capable of successfully polarizing the biomolecules. If target biomarker protein molecules that are between

any IDE pair do not contribute to the measured impedance (because molecules are not being able to electrically polarize), change of impedance may not correlate well with the molarity of biomarker protein molecules that are in the sample. This will lead to inaccurate results when quantifying number of biomarker protein molecules in the sample. Therefore, it is required to perform electric field calculations and find the variations electric fields across the IDEs array. In addition, using electric field calculations, for a given biomarker quantification, it can be determined the minimum number of IDE pairs needed in the array.

In addition, number of IDE pairs in the array is also important. To systematically determine the number of IDE pairs, we studied how electric fields vary with number of interdigitated electrode pairs of an IDE array (Figure 4.2 (b)). As shown in the Figure 4.2(b), when IDE arrays get smaller (by reducing number of electrode pairs), the variation of electric fields across each pair diminish. On the other hand, when the IDE array gets smaller (by reducing the number of IDE electrodes), the total surface area between electrodes are reduced. This will reduce the number of binding sites available for target biomolecules. One can increase the spacing between electrodes to increase the space available for antigen molecules, but it will cause to decrease the magnitude of the electric field. To avoid the electric fields weakening, one can easily increase the external potential applied the IDE array. Furthermore, the width of the electrode also very important. Wider electrodes occupy the substantial space in the IDE array. On the other hand, when the width of the electrodes is getting narrow, the production cost of the electrodes is significantly increase because it requires special photo lithography masks and lithography equipment. The gap of the electrode is also important in the impedance experiments. The gap will determine the magnitude of the electric field applied to the biomolecules. Again, to produce electrode with small gaps between electrodes will cost more to fabricate. In addition, if the gaps are very small, small signal

assumption utilize in the impedance measurements will not be valid and generate inaccurate impedance readings. Since the electrical impedance is a quantitative measurement of the molecules. Any changes to width and gap of the electrodes will affect the measured magnitude of the impedance because those changes will alter the number of molecules that can have between electrodes. At the same time, when width and gap change, total sensing area will change (increase or decrease). Therefore, the total effect on the impedance will depend on the extent of each activity. Further one can adjust the width and the gap of the electrodes without changing the measured impedance. The phase values will not change because phase values are dependent on the ratios of the real and imaginary impedance values. Figure 4.2(b) shows the variation of electric field across IDE arrays that have 166, 83 and 42 IDE pairs.

We have employed the IDE array (discussed above) indicated in the Figure 4.1(b) for impedance experiments. The IDEs were fabricated in gold (1000Å) on glass wafers using standard microfabrication techniques (Figure 4.1(b)) [207],[208]. The detailed description of the fabrication steps are discussed elsewhere [207],[208]. Prior to experiments, IDEs were visually and microscopically observed to see any defective electrodes like electrically short-circuiting electrodes pairs because these electrodes are not capable of generating electric fields to polarize target biomolecules. In addition, we have also measured the DC resistance of the IDE array to make sure that there are no short-circuiting IDEs. Before the experiments, IDE array was cleaned using standard solvents (Acetone and Isopropanol) to remove any organic contaminants.

4.3. Results

We used biotin-avidin system for this study and demonstrated the details of our in-depth impedance analysis. The biotin molecules were attached on to the glass surface between IDE electrodes. To attach biotin molecules, APTES (3- Triethoxysilylpropylamine, 5% APTES w/v)

chemistry was performed on the sample and modified the glass surface with amine (NH2) molecules [20]. We then systematically conjugated biotin molecules with known molarities (1fM-100 pM) by incubating biotin molecules with avidin molecules at room temperature for 30 minutes [204],[209]. After conjugation, the free avidin molecules were removed and entire IDE array was filled with a buffer. We have utilized two standard buffer solutions (2X SSPE and HEPES) for experiments. 2X SSPE buffer contains 2 mM EDTA and 0.3 M NaCl in 20 mM phosphate buffer (pH 7.4) and Triton-X was added to this 2X SSPE buffer, to a final concentration of 0.1 vol.% Triton-X in the 2X buffer. For each avidin molarity, impedance was measured (magnitude and the phase from 1Hz-1MHz by applying a sinusoidal voltage of 10mV p-p between A-B) (Figure 4.1) for each buffer solution.

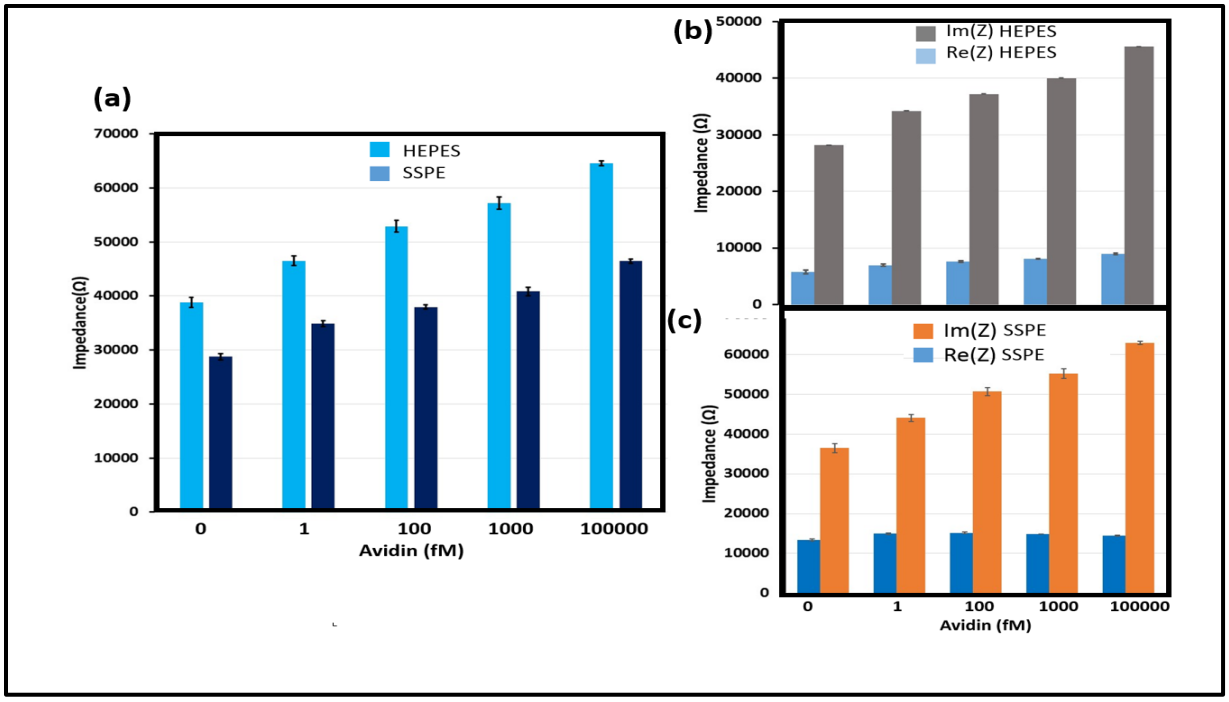

Figure 4.3. Measured impedance values of the biotin-avidin complexes using the set-up in Figure 1(a).
a) Variation of the |Z| vs. molarity of the avidin molecules in the HEPES (Conductivity 0.763 S/m) and 2X SSPE (Conductivity 3.815 S/m) buffers. (b) and (c) Variations of the Re(Z) and Im(Z) vs. the molarity of the avidin molecules in the HEPES and SSPE buffer respectively. The impedance was recorded at 1Hz.

Table 4.1. Variation of the impedance with molarities of the avidin. [a] and [b] Indicate the variation of |Z|, Re(Z) and Im(Z) with the molarities of the Avidin. The impedance was recorded for the frequencies from 1 Hz to 1 MHz.

(a)	Frequency (Hz)		1	100	1000	100000	1000000
Impedance (Ω)	HEPES Buffer	|Z|	38837	803.1	102.9	14.5	11.78
		Re(Z)	13365	145.4	34.52	13.88	11.74
		Im(Z)	36465	-789.8	-96.94	-4.18	1.02
	1 fM avidin	|Z|	46525	838.1	103.6	14.3	11.75
		Re(Z)	14990	122	33.23	13.71	11.71
		Im(Z)	-44045	-829.2	-98.15	-4.1	1.02
	100 fM Avidin	|Z|	52914	869.8	106	14.36	11.78
		Re(Z)	15180	112.8	33.24	13.75	11.72
		Im(Z)	-50690	-862.5	-100.7	-4.14	1.14
	1 pM Avidin	|Z|	57207	889.6	107.6	14.28	11.73
		Re(Z)	14815	108.8	33.17	13.66	11.68
		Im(Z)	-55255	-883	-102.4	-4.15	1.063
	100 pM Avidin	|Z|	64562	922.4	111.1	14.73	12.01
		Re(Z)	14425	101.8	34.16	14.085	11.96
		Im(Z)	-62930	-916.8	-105.7	-4.3	1.057
(b)	Frequency (Hz)		1	100	1000	100000	1000000
Impedance (Ω)	SSPE Buffer	|Z|	28772	548.9	80.5	12.67	10.27
		Re(Z)	5762	137.8	33.16	12.14	10.22
		Im(Z)	28190	531.4	73.36	3.63	1.06
	1 fM avidin	|Z|	34893	628.4	85.56	12.71	10.3
		Re(Z)	6924	132.3	31.59	12.17	10.25
		Im(Z)	-34200	-614.3	-79.52	-3.67	1.11
	100 fM Avidin	|Z|	37979	672.2	88.64	12.95	10.28
		Re(Z)	7605	131.4	31.04	12.37	10.24
		Im(Z)	-37210	-659.3	-83.03	-3.852	0.91
	1 pM Avidin	|Z|	40833	694.7	89.67	12.82	10.26
		Re(Z)	8061	122.5	30.16	12.25	10.2
		Im(Z)	-40030	-683.8	-84.45	-3.81	1.147
	100 pM Avidin	|Z|	46457	745.1	92.5	12.91	10.24
		Re(Z)	8935	113.5	29.25	12.31	10.19
		Im(Z)	-45590	736.5	87.76	-3.88	1.09

Commercially available impedance analyser (Gamry instruments, reference 600+) was used to measure the impedance. Each experiment was repeated 2-3 times to calculate the statistical variations. Figure 4.3(a) illustrate the variation of the magnitude of the impedance (|Z|) with molarities of avidin molecules at 1 Hz. It has been demonstrated that magnitude of the impedance is dependent on the molarity of avidin molecules at low frequency (1Hz- 1 kHz). This is the most common way of representing impedance data (molarity vs |Z|) by others (Figure 4.3(a)) [204]. It is also obvious that there is a linear relationship between magnitude of the impedance and the molarity of avidin molecules. Therefore, it can be used to quantify unknown amounts of avidin molecules in samples. In addition, magnitude of the impedance is dependent on the medium conductivity (SSPE or HEPES). Using similar experiments, it has been detected/quantified proteins such as hIgG(50 ng/mL), HSA (1.6 ng/mL) and αfetoprotein (50 ng/mL) by others [210],[211]. Next, we have utilized the phase and the |Z| to further analyse the impedance data. Specifically, variation of phase with frequency provide useful information on understanding how biotin and/or avidin complexes contribute to the measured impedance. To explore the phase information in quantifying the avidin molecules in the sample, we have decomposed the magnitude of the impedance into real and imaginary parts. When Z(ω) represent the measured complex impedance of the sample including biotin, avidin, buffer and electrodes at frequency f (ω=2Πf), resistance R can be represented as

$$R(\omega) = Re\big(Z(\omega)\big) = |Z(\omega)|cos\emptyset \quad (4.1),$$

and reactance (X) at frequency f is mathematically represented as

$$X(\omega) = Im\big(Z(\omega)\big) = |Z(\omega)|sin\emptyset \quad (4.2),$$

Where ∅ is the phase angle of the impedance at f and

$$tan(\emptyset) = \frac{X}{R} \quad (4.3)\ [212].$$

We have utilized the equations 4.1-4.2 and calculated the variations of X and R vs. the molarity of avidin molecules in SSPE and HEPES buffers. Figure 4.3(b) and 3(c) indicate the variations of the X and R with molarity of avidin molecules at 1 Hz. Table 01 indicate the variations of |Z|, X and R with molarity of avidin molecules at low- high frequencies (1Hz-1MHz) in SSPE and HEPES buffers. From this analysis, it can be concluded that at low frequency (<100 Hz), the major contribution to the magnitude of the impedance is from the reactance (X: R=4:1). As the frequency increases, reactance decreases and resistance increases. Specifically, at very higher frequency (~ 1MHz), the major contribution to the measured impedance is contributing by the resistance (X: R= 1:10). Therefore, at low frequency, only reactance, X, correlate with the molarity of the biotin. Furthermore, reactance (X) is sensitive to the molarity of the avidin molecules that are conjugated with biotin molecules. To further explore the impedance data with phase, we have analysed variation of phase with frequency. Figure 4.4(a) and (b) show the variation of the phase (with frequency) of the avidin molecules (1fM-100pM) in SSPE and HEPES buffers.

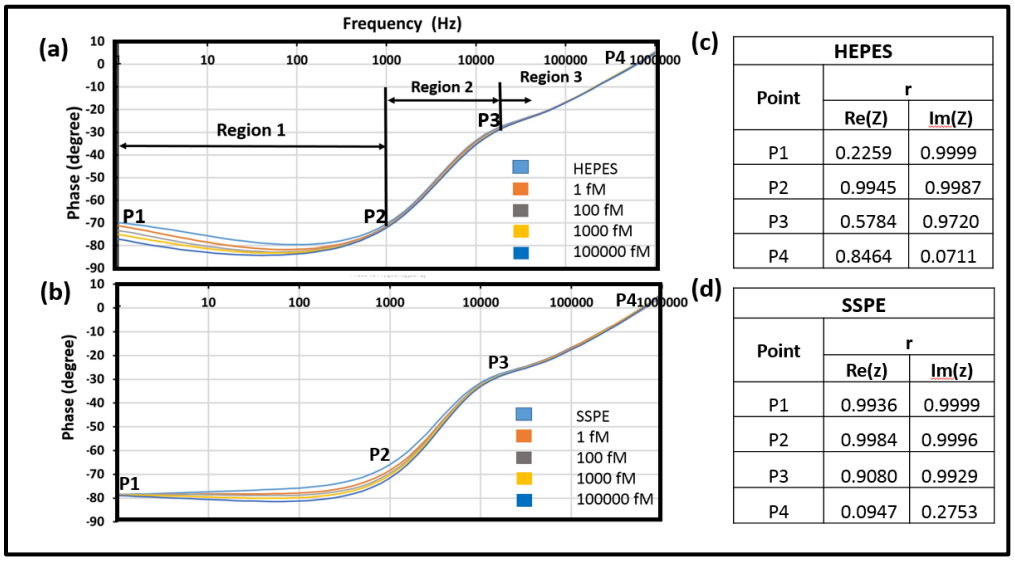

(c)

HEPES		
Point	r	
	Re(Z)	Im(Z)
P1	0.2259	0.9999
P2	0.9945	0.9987
P3	0.5784	0.9720
P4	0.8464	0.0711

(d)

SSPE		
Point	r	
	Re(z)	Im(z)
P1	0.9936	0.9999
P2	0.9984	0.9996
P3	0.9080	0.9929
P4	0.0947	0.2753

Figure 4.4. Avidin molarity dependent phase variation.
(a) and (b) Experimentally measured phase variations with molarity of avidin molecules in the HEPES and SSPE buffers respectively. The phase values were measured from 1Hz to 1 MHz. (c) and (d) Calculated r values for Re(Z) and Im(Z) of the impedance. The r values were calculated for the avidin molecules that were HEPES and SSPE buffer.

By observing the variations of the phase, 3 distinct regions can be recognized in the phase vs. frequency plot for each buffer. For the HEPES buffer (Figure 4.4(a)), from 1-1000 Hz, the phase values almost constant with slight variation (region 1). Therefore, the region 1 can be treated as the constant phase region. From 1000-10000Hz, the phase values vary drastically from -80° to -30° (region 2) and for the frequencies 10kHz-1MHz, phase values vary from -20° to +5° (region 3). Similarly, for the SSPE buffer (Figure 4.4(b)), from 1-400Hz, phase values are approximately 80° (region 1). This is the constant phase region for the SSPE buffer. From 400Hz- 8000Hz, phase values vary from -80°-30° (region 2). The phase varies from -30°- +5° from 8000-1000000Hz (region 3).

Among these three regions, the measured impedance in the region 1(constant phase region) is mostly reactance (X, $\sin\phi\approx1$) with very small contribution from resistance (R, $\cos\phi\approx0$). To understand how these impedance values, correlate with the molarities of avidin molecules, we have calculated the Pearson's correlation coefficient (r) for selected points in the region 1 (P1 and P2 are indicated in the Figure 4.4 (a) and (b)). There is a perfect linear relationship ($r\approx0.99$) between impedance (R or X) and the molarity of avidin molecules (Figure 4.4 (c) and (d)). However, for the P1 (resistance part of the impedance) in the HEPES buffer indicate r value of 0.23. This is due to highly fluctuating small resistance. Further, in this region, reactance (X) is making a dominant contribution to the measured impedance.

In the region 2, the magnitudes of impedance are in the range of 10-100Ω. In comparison with region 1, the magnitude of impedance values in the region 2 are about 1000X smaller. In this region, for both SSPE and HEPES buffers, phase values are changing drastically with the frequency (~-80° to -30°). We have then selected a point (P3) in region 2 and calculated the r values (Figure 4.4(c) and (d)). At P3, dominant contribution to the magnitude of the impedance is

from resistance (R). However, we noticed that r values are ~ 0.95. We have also noticed that r value (of the resistance) of the avidin molecules that are HEPES buffer is ~.60. Overall, in region 2, magnitude of the impedance is small and have highly fluctuating r values. Therefore, region 2 may not be good choice to use for quantification of avidin molecules.

In the region 3, there is a crossover point for phase (changing from – ve to +ve). The crossover frequency for both SSPE and HEPES buffer are around 500 kHz (Figure 4.4(a) and (b)). From 500kHz- 1000 kHz, the phase values are positive (0-5°). Since the reactance (X) is positive above the cross-over point, the inductance of the circuit contributes to the measured impedance readings. Since, there is no inductors in our biotin-avidin assay or in the IDE array, we believe that the cables that we used to connect the IDE array to the impedance analyser will contribute the impedance in this region. Therefore, we believe that in region 3, contribution from the avidin molecules to the measured impedance may be very minimal. This is evident from our correlation coefficient calculations (Figure 4.4 (c) and (d)).

Since avidin molecules show a molarity dependent impedance variation in the constant phase region (region 1), as our next task, we were interested in developing a circuit model for the IDEs with biotin-avidin complexes in the constant phase region (region 1). In addition, using the circuit model, we were interested in explaining the impedance data. For region 1, the IDEs, buffer, biotin and avidin molecules can be represented as a resistive-capacitive ladder network [213].

Systematic development of resistive-capacitive ladder model for our IDE array is illustrated in Figure 4.5 (a-c). As shown in the Figure 4.5(c), resistors r_i represent the ohmic resistance of individual fingers of IDEs and ci represent the capacitance between adjacent electrodes of the IDEs. The capacitance values are mainly due to the buffer, biotin and avidin

molecules. The complex equivalent impedance of a frequency f (1Hz ≤ f ≤ 1000Hz) of the resistive-capacitive ladder network is given by the Warburg impedance (Z(ω)) [213].

$$Z(\omega) = A(j\omega)^{-n} \tag{4.4}$$

Where 0≤n≤1, A is a constant and phase of the Z (ω) is ∅, $(\emptyset) = -n\frac{\pi}{2}$. Note that for a given value of n, ∅ is a constant in the frequency range from 1Hz to 1000Hz. Schrama calculated the analytical expressions for resistance (r_i) and capacitance (c_i) of the individual IDEs of the ladder network [26]. Those values are indicated below.

$$r_k = 2h^n P(n) \frac{\Gamma(k+n)}{\Gamma(k+1-n)} - h^n \delta_{k0} \tag{4.5}$$

$$c_k = h^{1-n}(2k+1) \frac{\Gamma(k+1-n)}{P(n)\Gamma(k+1+n)} \tag{4.6}$$

$$P(n) = \frac{\Gamma(1-n)}{\Gamma(n)}. \tag{4.7}$$

Where h is a small number, k is an integer running from 0 to ∞, 0<n<1 and δ is the Kronecker delta. We have used Schrama's expressions and calculated the variations of r_i and c_i values across our IDE array (from pair 1 to pair 166) for each avidin molarity (0-100 pM) and buffer (SSPE and HEPES) separately.

For SSPE and HEPES buffer, the measured phase is constant in the region 1. For HEPES buffer, there is a molarity dependent variation of phase at 1Hz. Similarly, for SSPE buffer, molarity dependent variation is at 250 Hz (Figure 4.4 (a) and (b)). Therefore, for HEPES and SSPE buffers, we have used the phase values at 1Hz and 250 Hz respectively. For each molarity of avidin in each buffer (SSPE and HEPES), we first calculated the n using phase$(\emptyset) = -n\frac{\pi}{2}$. We have used the experimentally measured ∅ value to calculate the n. The values of k vary from 0 to 166 for our IDE array. The value for h for each molarity of avidin was calculated using following expression,

$$h = \frac{-1}{\tan(\emptyset) * \omega * \frac{\Gamma(n)}{\Gamma(n+1)}} \tag{4.8}$$

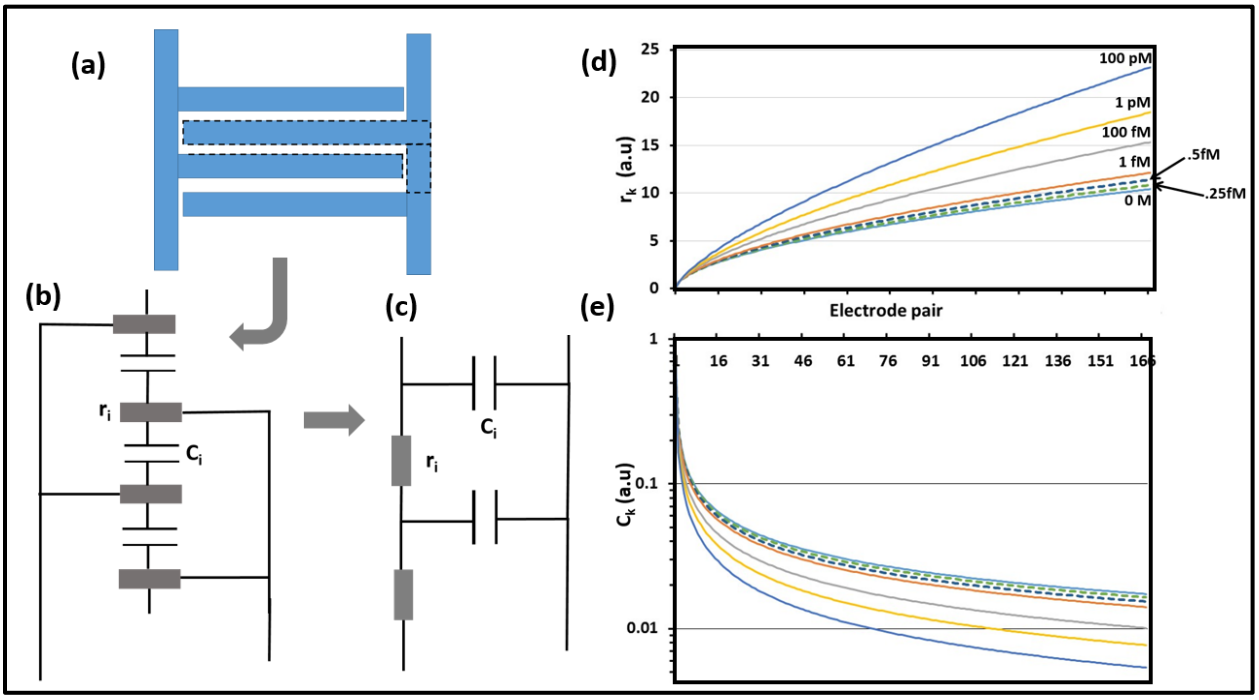

Figure 4.5. Development of resistor capacitor ladder network to determine the sensitivity of the IDE array.
a), (b), and (c) Systematic development of the resistor capacitor ladder network for the IDE array with biotin-avidin molecules. (d) and (e) Variations of the resistor and capacitor values of individual IDE pairs with molarity of the avidin molecules that were in the HEPES buffer. Broken lines indicate the calculated variations of the resistors and capacitors of individual electrode pairs using the experimental values.

The Eq. 4.8 was derived by calculating the phase of the impedance using (a) Schrama's equations and (b) simply solving the ladder network for r_o and k_o and equating values from two methods. After calculating n and h for each avidin molarity, we have calculated the variations of ri and ci of each IDE pair in HEPES buffer (Figure 4.5 (d and e)). It can be concluded that the last electrode pair of the IDE array (166th electrode pair) provide the most significant molarity dependent resistance and capacitance, in contrast, first few electrode pairs (1-9th pair) of the IDE array do not indicate avidin molarity dependent variation in capacitance and resistance.

Using the calculated values for capacitance (c_i) and resistance (r_i) vs. IDE electrode pairs (Figure 4.5 (d and e), we have calculated the smallest avidin molarity that can be quantified using our IDE array. To calculate the smallest avidin molarity, briefly, we plotted the n vs. molarity of the avidin. There is a linear relationship with n vs. molarity of the avidin. Using the linear relationship, we calculated the expected n values for .5 and .25 fM of avidin. Using the n value, we have calculated the phase (∅). The value of h was calculated using eq (4.8). Finally, variation of the c_i and r_i values of each IDE pair was calculated and plotted (indicated in the dotted line in the Figure 4.5(d and e)). According to our calculations .25 fM is the lowest avidin molarity that can be quantified using out 166 electrode pair IDE array. We extended our calculations for the SSPE buffer, our calculations show a minimum of 0.25fM avidin can be quantified in SSPE buffer (data not shown). From this calculation, it can be concluded that the sensitivity of an IDE array is independent of the conductivity of the buffer solution.

Next, we studied how measured impedance vary with number of IDE pairs of the array. This is important because, we have just proved that last IDE pairs of the array show significant molarity dependent ci and ri values. Therefore, we were interested in understanding how impedance vary with number of IDE pairs. Since our IDE array is a complex circuit, obtaining an analytical expression for the impedance with resistors and capacitors would be challenging. Therefore, we have simplified our IDE array. Specifically, we have disregarded the resistors in our circuit and assumed that all the capacitors (c_0, c_1, c_2,….c_k) are connected to each other in parallel. When 0<i<k, it can be easily proved that the

$$|z_{i-1}| - |z_i| = \left[\frac{1}{\sum_{l=0}^{i-1}\omega C_l} - \frac{1}{\sum_{m=0}^{i}\omega C_m}\right] > 0 \qquad (4.9)$$

Therefore, the when increasing the number of IDEs, the measured impedance will decrease. Increasing number of electrode pairs of the IDE array can improve the detection/quantification

sensitivity but decrease the impedance of the IDE array. If the impedance is small, the factors such as cable impedance will be providing a significant contribution to the impedance. Therefore, the measured impedance may not correlate with the avidin molarities.

4.4. Discussion

In conclusion, from this initial study, we have demonstrated that the electric fields between individual IDE pairs is an important design consideration when designing sensitive IDE arrays. Depending on the frequency of the externally applied electric potential, IDE electrodes that are away from the point where electric signal is applied (away from A and B in Figure 4.1(b)) may generate weak electric fields. Therefore, in designing, it is needed to perform these electric field calculations and verify every IDE pair of the array will have enough electric field to polarize biological particles, which will be a design consideration for micro-electroporation systems. Also, we have utilized theoretical Warburg circuit model to build an experimental impedance model and predict the sensitivity of an IDE array. These calculations are also very important in designing IDE arrays for various applications like detecting the extracellular concentration monitoring during electroporation. Depending on the application, for a given number of IDE electrode pairs, one can figure out the smallest molarity of the target biomolecules that can be detected/quantified using an IDE array with certain number of electrode pairs.

CHAPTER 5. A DISPOSABLE, LOW-POWER, AND SENSITIVE UNIVERSAL BIOSENSOR FOR CLINICAL APPLICATIONS[4]

5.1. Introduction

Among the diagnostics methods, except for the protein biomarker detection discussed in chapter 4, profiling the expression levels of nucleic acid (e.g., DNA, RNA, and microRNA) biomarkers is used widely in circulating biomarker testing is performed for most diseases, including cancer, cardiovascular disease, and infections [214]–[216]. Currently, biomarker testing involves multiple assays and instruments to detect various molecular types. For example, expression profiling of nucleic acid biomarkers, such as DNA, mRNA, and microRNA (miRNA), is commonly performed using quantitative reverse transcription-polymerase chase reaction (RT-qPCR), which involves the production of identical copies or sections of nucleic acid molecules of interest and subsequent labeling of the copied molecules with fluorescent dye molecules; fluorescent intensity is then used to quantify molarities of the nucleic acid molecules of interest [217],[218]. Although RT-qPCR is widely utilized in both clinical diagnosis and fundamental biomarker discovery studies, there is a need to develop methods to deliver rapid and affordable healthcare. This is because the cost of an RT-qPCR machine is $25,000 or more, the assay time is ~7 h or more, assay optimization (e.g., temperature and time required for each PCR reaction step) is needed before molecular quantification, expression profiling of short molecules (e.g., miRNA) requires costly target-specific probes (e.g., TaqMan probes) for high sensitivity and selectivity, and additional steps (e.g., multiplexing) can be required to detect more than one target in a single

[4] The material presented in this chapter is currently under review after submission to Biomicrofluidics journal and was co-authored by Logeeshan Velmanickam, Vidura Jayasooriya, and Dharmakeerthi Nawarathna. Jayasooriya V. conducted experiments, analyzed results and co-drafted the paper. Reprinted with permission, from Logeeshan Velmanickam, Vidura Jayasooriya, and Dharmakeerthi Nawarathna. “A disposable, low-power, and sensitive universal biosensor for clinical applications”

assay [219],[220]. Next-generation sequencing (NGS), microarray-, electrochemical-, plasmonic-, and hybridization-based nucleic-acid sensors have also been developed for nucleic acid biomarker detection, but these techniques require expensive equipment and large quantities of starting material and involve long and labor-intensive assays; therefore, they are ideal for resource- and personnel-limited clinical settings [220]–[222].

Enzyme-linked immunosorbent assay (ELISA) is used for antigen expression profiling in clinical samples [223],[224]. ELISA uses absorbance, fluorescence, or electrochemical signals produced by the target-probe conjugation, which is typically antigen-antibody conjugation. ELISA requires a costly (>$10,000) scanner for end-point chromogenic or fluorogenic analysis, and the assay time is ~4 h or more and involve an expensive (e.g., the average kit price is approximately $600), multi-step process that is prone to contamination or false-positive detection, as well as having a narrow dynamic range [161],[223],[224]. Despite the wide use of ELISA in clinical applications, there is a need to reduce the instrument and operation cost, increase the throughput and speed, improve the accuracy and performance, and simplify the assay. To address these issues in biomarker detection, in this study, we tested a potential device and assay that is applicable to analyze multiple clinical biomarkers, such as nucleic acid and antigens, in resource and technology limited settings, such as clinics, hospitals, and rural medical centers. To demonstrate the concept, in this study, we have used the technology to quantify microRNA (miRNA) and antigen molecules in diluted serum samples. Both miRNA and antigen molecules are currently being used as biomarkers or under investigation for sensitive biomarkers for many diseases.

5.2. Experimental section

There were three steps to follow in the biomarker detection and quantification; step (1) was performed in a commercially available micro-centrifuge tube, and the other steps were

performed on the disposable device that we have developed for this study. Briefly, in step (1), target molecules were labeled with their complementary molecules. Step 2 involves separating target molecules from non-target molecules and concentrating them in the micro-interdigitated electrodes within the device. Finally, in step (3), the quantification of target molecules is performed.

In step (1), it was required to conjugate/hybridize target molecules with their complementary molecules. For example, to analyze the expression of miRNA molecules that are typically about 22 nt long, complementary DNA molecules (22 nt) of the target miRNA were added to the sample (e.g., serum or cell lysate) and hybridized with target miRNAs and produce miRNA-DNA duplex molecules; the hybridization of miRNA and DNA is typically efficient at 50℃ for about 10 min [57]. Similarly, to detect and quantify the expression of antigen (protein) molecules, complementary monoclonal antibody molecules of the targets were added to the sample and, by incubating at room temperature for about 20-30 min, these conjugate to produce antigen-antibody complexes [225].

After step (1), the sample was added to the device by (region indicated within the yellow rectangle in Figure 5.1(a)) carefully pipetting about 10 μL of the sample (from step 1). 10 μL was selected to fill our electrode area but electrode area needs to increase to accommodate higher sample volumes. In step (2), separation of target molecules from non-target molecules was performed, followed by the concentration of the target biomarkers in specific area of the device. Speedy separation of target molecules from other molecules with high accuracy is generally difficult to achieve. For this, multiple methods and devices have been investigated. However, these methods require complicated multistep assays that take hours to days to complete, as well as skilled technical personnel, and therefore they are not suited to clinical settings [226],[227]. In this study,

we have developed an approach that uses multiple molecular-field (electric and temperature) interactions to efficiently separate target molecules from other molecules in the sample and selectively concentrate labeled target molecules (e.g., miRNA-DNA duplex molecules) near electrodes in the device. To achieve accurate quantification, non-target molecules (e.g., free DNA and non-target miRNA molecules) were strategically concentrated away from the target molecules. In step (3), quantification of target molecules was performed. There are multiple methods available for molecular quantification. Fluorescence-based methods are very popular and widely use in detection[228]. Detection of molecules with fluorescence requires fluorophore labeling of target molecules, and fluorescence intensity is used to quantify the molarities of the biomarker molecules. Since the concentration of target biomarker molecules is typically minute (< 1 pM) in clinical samples, the fluorescence intensity is generally weak, and therefore it is difficult to differentiate fluorescence intensity of target biomolecules from the background. To address this issue, in this work, we have investigated the use of electrical impedance. The electrical impedance experiments apply a small AC electrical signal (10 mV, 0–1 MHz) and measure the complex electrical impedance over the range of frequencies [188].

The device has planar gold microelectrodes that were manufactured on a commercially available glass substrate, using traditional photolithography based micro-fabrication techniques. The current version of the device has electrodes covering a 5 mm × 5 mm area, and the electrodes are about 100 nm in height (Figure 5.1(a)). Each device has about 2500 pairs of T-shaped interdigitated electrodes (TIEs). Traditional finger-like interdigitated electrodes have been used in number of biomedical assays, including cell separation, cell detection, and molecular analysis [229]–[233]. However, in this study, we have designed T-electrodes (consisting of semi-circular, and straight rectangular electrodes (Figure 5.1(b))) to efficiently separate and concentrate target

biomarker molecules. The external AC potentials applied (10 V_{pp}, 0–1 MHz) on the TIEs produce temperature and electric fields and their gradients near the TIE electrodes. These temperature and electric field gradients result in thermophoresis (or thermophoretic diffusion) and dielectrophoresis (or dielectrophoretic force), respectively, on suspended molecules. The extent (magnitude and direction) of those effects could depend on the molecular structure (e.g., conjugated vs. not conjugated and single-stranded vs. double-stranded) of the affected molecules. For example, a frequency-dependent differential dielectrophoretic force of single vs. double-stranded DNA molecules has been demonstrated [151]. To use the dielectrophoretic force to efficiently separate target from non-target molecules and quantify target molecules in the sample, the dielectrophoretic force must be able to effectively separate and concentrate molecules in the entire sample. To investigate this, we have used the AC/DC module of COMSOL software and calculated the expected capture volume for double-stranded (miRNA-DNA duplex molecules) and single-stranded molecules (free DNA and miRNA). The capture volume is the volume near TIEs where electric field effectively captures the molecules by dielectrophoresis. Mathematically, capture volume is the region near the electrodes that satisfies

$$\frac{\frac{1}{2}\alpha E^2}{kT} > 1, \tag{5.1}$$

where E is the electric field, α is the frequency-dependent electric polarizability of the molecule, k is the Boltzmann constant, and T is the temperature [57]. Figure 5.1(c) and (d) show the calculated capture volumes or spatial variation of $\frac{\frac{1}{2}\alpha E^2}{kT}$ in the frequency of 1 MHz for double-stranded (miRNA-DNA) and single-stranded (DNA and miRNA) molecules, respectively. miRNA-DNA molecules have a capture volume that has an approximate diameter of 5 μm or more, and single-stranded miRNA/DNA molecules have a small volume (diameter < 100 nm). According to this calculation, miRNA-DNA molecules that are located within about 5 μm could experience

the effects of the applied electric fields or the dielectrophoresis, and similarly, single-stranded molecules that are located within <100 nm or less could experience the dielectrophoretic effects. In comparison, the capture volume calculation indicates that dielectrophoresis could effectively be used to concentrate a large number of double-stranded molecules that are located within the 5 μm capture volume.

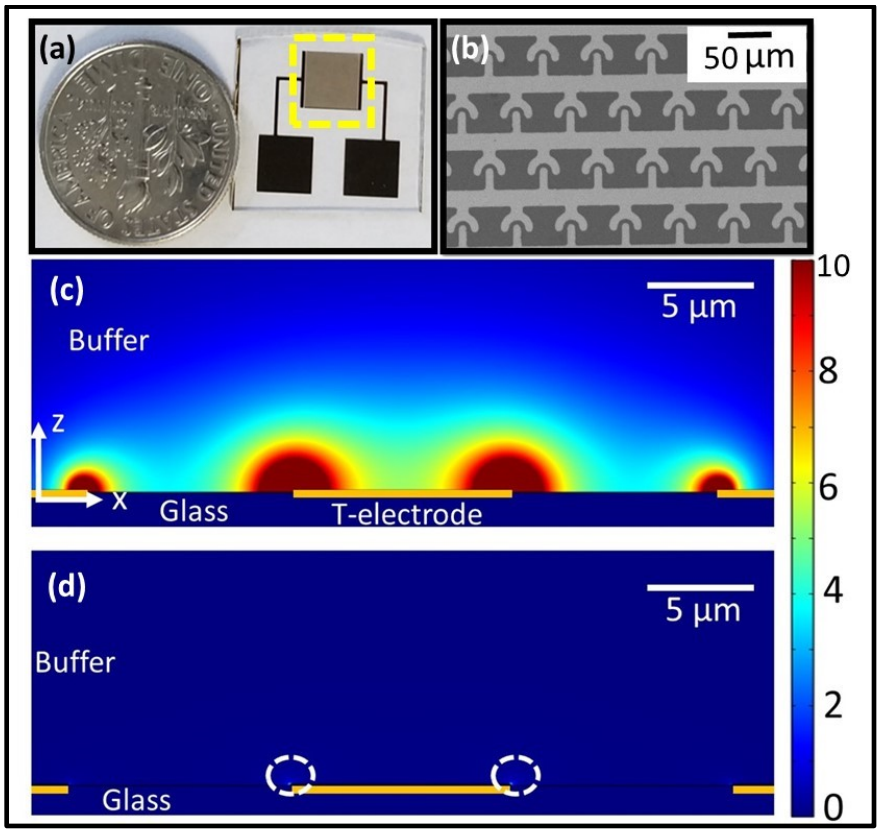

Figure 5.1. Universal biomarker sensing device, and calculated dielectrophoretic capture volumes of target molecules and non-target microRNA molecules.
(a) A picture of the biosensor used in the experiments. The area enclosed in the yellow broken rectangle has an array of T-shape interdigitated microelectrodes (TIEs). The sample was pipetted on the TIEs for detection and quantification. (b) Scanning electron microscope image of T-electrodes showing the shape of individual electrodes and the density of TIEs. (c, d) Dielectrophoretic capture volumes around the TIEs for target miRNA-DNA (c) and non-target molecules (d). In order to be captured by dielectrophoresis, the molecules must be in an area that has a calculated $\frac{\frac{1}{2}\alpha E^2}{kT}$ number greater than 1.

When dielectrophoretic force concentrates the molecules (both target and non-target molecules) near the electrodes, the local molecular concentration near the TIEs significantly increases, which leads to concentration-dependent diffusion of molecules to drive molecules out of the highest concentrations. However, the diffusion could only drive the single-stranded molecules or non-target molecules because double-stranded duplex molecules are firmly held by strong dielectrophoretic force. Moreover, when we calculated the magnitudes of the dielectrophoretic forces of double-stranded miRNA-DNA duplex molecules and single-stranded molecules, we found that the smallest dielectrophoretic force of the duplex molecules is about 1000-times larger than the maximum value of the dielectrophoretic force of single-stranded molecules. Since the dielectrophoretic force is dependent on the electric field gradient ($\nabla|E^2|$), it concentrates the target molecules in the area that has the largest $\nabla|E^2|$ [57]. We have calculated the $\nabla|E^2|$ in the x, y, z = 0 plane of TIEs (Figure 5.2(c)) and found that the largest $\nabla|E^2|$ occurs between the T-electrodes, and therefore, target molecules are concentrated between individual T-electrodes. Capture volume and $\nabla|E^2|$ calculations were performed by applying an electric potential of 10 Vpp (1 MHz frequency) and assuming that the molecules were suspended in the 0.01 × TE buffer (Tris EDTA; 5 μS/cm). The electric polarizability values (α) for miRNA-DNA duplex and free DNA and miRNA in the high frequency (1–50 MHz) were 10^{-32} and 3.4×10^{-35} $CV^{-1}m^{-2}$, respectively [234]. Another important conclusion drawn from the capture volume calculations is that only a small amount of the target molecules that are located within the capture volume could be separated and concentrated between TIEs. When the device is used to quantify molecules in the entire sample, it might provide inaccurate results about the total quantity of target molecules or even produce significant variations between runs. Therefore, ideally, there must be a method to concentrate molecules (both target and non-target) in their capture volumes.

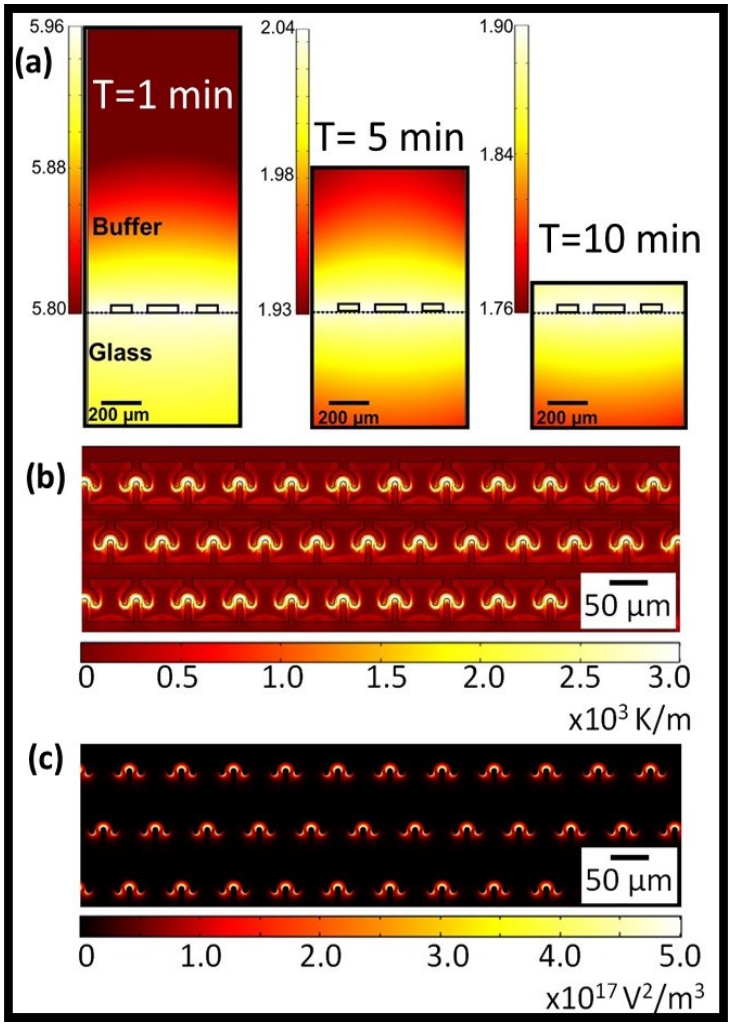

Figure 5.2. Conceptual demonstration of target molecular capture and concentration between TIEs.
(a) Calculated time and distance-dependent temperature distribution (in Kelvin) around TIEs. Note that the sample volume gradually decreases with time (60,300,600 seconds), but locations of high and low-temperature gradients do not change. (b) Calculated $\nabla(T)$ variation on the TIE electrode plane (x, y, z = 0). (c) Calculated $\nabla(E2)$ variation on the TIE electrode plane (x, y, z = 0). Since the maximum values of $\nabla(T)$ and $\nabla(E2)$ were produced between TIEs, target molecules were captured and concentrated by integrated dielectrophoresis and thermophoresis. Non-target molecules were driven out of the region of target molecules by concentration-based diffusion.

We have investigated the use of thermophoretic mobility of molecules as a method for mobilizing molecules toward their capture volumes. The thermophoretic mobility is a result of thermophoresis, which drives molecules along the temperature gradient $\nabla(T)$, either to the largest or smallest $\nabla(T)$. The effect of thermophoresis could extend far beyond the localized

dielectrophoretic effects. For example, electric field distribution around a point charge is inversely proportional to the square of the distance ($\frac{1}{r^2}$), and therefore $\nabla(|E^2|) \propto \frac{1}{r^3}$. Using a similar argument, the variation of $\nabla(T)$ around a point heat source (e.g., heated electrode) is inversely proportional to the distance between the heat source and the point (r) [158],[235]. Therefore, the strength of thermophoresis could extend a far greater distance than $\nabla|E^2|$ dependent dielectrophoresis. A temperature distribution or $\nabla(T)$ can be established in the sample using Joule heating or applying a voltage on electrodes. We will present detailed calculations of $\nabla(T)$ and $\nabla|E^2|$ near TIEs later in the discussion. To further understand how thermophoresis could be used to concentrate molecules in a specific area within TIEs, we have studied how electric potential, frequency, and conductivity of the buffer produce temperature distributions in the vicinity of the TIEs. We have found that an electric potential of 10 Vpp, 1–20 MHz applied on TIEs produces a maximum temperature increase of about 7–8°C in the TE buffer (conductivity = 5 μS/cm) in the device. This temperature increase does not cause any structural damage to the molecules, such as the melting of miRNA-DNA duplex molecules or antigen-antibody conjugates. Therefore, we have used these experimental conditions to produce temperature in our experiments.

As the buffer temperature goes up, some of the sample buffers evaporate, and the sample volume could be decreased. We have used the Joule heating module of the COMSOL software and studied the time-dependent temperature increase near the TIEs (Figure 5.2 (a)). The calculation shows that it takes about 10 min to increase the temperature to the maximum value of about 8°C (Figure 5.2(a)), which is consistent with our experimental observations. In addition, this calculation identifies the areas in the x-z plane with the largest (between TIEs) and smallest (on TIEs) $\nabla(T)$s. Next, we calculated the distribution of $\nabla(T)$ in the x, y, and z = 0 plane of the TIEs (Figure 5.2(b)). Braun's group has recently demonstrated that thermophoresis drives short nucleic

acid molecules, such as miRNA-DNA and DNA, along $\nabla(T)$ and concentrates both miRNA-DNA and DNA molecules in the location with the highest $\nabla(T)$ [236]. By simple comparison, maximum values of both $\nabla(T)$ and $\nabla|E^2|$ take place between TIEs, and therefore thermophoresis could be integrated with dielectrophoresis to efficiently concentrate target and non-target molecules in their dielectrophoretic capture volumes. The smallest $\nabla(T)$ occur on TIEs, as a result single-stranded (miRNA and DNA) molecules concentrate on TIEs by diffusion. Once the target molecules are separated and concentrated between electrodes, it is necessary to quantify and calculate the molarity of the target molecules, which is done in step (3) of the assay.

5.3. Results and discussion

First, we developed experiments to demonstrate how integrated thermophoresis, dielectrophoresis, and diffusion effectively and efficiently separate target molecules from non-target molecules and concentrate between TIEs. We have used fluorophore (fluorescein: excitation, 494 nm; emission, 512 nm) labeled nucleic acid (miRNA-DNA and DNA) and protein (antigen-antibody and antibody) molecules in experiments. The molecules were labeled with fluorophore tags for easy visualization. Dipole moments of nucleic acid and protein molecules are significantly larger (more than 100-times) than that of fluorophore molecules. Therefore, the labeling of biomolecules with fluorophore molecules does not have any effect on the dielectrophoretic force of the biomolecules. We have varied the frequency of the electric potential (0–10 MHz) to determine the best experimental conditions for nucleic acid and protein molecules. Separate experiments were performed for target and non-target molecules. Briefly, in experiments, we have pipetted 1 μM of molecules (e.g., miRNA-DNA or complementary DNA) suspended in 0.01 × TE buffer and pipetted about 10 μL on TIEs, turned on the electric potential (10 V_{pp}; 0–10 MHz), waited about 10 min to achieve the maximum fluorescence intensity, and measured the

intensity between TIEs at each frequency. Similarly, antigen and antibody molecules were suspended in manufacturer recommended 0.01x PBS (phosphate buffered saline) solution and rest of the experimental procedure was similar to previous nucleic acid experiment.

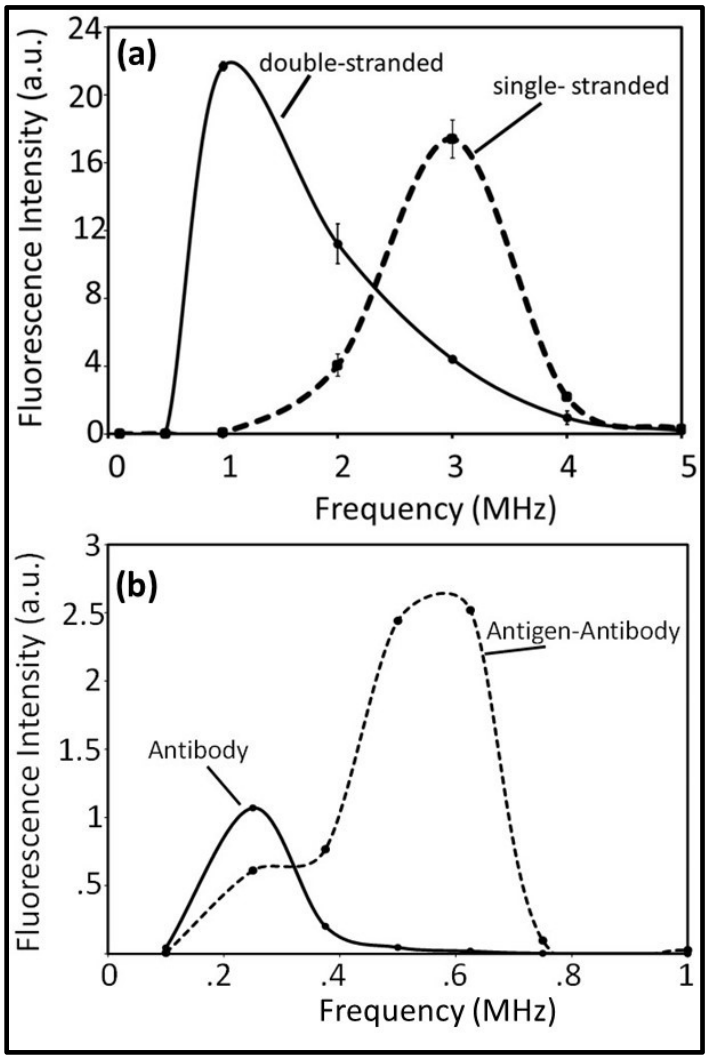

Figure 5.3. Experimental demonstration of separation and concentration of target biomarkers between TIEs.
(a, b) Variation of fluorescent intensity (between TIEs) with the frequency of the applied electric potential for fluorophore-labeled let 7b-miRNA-DNA and single-stranded DNA that is complementary to let 7b miRNA. Note that at 1 MHz, only let 7b-miRNA-DNA is captured and concentrated between TIEs. Similarly, (b) illustrates the fluorescence intensity for fluorophore-labeled conjugated IL-6 antigen-antibody and fluorophore-labeled IL-6 antibody molecules. Note that at 0.6 MHz, only conjugated IL-6 antigen-antibody molecules are captured and concentrated between TIEs.

Figure 5.3(a) and (b) show fluorescence intensities for let-7b-miRNA-DNA, complementary DNA to let-7b, conjugated interleukin-6 (IL-6)-antigen-antibody complexes, and monoclonal antibody for IL-6, respectively. Let-7b miRNA and fluorophore labeled DNA was synthesized by Midland Certified Reagent Company at Midland, TX, and purified anti-human IL-6 antibody was purchased from BioLegend, San Diego, CA, and IL6- antigen was purchased from MyBioSource (San Diego, CA). We also have measured the fluorescence intensity on TIEs, but we saw an accumulation of fluorescence on the electrode. However, we did not observe concentration of fluorophore intensity on the TIEs (data not shown). We believe that non-target molecules (e.g., complementary DNA and antibody for IL-6) are spread out on TIEs. At 1 MHz, miRNA-DNA duplex molecules could be separated and concentrated between TIEs with ~100% purity, and conjugated antigen-antibody complexes could be separated and concentrated with ~100% purity at 0.6 MHz. This result also demonstrates that both double-stranded miRNA-DNA and antigen-antibody complexes could be separated and concentrated between TIEs in a single assay. Moreover, it is necessary to concentrate and quantify antigen-antibody complexes at 0.6 MHz, and then, at 1 MHz, miRNA-DNA molecules could be concentrated and quantified. However, we have not investigated the simultaneous concentration of miRNA-DNA and antigen-antibody molecules.

As our next step, we studied the potential use of electrical impedance to quantify the molarities of target biomarkers that are concentrated between TIEs. When the electrical impedance of the TIE array is measured after molecular separation and concentration, it could still measure the cumulative impedance from the target and non-target molecules, metal electrodes, and buffer solution. We have systematically developed experiments to understand how target and non-target molecules contribute to the electrical impedance. Moreover, concentration of target molecules

(e.g., hybridized miRNA-DNA) between TIEs could alter the capacitance between individual TIE electrodes. Similarly, the concentration of non-target molecules (e.g., free complementary DNA and non-target miRNA) on TIEs could also alter the weak capacitance between electrodes that is produced by the leakage electric fields through the air.

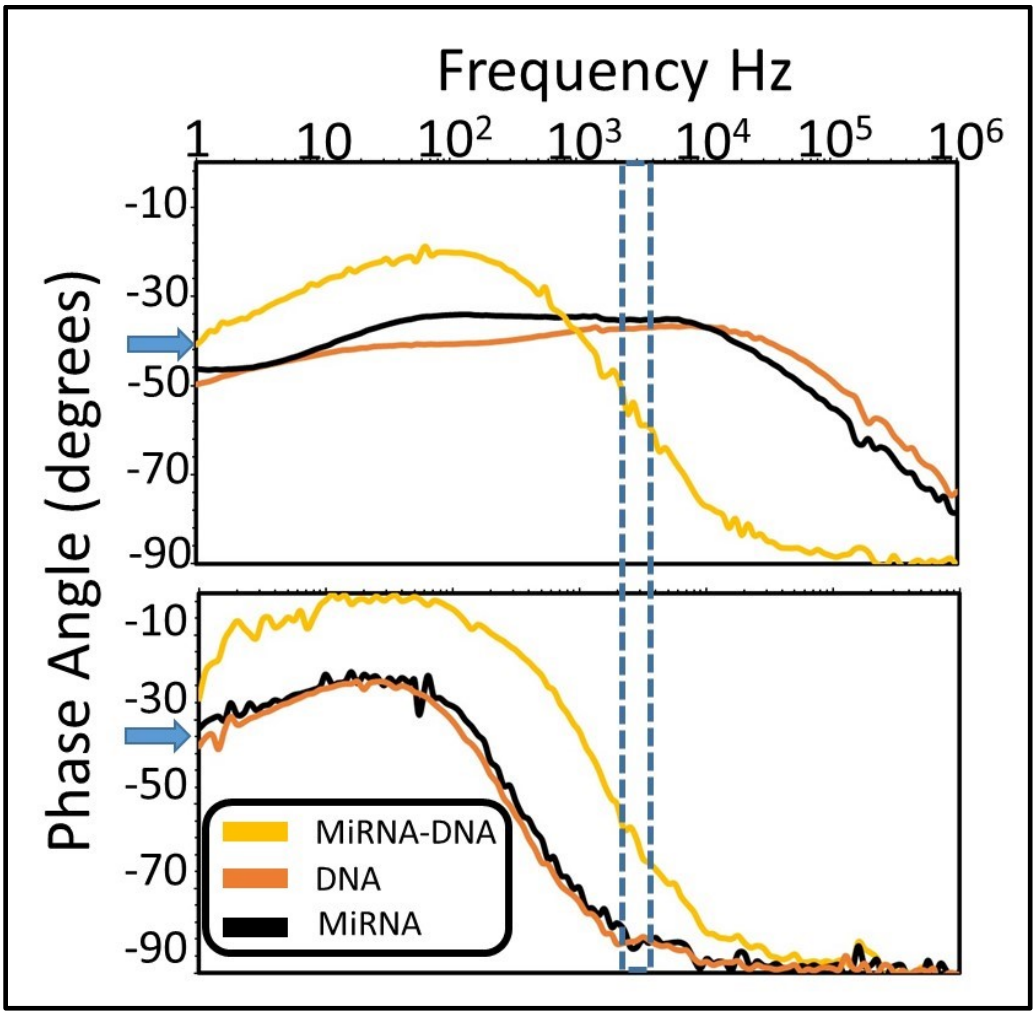

Figure 5.4. Electrical phase spectroscopy of miRNA-DNA, miRNA, and DNA molecules. Phase spectroscopy of miRNA-DNA, miRNA, and DNA molecules at 1 MHz (a) and 3 MHz (b). Note that when molecules (both target miRNA and non-target miRNA and DNA) are concentrated between TIEs, this produced a unique phase spectroscopy pattern. Moreover, phase spectroscopy of molecules that were concentrated between TIEs has a low-frequency region (1 Hz to 5 kHz) that was dominated by resistive impedance and, the measured impedance was reactive in the in the high-frequency region (5 kHz to 1 MHz).

First, we were interested to understand how molecular concentration would produce electrical impedance. We have separately measured the impedance spectra of (impedance vs. frequency) 1 nM let-7b-miRNA, complementary DNA to let-7b, and hybridized let-7b-miRNA-DNA molecules (suspended in the 0.01 × TE buffer). Briefly, we have pipetted about 10 μL of sample on to the device, applied 10 Vpp at 1 MHz electric potential to produce thermophoresis and dielectrophoresis on molecules, and recorded the impedance and phase spectroscopy of the sample by applying an electric potential of 10 mV, 0–1 MHz. We then plotted the phase spectroscopy or variation of phase angle of the impedance with frequency for each molecule (Figure 5.4(a)). Both DNA and miRNA have similar variations of phase spectra, and miRNA-DNA molecules had a markedly different phase spectroscopy (yellow curve with blue arrow at 1 Hz). These unique phase variations of single (e.g., miRNA and DNA) and double (e.g., miRNA-DNA) stranded molecules could be due to their structure (single vs. double-stranded) and/or location within the TIEs (between vs. on TIEs). To further understand the origin of the unique phase variation, next we performed another experiment in which we have used 10 Vpp at 3 MHz to concentrate molecules. Note that single-stranded miRNA and DNA molecules experience larger dielectrophoretic forces at 3 MHz than double-stranded miRNA-DNA molecules and concentrate between TIEs (Figure 5.3 (a)). At 3 MHz, miRNA-DNA duplex molecules also experience a dielectrophoretic force and could also concentrate between TIEs. By simple comparison of phase spectra at 3 MHz, miRNA, DNA, and miRNA-DNA produced identical variation of the phase with frequency (Figure 5.4 (b)). Moreover, note that miRNA and DNA produced a variation pattern similar to the miRNA-DNA molecules at 1 MHz (Figure 5.4 (a)). From these experiments, it can be concluded that the variation pattern of phase with frequency is more dependent on the locations of molecules within the device (between or on TIEs) than the molecules themselves. According to

phase vs. frequency data for miRNA-DNA duplex molecules concentrated between TIEs (Figure 5.4), the phase spectroscopy can be sub-divided into low and high frequency regions. The low-frequency region lies between 1 and 5 kHz (Figure 5.4), in which the majority of the impedance is resistive ($-50° \leq \theta \leq -20°$), and the high-frequency region lies between 5 and 1000 kHz (Figure 5.4). In the high-frequency region, impedance is reactive ($-90° \leq \theta \leq -50°$). Similarly, for conjugated IL-6 antigen-antibody molecules suspended in 0.01x PBS, in the low frequency (1 Hz-10 kHz) region, the impedance was resistive ($-40° \leq \theta \leq -10°$) and high frequency region was from 10 kHz – 1 MHz in which impedance was reactive ($-90° \leq \theta \leq -40°$);

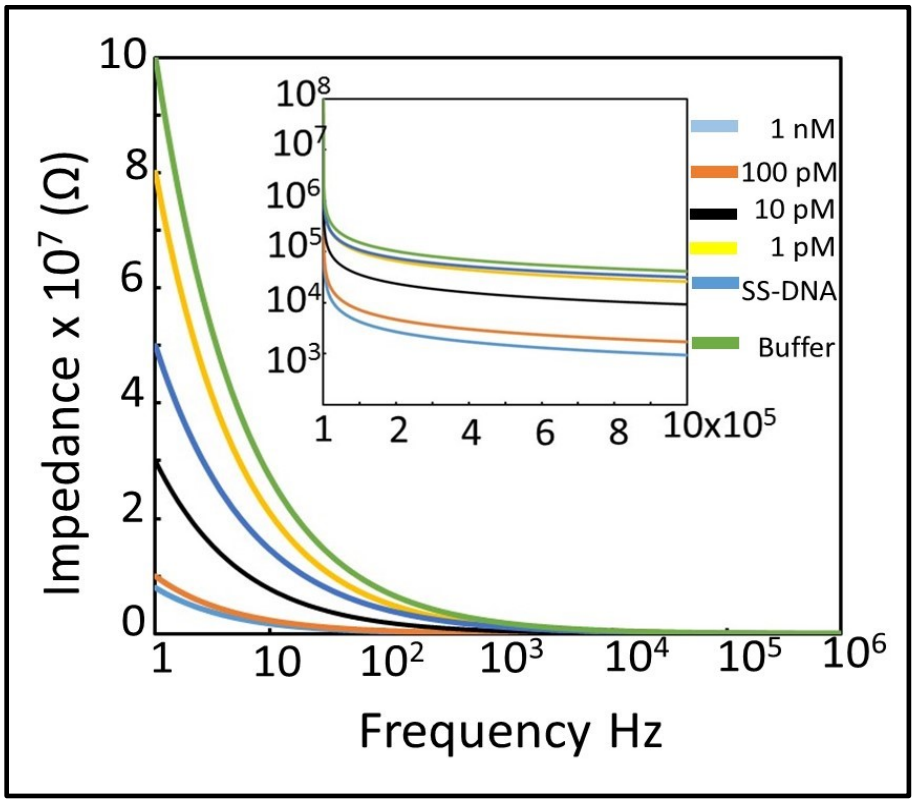

Figure 5.5. Analysis of impedance data from Let 7b-miRNA-DNA, let 7b-miRNA, and complementary DNA molecules to let 7b.
This figure shows the impedance spectra in the low-frequency region (1 Hz to 5 kHz), and the inset shows the impedance spectra in the high-frequency region (5 kHz to 1 MHz). Note that the impedance spectra in the high-frequency region are highly dependent on the molarities of target let 7b-miRNA-DNA molecules.

Next, we studied how molecular concentration within the device (between TIEs or on TIEs) contributes to the impedance spectroscopy. We have performed all three steps of the detection and quantification assay stated above on the spiked let-7b-miRNA molecules in 0.01 × TE buffer. We hybridized let-7b miRNA with complementary DNA molecules, pipetted about 10 μL of sample on the device, applied an electric potential of 10 Vpp at 1 MHz, and measured the impedance spectroscopy (Figure 5.5). Note that impedance values are not always proportional to target miRNA-DNA molarities in the low–frequency region (Figure 5.5). On the other hand, in the high-frequency region (Figure 5.5 inset), the impedance values are correlated to the miRNA-DNA concentrations. We believe that miRNA-DNA molecules that are concentrated between TIEs contribute to the measured reactance values. To demonstrate the feasibility of using the electrical impedance to quantify the target biomarkers, we have separately spiked let-7b miRNA molecules (0–1 nM) to 1/100 and 1/1000 diluted commercially available serum samples (Innovative Research, Novi, MI), then hybridized let-7b with complementary DNA molecules (1 ng); separated let-7b miRNA-DNA duplex molecules from other non-target miRNA and free DNA molecules; concentrated the let 7b-miRNA-DNA duplex molecules between TIEs (10Vpp, 1MHz); and measured the electrical impedance (10 mV, 0–1 MHz) and the phase at each frequency with the spiked molarity of let -7b miRNA. Similarly, we have extended our experiments and detected IL-6 molecules in diluted (1/100 and 1/1000) serum samples. We also found that lower dilution factors greater than 1/100 cannot be used in our device because, at higher conductivity values, dielectrophoresis of molecules is not produced and/or the significantly higher temperatures produced in the solutions could disintegrate or degrade the biomolecules. We calculated the limit of detection (LOD) and sensitivity values for let 7b-miRNA and IL-6 molecules spiked into 1/100 and 1/1000 serum samples (Table 3.1 and Table 3.2). Note that the fM values for LOD and high

sensitivity values (10^{12} Ω/M or more) were obtained for let 7b-miRNA. In comparison, traditional impedance sensing techniques (that chemically attach complementary DNA molecules on the glass substrate between interdigitated electrodes, hybridize target miRNA, produce miRNA-DNA duplex, and measure the impedance spectrum) have reported pM for LOD values (Table 3.2). Similarly, fM values for LOD and sensitivity values in 10^{12} to 10^{15} Ω/M were experimentally obtained for detecting spiked molarities of antigen IL-6. It has been reported that LOD of ELISA is about 30 nM. In experiments, first, antibody and antigen molecules were mixed in the ratio of 10:1, respectively. The mixture was briefly mixed by vortexing, and the sample was kept in the ultra-rocker at room temperature for about 20 min. The sample was then added to 1/100 or 1/1000 diluted serum samples. About 10 μL of sample was pipetted on the TIE electrodes. We then applied electric potential of 10 Vpp at 600 kHz for about 10 min to separate conjugated antigen-antibody from other molecules and concentrate between electrodes. Finally, electrical impedance spectrum of the sample was measured and recorded.

Table 5.1. Performance values (limit of detection and sensitivity) produced by the device in measuring let 7b miRNA molarities that spiked into diluted serum samples.

Frequency	Limit of Detection (LOD)		Sensitivity(Ω/M)	
	(1/100) Serum	(1/1000) Serum	(1/100) Serum	(1/1000) Serum
1Hz-1kHz	84±4.3 fM	49±23 pM	(1.1±1) x10^{15}	(1.1±1) x10^{14}
1kHz-1MHz	220±47fM	79±52fM	(4±2) x10^{16}	(4.6±2.4) x10^{12}

Table 5.2. Performance values (limit of detection and sensitivity) produced by the device in measuring IL-6 antigen molarities that spiked into diluted serum samples.

Frequency	Limit of Detection (LOD)		Sensitivity(Ω/M)	
	(1/100) Serum	(1/1000) Serum	(1/100) Serum	(1/1000) Serum
1Hz-1kHz	75.44±45.9 fM	4.36±2.2 pM	(1.5±0.7) x10^{15}	(5.65±5.0) x10^{16}
1kHz-1MHz	6.09±4.3 pM	44.78±44.5 fM	(6.01±4.7) x10^{13}	(2.62±2.2) x10^{12}

5.4. Conclusions

We have demonstrated the proof-of-concept of a potential universal biosensing technology that could detect clinically relevant biomarker levels (< 1 pM) directly in diluted serum samples. Moreover, in this study, we have demonstrated the detection of miRNA and antigens could also be done. Also, the utilization of DEP allowed us to avoid the surface modification steps discussed in chapter 4. In addition to these biomarkers, our universal biosensor could also be used to detect and quantify circulating short DNA molecules. Austin's group has previously demonstrated differential dielectrophoretic forces for double- and single-stranded long DNA molecules (> 1 kb) at low frequencies [27]. Therefore, long DNA molecules could also be detected by the proposed method. It is important to note that the conductivity of the sample buffer plays critical roles in thermophoresis, dielectrophoresis, and electrical impedance. Moreover, to be effective, the conductivity of the buffer must be low (~0.01 × TE). For example, if serum is used in assays, it is necessary to dilute the serum by at least 100 times to achieve proper conductivity.

Generally, in clinical assays, it is necessary to detect single or multiple biomarkers (up to about 3–4 biomarkers) in a single assay [214],[215],[237]–[239]. To detect multiple biomarkers, samples need to be divided into equal volumes, and multiple devices could be used for each target. Since the fabrication cost a device is about $15, use of multiple devices in a single assay is not cost-prohibitive. The device uses up to 10 Vpp as the input, with a very high impedance value (>100 kΩ) for the TIEs, therefore consuming very little power (a few mW or less). The biomarker detection time is about 30 min or less, which includes 10 min for hybridization or conjugation, 10 min for separation and concentration of target molecules, and 5–10 min for impedance measurements. To be useful and applicable in clinical assays, specificity and sensitivity of the biomarker detection must be very high. In the nucleic acid and antigen biomarker detection,

specificity is controlled primarily by the target and complementary conjugation step (Step 1) that is performed outside the device. Studies have reported that conjugation of target biomarker with its complementary molecules can be optimized to significantly reduce the false positives [57]. Also, if the current sensitivity and specificity are not sufficient, one can utilize a commercially available antigen, miRNA, or DNA isolation kits and isolate the biomarkers of interest, suspend molecules in low conductivity buffer (e.g., 0.01xTE), and perform the detection. Such molecular isolation could decrease the molecular crowding near TIEs and increase the capture of the target molecules between TIEs, which would improve sensitivity and LOD values.

CHAPTER 6. DIELECTROPHORESIS BASED MICRO ELECTRODE APPROACH TO AUTOLOGOUS CAR T CELL MANUFACTURING

6.1. Introduction

As discussed in Chapter 1, section 1.3.3. CAR (Chimeric Antigen Receptor) T-cell therapy has emerged as a powerful therapeutic method, with evident prominent results in treating acute lymphoblastic leukemia (ALL) and diffuse large B-cell lymphoma (DLBCL) [103]–[105]. The CAR molecule will produce an antigen targeted antibody on the T-cell surfaces, which can recognize the antigen-presenting cells. The CAR is a synthetic molecule that will be produced in-vitro and be transcribed into a viral vector or encoded into an mRNA. Then, the engineering of T-cells using CAR molecules is done by effectively transfecting them into the cells. The ideal method of transfection should have high transfection efficiency, controllable injection, high cell viability, minimal effects on normal physiology, and be easy to use and be reproducible [240]–[242]. Virus-mediated transfection, which is also called transduction is the current state of the art method in CAR T cell therapy [120],[243],[244],[245]. This method uses the innate abilities of viruses, which will attack the host cells and transfer their genetic materials during their cycle of replication. When it comes to therapy, these viruses will be modified by replacing harmful genes with the desired gene for therapy [243],[246]. Herpes simplex virus, adenovirus, retrovirus, lentivirus, adeno-associated virus, vaccinia virus, and sindbis virus are some of the examples for the commonly used viruses and virus types in the therapy [120],[240]. However, there are a few major drawbacks involved in this method. The random attachment of the genes to the cell's DNA by viruses possibly can cause detrimental mutations which can worsen the situation and probably can pass to the next generation, in cases where a patient has a child after the treatments [121],[244]. It can cause immunogenicity and cytotoxicity and can be transmitted from the patient to the others as well. A

great effort, therefore, has been made to develop non-viral transfection methods for engineering cells for therapy.

Recently, a new protocol for generating CAR T-cells was developed by CAR-mRNA electroporation, rather than viral transduction [101],[247],[248]. Use of mRNA transfection has the advantage of mitigating permanent gene modifications and results in only transient expression of the CAR [101],[247]. Further, this electroporation is less time- and resource-intensive compared to the viral vector-based methods. Electroporation is the process of creating pores in cells using externally applied electric fields. These pores can be created in such a way that they can be resealed after a short period [30],[102],[249]. During the very short time of milliseconds these pores are opened, one can easily transfect small biomolecules like DNA, RNA, or drugs into the cell [250],[251]. The electroporation phenomenon has been possible due to very thin cellular membranes, typically between 5nm-10nm [252]–[254]. This non-polar thin layer creates an insulated barrier between the interior and the outside of the cell. Therefore, once an external electric field is applied to a cell the insulated barrier will experience a very high electric field, which at some point can alter the arrangement of the phospholipids and create aqueous pathways into the cells [32],[255],[256].

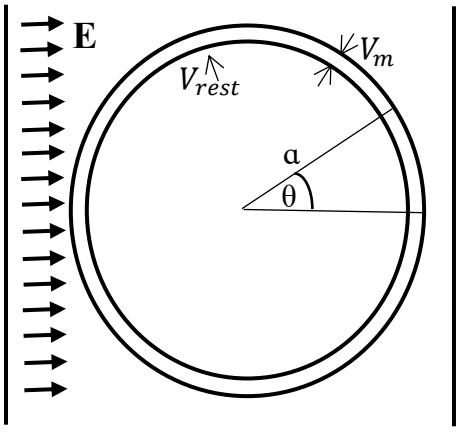

Figure 6.1. Single-cell exposed to a uniform external electric field.

When a single cell is exposed to an external electric field, as in Figure 6.1, the induced transmembrane potential (V_m) at a given location on the cell circumference (θ) is given by equation 6.1.

$$V_m^{\theta} = 1.5Eacos\theta + V_{rest} \quad (6.1)$$

Here, E is the applied electric field magnitude, a is the radius of the cell, and V_{rest} is the resting transmembrane potential, which is typically ~ -80mV for a normal cell. It has been proved experimentally that pore creation happens when the transmembrane potential exceeds a threshold value ~1V [30],[257],[258]. From the equation 6.1, it is evident that the induced voltage at different areas of the membrane varies and pore creation starts where the cell experiences the highest electric field. Also, smaller cells will need higher electric fields for electroporation compared to the bigger cells. By varying these parameters, electroporation can be calibrated according to the cell type and be used for transfecting cells.

However, conventional electroporation method uses bulk electroporation, where millions of cells are electroporated using two electrodes in a cuvette setting [110],[138],[139]. In the bulk electroporation setting, the aforementioned parameters are not optimized at the single-cell level but use an average value for all the cells [110],[138],[139]. Bulk electroporation reports a very low throughput (30%-40% out of cells used), high cell death (60%-70% out of cells used) and inefficient transfection (20%-30%) [110],[138],[139]. To obtain a quality engineered CAR T-cell sample, it is necessary to optimize electroporation in a single-cell.

To address the issue in mRNA electroporation, here we report a microelectrode array-based miniaturized technology utilized with DEP, for controllable and effective electroporation. The utilization of DEP allows cells to be positioned in the microelectrode array and experience the optimized electroporation conditions at the single-cell level. The technology was successfully

utilized in CAR mRNA transfection. Results show an improved transfection efficiency, controllable transfection, improved CAR-expressing time, faster target cell lysing, and higher viability after electroporation over the conventional methods.

6.1.1. MEA manufacturing

COMSOL Multiphysics 5.3a was used in this study for designing electrodes. Spatial distribution of the electric field and electric field intensity were simulated using COMSOL with various electrode designs prior to manufacturing, to obtain optimum results. To setup COMSOL simulations, briefly, interdigitated electrodes were drawn to scale using AutoCAD (Autodesk) software. Then it was imported into COMSOL and simulated with AC/DC electric current (ec). The device contains planar gold microelectrodes that were manufactured on a commercially available glass substrate, using traditional photolithography based micro-fabrication techniques. Electrodes are about 100 nm in height and different electrodes with different width and gap ratios were manufactured based on the cell type (will be discussed in later part in results and discussion).

6.1.2. Culturing cell lines

Acute T-cell leukemia (Jurkat) cell line, acute lymphoblast leukemia (SUP B15) cell line, and human CD8 T-lymphocyte cells were used in the experiments. Jurka, which is a T-lymphocyte cell line was chosen for the initial T-cell transfection experiments to validate the concept. We cultured the cells in an incubator with 5% CO_2 with RPMI media with 10% fetal bovine serum (FBS) and 1% pen-strep (Penicillin-Streptomycin) by volume.

SUP-B15 acute lymphoblast leukemia (ALL) cell line was used as the target cells in cytotoxicity assay, which respond to CD19 antigen targeted CAR T-cells. The cell line was purchased from ATCC and was cultured in Iscove's Modified Dulbecco's medium with 4 mM L-

glutamine adjusted to contain 1.5 g/L sodium bicarbonate and supplemented with 0.05 mM 2-mercaptoethanol, 80%; fetal bovine serum, 20% and incubated at 37 °C and 5% CO_2.

Chronic myelogenous leukemia (K-562) cell line was used as a non- target cell line for cytotoxicity assay using CD19 antigen targeted CAR T-cells. The cell line was purchased (ATCC Manassas, MA) and cultured in RPMI 1640 medium supplemented with 2 mM glutamine and 10% FBS (by volume). Cells were cultured in an incubator at 37 °C with 5% CO_2.

6.1.3. Isolating human CD8 T-cells

Human primary CD8 T-cells were used as the effector cells in the cytotoxicity assay in the final experiments. CD8 cells were isolated from human blood samples purchased from Innovative research, Novi, MI. To isolate the CD8 T-cells from a blood sample, 20 mL of ficoll paque was added to a 50 mL centrifuge tube. Then 10 mL blood sample was slowly pipetted on to the ficoll paque layer. The solution was then centrifuged for 30 min at 24 °C at 400 x G. Following the 30-minute spin, the blood was separated into distinct layers. To ensure the collection of all the CD8 cells, the entire top layer, which was approximately 6 mL of the sample, was obtained and placed in a 15 mL centrifuge tube. The sample was topped to 15 mL with sterile 1x phosphate buffer solution (PBS). The tube was placed back into the centrifuge and was spun for 5 minutes at 24 °C and 300 x G. The supernatant was poured out of the centrifuge tube and the cells were noted to be red. To get rid of any remaining red blood cells (RBC), 3 mL of RBC lysis was added to the pellet and vortexed on setting 5 for 3 minutes. The sample was topped to 15 mL with PBS and put into the centrifuge for 5 minutes at the same settings, following the same procedure. The initial count of the cells was $9.0x10^7$ in about a 2 mL solution. Following the count, 15 mL PBS was added to the sample and the cells were put back in the centrifuge for a final 5-minute spin at the same settings. After removing the supernatant, 1.6 mL of EasySep buffer which came with the CD8 T-

cell isolation kit, was added to the cells and mixed. The directions on the kit were followed to finish isolating the CD8 T-cells, using a cocktail mix and magnetic beads. Once the cells were isolated, a final count was observed to be $3.45x10^6$ cells. To quantify cell viability following isolation, trypan blue was used as a stain on the hematocytometer. The viability of the CD8 T-cells was found to be 92% upon isolation.

6.1.4. Cell patterning experiments

Cell patterning was done by subjecting cells to dielectrophoresis force through the microelectrode array device. Through a series of experiments, it was found that the effective condition for patterning cells is negative dielectrophoresis, which makes the cells to form a line in between the parallel electrodes. The optimum buffer for patterning and the electroporation is 0.01xPBS with the conductivity of 0.03 S/m. Buffers were prepared once a week for experiments. To make the buffer, 1 part of RNAse free 10xPBS (Invitrogen PH 7.4) was mixed with 999 parts of RNAse free DI water (Invitrogen) and then the osmolarity of the solution was adjusted to 180 mOsm/L using RNAse free D (+) Sucrose. Cells were extracted from the culture flasks and spun down at 500 g for 5 min and washed twice with the above-mentioned buffer. Finally, the cells were collected in the same buffer approximately with a concentration of $1x10^6$ -$2x10^6$ cells/mL. Then, the MEA device was cleaned using RNaseZap (Thermofisher Inc.) to get rid of RNAse that can degrade the mRNA. Then, 100 μL of the cell suspension was pipetted on top of the MEA electrodes, and the patterning electric signal was applied to the array (1 Vpp of a sinusoidal signal at 10 kHz). Then we waited for about 10 minutes until the cells settle down and form the pattern.

6.1.5. Cell electroporation

After cells were collected in 0.01xPBS (RNase Free,200 mOsm/l) with a buffer for a cell density of $1x10^6$ cells, they were kept on ice until the experiment begins. Transfection experiments

were conducted by mixing the molecules into the 100 μL of the cell suspension to be transfected into cells. Initially, the experiments were conducted by transfecting PI molecules [Invitrogen, Molecular Probes, OR] at 1 μM for the proof of concept purposes. Then, 8.98 pM of EGFP mRNA [Trilink Inc., CA] was used in transfection to observe the mRNA transfection efficiency and 7.96 pM of CAR mRNA [G&P Biosciences, Santa Clara, CA] was used in final experiments for cytotoxicity and CD 19 expression assays. Then, Transfection experiments were performed in the following conditions for cell electroporation using a commercially available function generator (Tektronix AFG3021B), where we wanted to analyze the effect of patterning vs conventional methods;

(1) Cell patterned with 1 Vpp, 10 kHz sinusoidal and transfected with 3 DC pulses of 9 Vp for 1.5 ms,

(2) Cell patterned with 1 Vpp, 10 kHz sinusoidal and transfected with 3 AC pulses of 8 Vpp, 100 Hz for 150 ms,

(3) Transfected with DC 3 DC pulses of 9 Vp for 1.5 ms without forming single-file cell patterns,

(4) Transfected with AC 3 AC pulses of 6 Vpp, 100 Hz for 150 ms without producing single-file cell patterns,

(5) Cell patterned with 1 Vpp, 10 kHz sinusoidal and transfected with DC fields but no external molecules were present,

After the transfection, cells were collected from the device using a pipette. Then, for PI transfection experiments, cells were directly analyzed using Fluorescence Activated cell sorting (FACs). For the EGFP transfected cell analysis, collected cells were incubated in 5% CO_2, 37℃, and taken for FACs at different time points. For Cytotoxicity assays, electroporated CD8 effector

cells were mixed with target cell SUP B 15 cells with a ratio of 4:1 and incubated in 5% CO_2, 37℃ with IL-2 in media. Then it was taken for FACs at different time points along the time axis to assess the cytotoxicity, by observing the target cell growth.

6.1.6. Fluorescence-activated cell sorting

BD Accuri C6 Flow cytometer consists of a 488 nm excitation laser.FL1 (533/30 nm) and FL2 (585/40 nm) filters were used to capture the emission from Calcein (516 nm) and PI (617 nm) respectively. In order to get to rid of the overlap of the FL1 and FL2 filters, compensation values were used as per the Flowcytometers' vendor specifications. Then the sample core size was adjusted according to the cell diameter. After doing the above adjustments, the data was collected.

For analyzing the cells transfected with Propidium Iodide (PI), cells were collected to 1.5mL tube upon the experiments and stained with Calcein AM (1 µL from 1 µM solution for $1X10^6$ cells) to investigate the viability. Then the samples were kept in ice and flow analysis was conducted.

For analyzing the cells transfected with EGFP mRNA, collected cells were cultured at 37 °C and 5% CO_2 incubator. Then the cell samples were taken at 12 hours, 18 hours, 24 hours, 36 hours, 48 hours, 72 hours, and 96 hours. Then the cells were washed with PBS and 100 nM of PI was added to investigate the viability. Then it was analyzed through FACs.

For analyzing the cells transfected with mRNA; cytotoxicity assay and CD 19 expression analysis were conducted with FACs. There, the cell samples collected at each time point from the incubator were initially mixed with 100 nM of Biotin-SP (long spacer) AffiniPure $F(ab')_2$ fragment goat anti-mouse IgG and incubated on ice for 25 minutes. Then the cells were washed with PBS and added 200 nM of FITC Streptavidin. Then it was incubated on ice for 5 minutes. Thereafter,

the cells were washed with PBS, and 100 nM of PI was added to investigate the viability before analyzing through FACs.

6.2. Results and discussion

6.2.1. Cell patterning

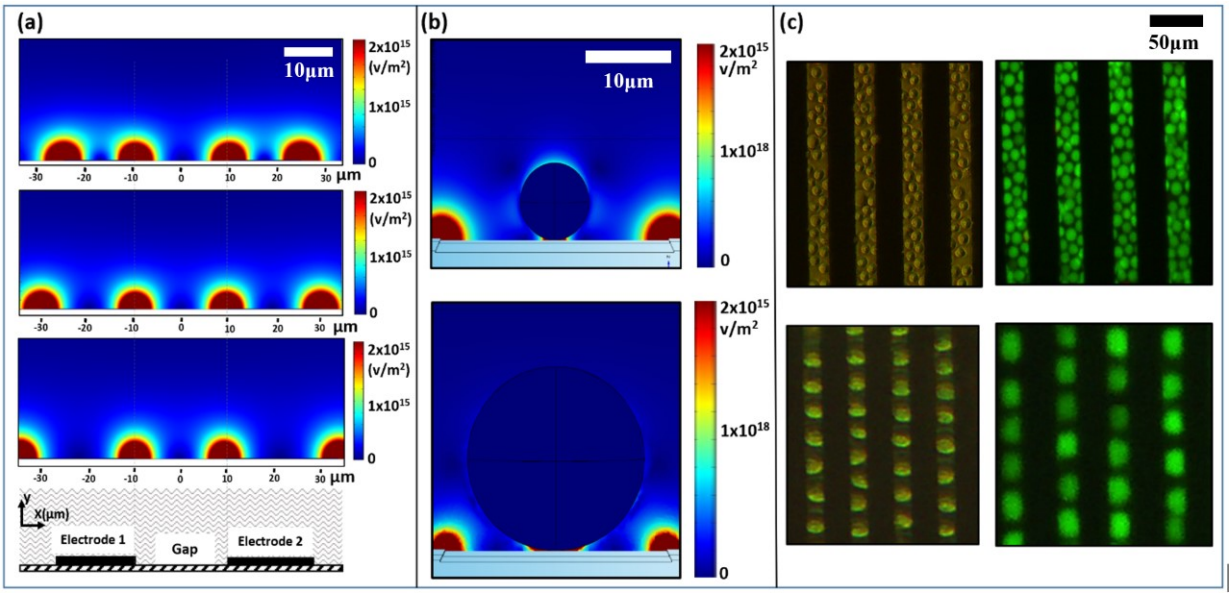

Figure 6.2. Electrode design parameters for effective cell patterning.
a) Effect on the electrode width on cell settling (b) Effect on the gap between electrodes on cell settling (c) Top two figures show bright field and fluorescence images of an incorrect electrode design that can result in cell crowding. Bottom two figures show bright field and fluorescence images of a correct electrode design, which forms a single line of cells.

In this study, we have done a systematic study by conducting simulations to design effective patterning electrodes array, while producing enough electric fields to electroporate cells. Figure 6.2 (a) shows how the width of the electrode and the gap between electrodes determines the cell settling area. Electric field gradient distribution in the electrode level was simulated through COMSOL. Figure 6.2(a) illustrates how the electrode width has been changed while maintaining the gap between electrodes as a constant. As we utilize the negative DEP to trap these cells, cells are placed at the electrode plane, where the electric field gradient is minimum. It was observed that the top configuration is the ideal condition to drive the cells into the gaps as desired.

According to the 3rd figure from the top in Figure 6.2 (a), once the electrode width is increased than the gap, the cell has more tendency to settle over the electrodes. However, with the calculations, it was determined that the electrode width/ gap width ratio should be kept below 1. But, due to the manufacturing restrictions, it is difficult to reduce the width of the electrodes. Also, if the width of the electrodes is reduced, the resistance through electrodes will be increased resulting in potential joule heating as well as electrolysis. Figure 6.2 (b) shows how the relative gap between the electrodes compared with the cell size, contributes to form a perfect line of cells. A modeled cell has been placed in between the two electrodes to observe how the electric filed gradient distribution varies with a cell in between electrodes. The results show that, when the cell size is significantly smaller than the gap width, more than one number of cells settle in the gap, distorting the perfect line of cells. Figure 6.2 (c) shows two such cases. On the top row, it shows the effect of having a bigger gap with smaller cell size and how it results in cell crowding in between the electrodes. The bottom row shows a perfectly arranged line of cells resulted due to the correct dimensions of electrodes. Therefore; based on the different types of cells we used during the operations, we had to come up with several designs for different sizes of cells. For instance, for patterning primary human T-cells (~7 μm in diameter) we used an electrodes gap of 10 μm.

Figure 6.3 (a) shows the contribution of the applied voltage magnitude towards better patterning conditions. The top figure shows the effect of having inadequate electric field values, which result in random cell settling in between as well as on top of the electrodes. The middle figure shows how an adequate voltage level creates more tendency for the cells to settle in-between the electrodes. The bottom figure shows the effect of the voltage value which is higher than the adequate limit. It pushes all the cells away from the electrode surfaces and causes cells to levitate

without settling. Figure 6.3 (b) shows the comparison between the levitating cells (two images in the top row) vs perfectly patterned cells.

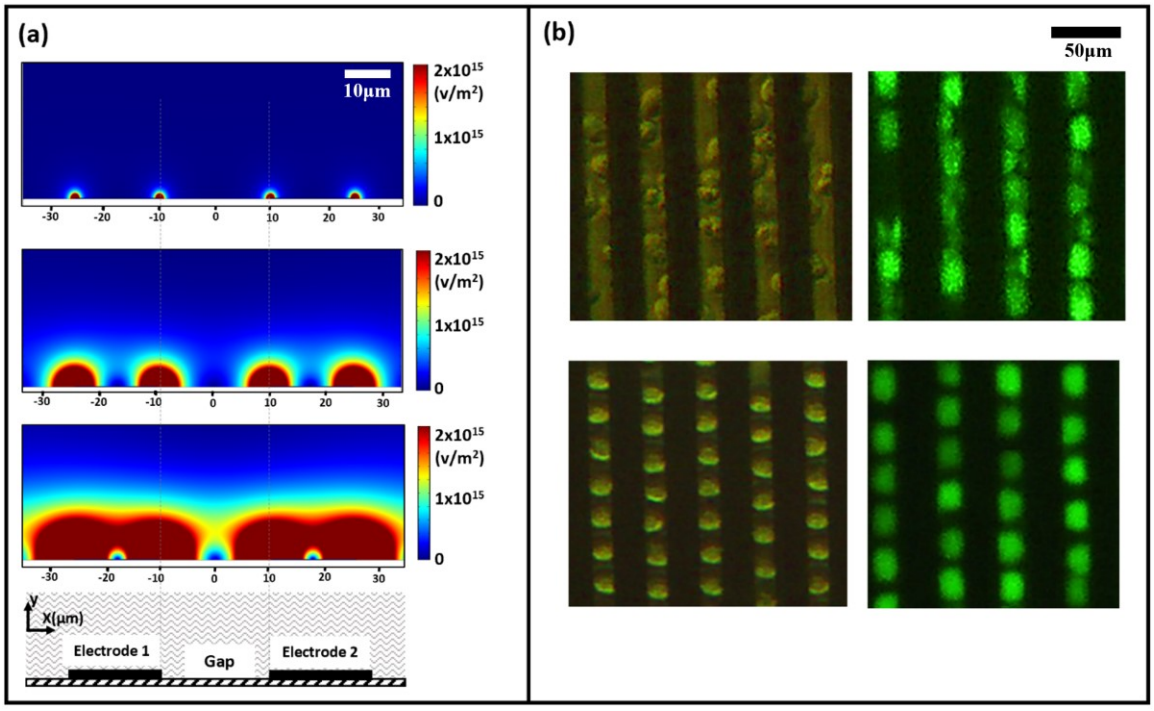

Figure 6.3. Applied voltage contribution for effective cell patterning.
(a) COMSOL simulation showing Electric field gradient variation with different applied voltages between electrodes. (b) Images of the different cell settling configurations with applied voltage, Top two images show floating cells due to the higher voltage applied, bottom two figures show cells which are patterned with perfect patterning conditions.

Thus, when designing a system for cell patterning, all the above-mentioned parameters must be considered. In this research, we have successfully designed a cell patterning system, which can be used to pattern different types of cells with different parallel electrode designs. To pattern cells, negative DEP has been used while the frequency was lying from 10 kHz-50 kHz.

6.2.2. Cell electroporation and transfection of molecules

Our novel approach in effective and controllable electroporation include two steps. Under the first step, the cells are patterned using the DEP. Then, the electroporation pulse is applied using AC and DC pulses that produce adequate energy to electroporate cells reversibly. The steps are as below in Figure 6.4.

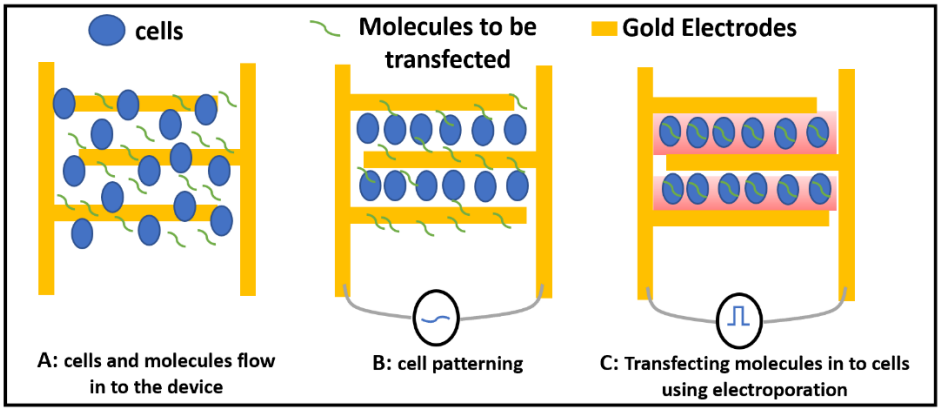

Figure 6.4. Cell electroporation steps using our approach.

In this approach, initially, simulations were conducted using COMSOL to access the effect of patterning on the induced transmembrane potential, by the applied electroporation field. There, the induced transmembrane potential was obtained from COMSOL software by using models of cells with different configurations, as discussed in equation 6.1. Then it was compared with the cuvette electroporation conditions. As shown in Figure 6.5 it is evident that the patterned case has more uniform induced transmembrane potential which lies around 1 V, when comparing with the non-patterned case. The non-patterned case has more variation in the transmembrane potential. As it was mentioned in chapter 1, this causes certain cells to go to the irreversible electroporation state while some other cells will not have enough voltage to electroporate. Thus, patterning gives salient advantages to uniformly electroporate cells.

Figure 6.6 then, compare the proposed technology with the traditional cuvette electroporator. Figure 6.6 (a) shows the distribution of higher induced transmembrane potential, which shows that in the proposed method, the electroporation is happening locally in a targeted area, yet uniformly in every cell. Then, Figure 6.6 (b) shows the traditional electroporator which has more exposed areas with induced transmembrane voltages, which vary from cell to cell. The results in Figure 6.6 further explain the variable induced transmembrane potentials in traditional

electroporator. Thus, it is evident that compared to the traditional electroporators the developed approach is capable to produce more viable cells as well as controlled transfection.

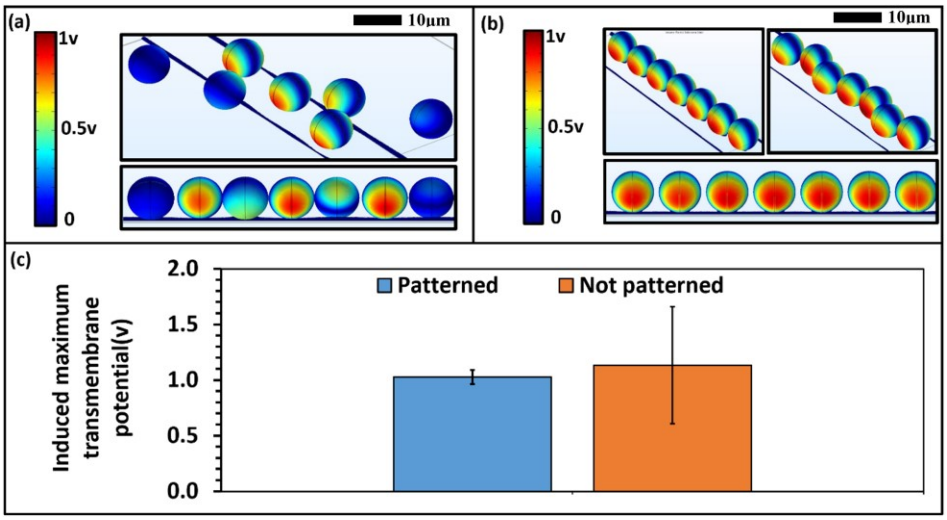

Figure 6.5. Comparison of induced membrane potential with patterned and not patterned cells. (a) Simulation of cells randomly scattered on and among electrodes (b) perfectly patterned cells in between electrodes. (c) statistical comparison of maximum induced transmembrane potential between two cases.

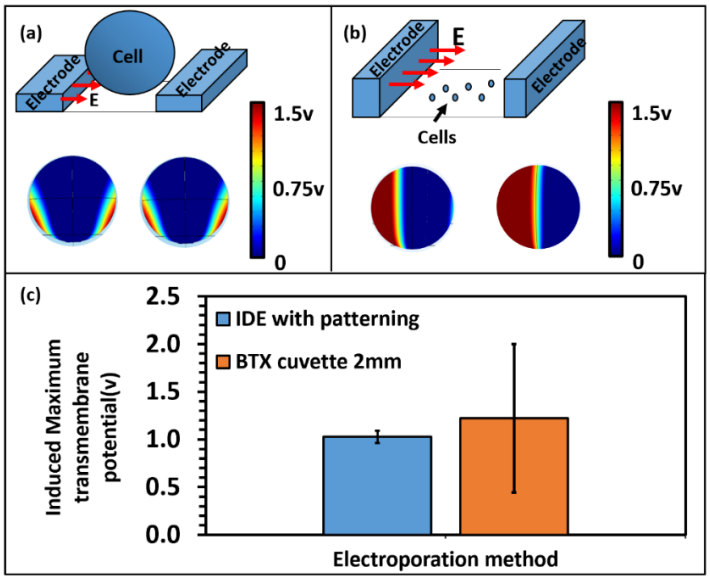

Figure 6.6. Comparison of the induced transmembrane potential of the proposed device and traditional cuvette electroporator.
(a) Simulated induced transmembrane potential in cells of proposed electroporation technology which shows localized electroporation region. (b) Simulated induced transmembrane potential in cells using conventional electroporator BTX cuvette 2 mm.

Upon conducting simulation studies, we moved into conducting experiments using cells. Initially, the experiments were conducted with DC and AC electroporation pulses using Jurkat cells, because of its close resemblance to T-cells. Propidium Iodide was used in transfection initially, to assess the uptake of the molecules, following calcein assay for viability studies (the procedure is mentioned in materials and methods). The transfection was assessed visually using a fluorescence microscope as well as through FACs and the results are shown in Figure 6.7. Initially, the concept was monitored under the microscope as PI instantly binds to the nucleus of cells, if it can penetrate the cell membrane. This can be visually observed through a microscope.

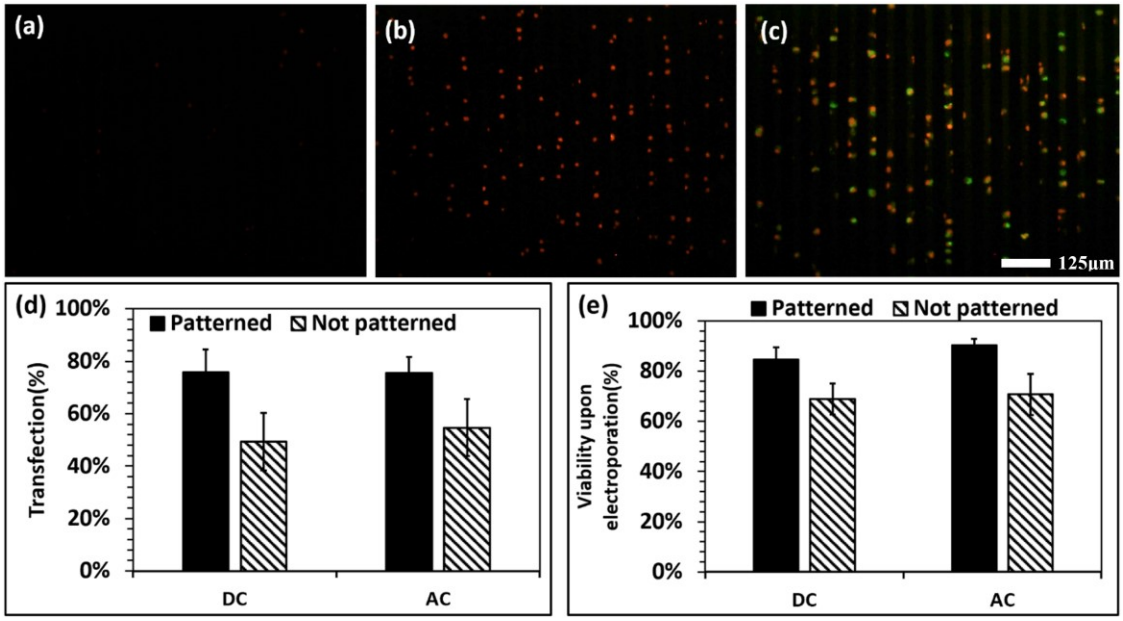

Figure 6.7. Results from PI transfection with Jurkat cells.
(a) Fluorescence image of the electrode device before applying the electroporation pulse. (b) Fluorescence image of cells after applying electroporation pulse. (c) The electroporated cells after adding Calcein for viability assay. (d) Statistical analysis of transfection efficiency assessed by FACs results using five experiments. (e) Statistical analysis of viability assessed by FACs results using five experiments.

Figure 6.7 (a) shows the fluorescence image prior to electroporation, which indicates that there are no electroporated cells or any dead cell in the initial sample. Then, Figure 6.7 (b) shows the fluorescence image of cells just after the electroporation signal is applied, which indicates that

the PI molecules were able to transfect into the cells. This penetration of PI molecules can occur due to two reasons, either because the cells died with the application of electroporation signal and the membrane got compromised or because of successful irreversible electroporation. To assess that, we used the calcein assay. As shown in Figure 6.7, the electroporated and viable cells express both green and red signals from PI whereas Calcein and dead cells are only shown in red color. Figure 6.7 (d) and (e) shows the assessed results using FACs analysis with repeated experiments. Patterned and electroporated cells reported transfection efficiency of ~80% using both the AC and DC electroporation while the non-patterned cells only had an efficiency of ~50%. The viability of the cells also reported a considerable difference between the patterned (~90%) and not patterned cases (~70%) under both electroporation methods.

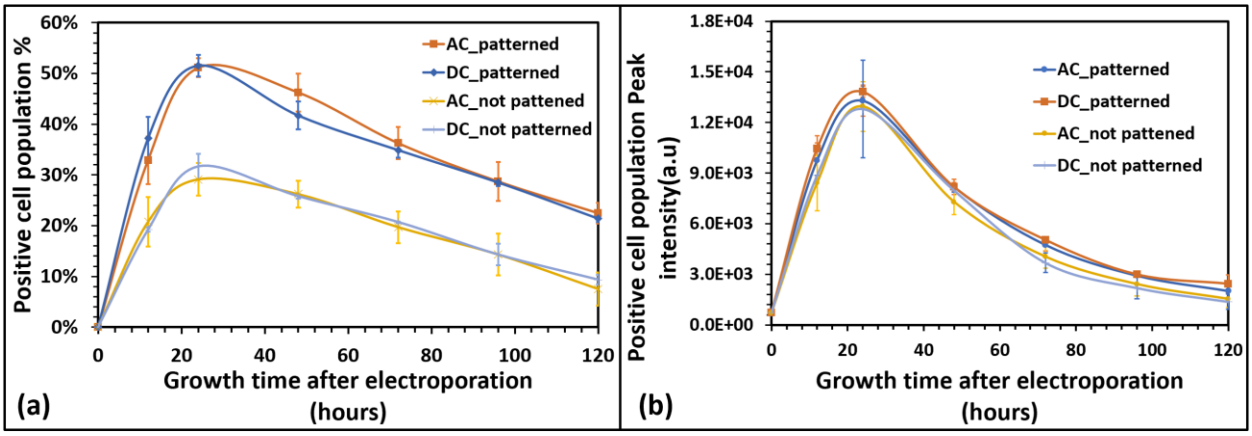

Figure 6.8. Results of EGFP transfection with CD8 T-cells.
(a) Positive cell population expressing EGFP along with time for cells electroporated after patterning. (b) Peak intensity of EGFP expression variation along with time for cells electroporated after patterning.

Upon successful evaluation of the advantages in utilizing the novel approach to transfect molecules into Jurkat cells, the transfection of mRNA into primary T-cells was tested. Initially, Enhanced Green Fluorescence Protein mRNA molecules were used to access the ability of mRNA transfection. Furthermore, mRNA expression along with time was also observed to assess the ability of the novel approach to expand the expression time. Similar electroporation conditions

used in Jurkat cells were used in CD8 cell experiments, where cells were electroporated with AC and DC electroporation conditions with and without patterning. 50 µg/mL of mRNA was used in each experiment. Figure 6.8 (a) shows the EGFP transfected positive cell population analyzed through FACs with each transfection condition along the time. We were able to witness the highest transfection of ~55% in both the AC and DC electroporation conditions with patterning whereas the not-patterned case only reported about ~30% in the transfection. Furthermore, with the results shown in Figure 6.8(b), in terms of the EGFP expression, represented by the fluorescence intensity shows a higher intensity at 120-hour time point for patterned conditions over not-patterned conditions. Therefore, the expression will last longer in the patterned and electroporated conditions. These data provide an insight into the positive effects of patterning incur on the effective mRNA electroporation.

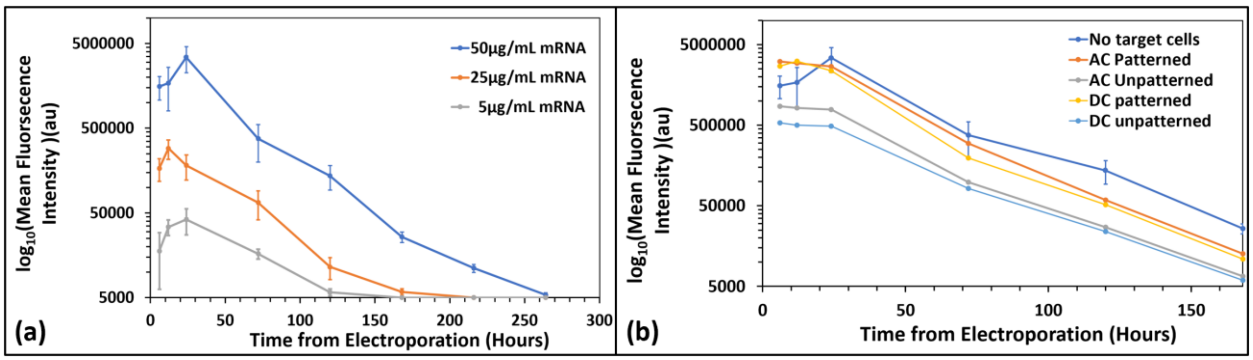

Figure 6.9. CD19 expression along time with electroporated CD8 cells.
(a) Mean fluorescence intensity of CD19 expression along with time with different mRNA concentrations at electroporation. AC electroporation was used upon patterning in these experiments. (b) Mean fluorescence intensity of CD19 expression along with time with different electroporation conditions, when co-cultured with target cells.

After using EGFP mRNA, CAR mRNA (G &P Biosciences) that produce anti CD19 CAR on the cell surface were used in the experiments. The experiments using CAR molecules to assess CD19 expression were done to test two major hypotheses; The ability to expand the CD19 expressing time of CAR of mRNA by increasing the mRNA concentration at electroporation, The

ability of the novel approach over the not-patterned conventional method to expand CD19 expression time. To test the first hypothesis, an isolated CD8 T-cell sample was tested with AC electroporation condition upon patterning with different concentrations of mRNA. Figure 6.8 (a) shows the CD19 expression assessed with the time, after electroporating with several mRNA concentrations at the initial electroporation cell mixture. It is evident that when the concentration is increased, the CD19 expressing time has increased. According to Figure 6.9 (a) an increment of concentration by 10-fold has increased the expression time from almost 100 hours. Therefore, one can increase the mRNA-CAR expression time by increasing the initial mRNA concentration of the electroporation sample. Figure 6.9 (b) shows the experiments conducted on testing the second hypothesis. In this experiment, we tested the CD19 expression of the CAR T-cells with the target cells present in the cell sample. It will demonstrate the real-world application of CAR T-cells attacking cancer cells and CAR expression degradation. Then, we compared it with CAR expression of CAR T-cells along the time without target cells present (4:1 ratio of target: effector cells). Figure 6.8(b) demonstrates that when the target cells are present, the CAR expression started earlier and degrades faster. It demonstrates that when the target cells are present CAR T-cells are likely to respond quickly and start killing cancer cells utilizing more mRNA. Then, we can see a significant difference in the CD19 expression between patterned and not-patterned cases after 168 hours, demonstrating that the cells that were patterned and electroporated will express CAR mRNA for a longer time compared to not-patterned case.

In order to test on the cytotoxicity induced by the engineered CAR T-cells using the novel approach, SUP-B15 (CD19+) target cells and k562 (CD19-) non-target cells were utilized in the experiments. In cytotoxicity experiments, CAR T-cells and tumor cells were co-cultured in a 24 well-plate and the cell number of the tumor cells was monitored over time using FACs.

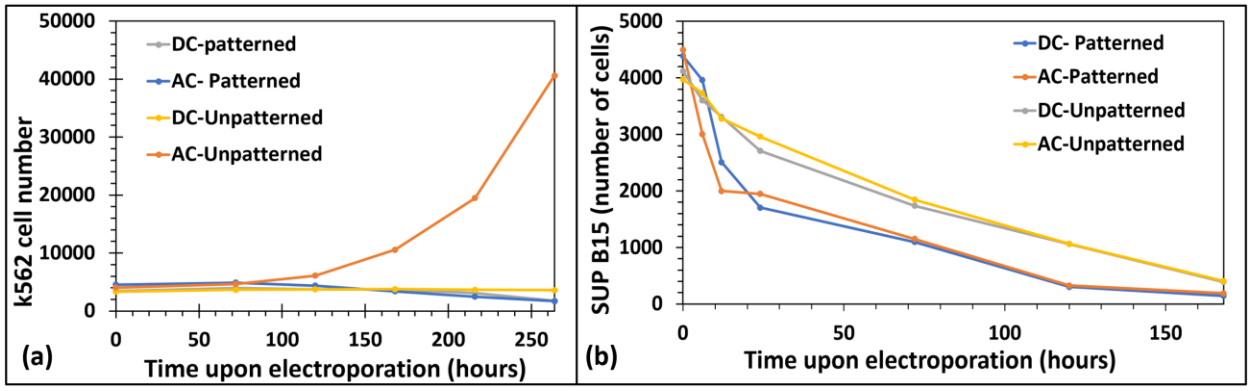

Figure 6.10. Cytotoxicity data.
(a) Cell number variation of the non-target cells with time. (b) Cell number variation of the target cells with time.

Figure 6.10 shows the cytotoxicity data for both non-target and target cells. As shown in Figure 6.10 (a), non-target cells have experienced a non-specific killing and even after 264 hours upon electroporation we still could see a considerable amount of tumor cells are left in the cell sample. Figure 6.10 (b) demonstrates a successful killing of target cells, where the cell numbers were drastically reduced within a very short period. We can see a specific killing of target cells wherein every electroporation condition target cells are being killed faster. When we compared the killing rate of CAR T-cells electroporated with patterning over the CAR T-cells electroporated without patterning, we can see a rapid killing of the patterned and electroporated cells. Therefore, the demonstrated CAR T-cells produced by novel technology are capable of rapid killing compared to conventional electroporation technologies.

6.3. Conclusion

In conclusion, we have demonstrated the successful implementation of a microelectrode device to effectively produce non-viral CAR T-Cells. In this work, we initially did a proof of concept of the novel technology through finite element simulations. Then, we demonstrated the proof of concept through the Jurkat T-cell line that can be cultured in the laboratory by transfecting PI molecules. Later, T-cells were isolated from the human blood and we demonstrated the real

avenues of the novel technology through CAR mRNA transfection and cytotoxicity assays. The utilization of microelectrode arrays with DEP cell patterning enabled the device to improve the transfection efficiency, uniform injection of molecules, higher cell viability upon electroporation, and the capability to transfect more molecules into cells compared with conventional electroporation. These improvements yield the ability in producing CAR T-cells which will have a more CAR-expressing lifetime, which will reduce the number of infusion cycles and much more effective cell killing. Since the fabrication cost of these interdigitated electrodes is below $100 per device, the cost of the therapy can be reduced drastically with a safe non-viral approach.

CHAPTER 7. LABEL-FREE PURIFICATION OF VIABLE HUMAN T-LYMPHOCYTE CELLS FROM A MIXTURE OF VIABLE AND NON-VIABLE CELLS AFTER TRANSFECTION BY ELECTROPORATION[5]

7.1. Introduction

Cell-based therapies, CAR-T-cells, are gaining momentum as a therapeutic strategy for cancer [93],[115],[259]–[261]. CAR T-cells are ex vivo engineered T-cells that express CAR molecules on their surfaces [93],[115],[259]–[261]. The CAR molecule is an antibody derived binding domain that selectively recognizes the target tumor's surface antigen and is directly linked to a signaling domain (such as TCRξ) to provide T-cell stimulation. Once infused into patients, conjugation of the antigen (from the tumor cell) and antibody (the CAR T-cell) triggers T-cell mediated cytotoxicity and kills the tumor cells [93],[115],[259]–[261]. The US food and drug administration (FDA) has recently approved CAR T-cells for treating acute lymphoblastic leukemia (ALL) patients. Approximately 30 million CAR T-cells are required for a single treatment, and typically a patient will undergo about 6–8 treatments or CAR T-cell infusions over the course of a 2–3-month period. Figure 7.1 illustrates the steps involved in CAR T-cell manufacturing and the main focus of this paper. These steps include; drawing a sample of blood from the patient, isolating the T-cells, transfecting the T-cells with. viral vectors that produce CAR molecules on their surfaces, expanding and producing roughly 30 million CAR T-cells and administering the CAR T-cells back to the patient [93],[115],[259]–[261].

[5] The material presented in this chapter was co-authored by Jayasooriya, V. and Nawarathna, D. Jayasooriya conducted experiments and co-drafted and revised all versions of this chapter. Reprinted with permission, from Jayasooriya V. and Nawarathna, D. "Label-Free Purification of Viable Human T-Lymphocyte Cells from a Mixture of Viable and Non-Viable Cells after Transfection by Electroporation". *J. Phys. D. Appl. Phys.* **2019**, *52* (36). https://doi.org/10.1088/1361-6463/ab2b81.)

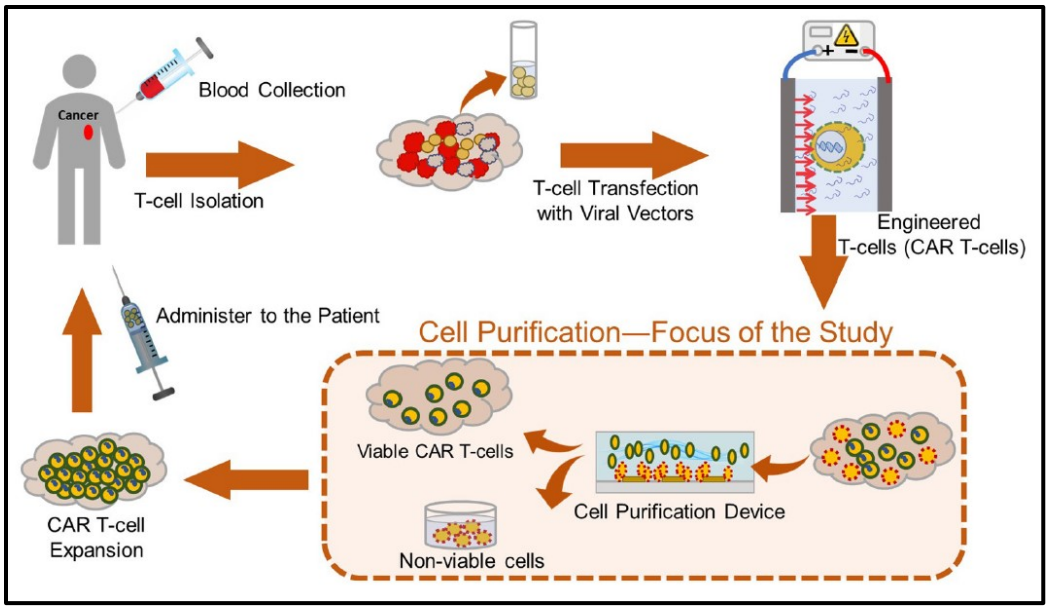

Figure 7.1. The CAR T-cell manufacturing procedure used in cancer immunotherapy.
Isolated T-cells are transfected with viral vectors to modify the T-cell genome and express the antigens that recognize the antibody in cancer cells. Once the antigen and antibody conjugation take place, CAR T-cells are activated and kill the cancer cells. The primary focus of this study is the purification of live cells after transfection by electroporation, which is represented by the rectangle with dashed lines.

To transfect T-cells with viral vectors or electroporation is used. During the electroporation of cells, the T-cells are exposed to short external DC electric field pulses (<1ms) or low-frequency AC electric fields (<1 MHz) [262],[263]. These external electric fields induce electric fields or potentials in the cell membranes of the cells. When the total electric potential exceeds the threshold voltage (typically ~ 1 V), nanometer- scale accessible pathways or pores for external molecules (e.g. viral vectors) are formed on the T-cell membranes. Once these pores are formed, the viral vector molecules that are suspended in the extracellular buffer flow into the T-cells via Brownian motion or via a combination of Brownian motion and electrophoresis [29],[30]. Once the external electric field is turned off, the pore is closed and the molecular flow into the T-cells stops [29],[30]. The electric fields needed for electroporation is produced by suspending T-cells between two-macro or micro-scale electrodes and applying AC or DC electric potentials. In addition, studies

have reported a number of miniaturized versions of electroporation systems in microfluidic channels; these systems are capable of performing T-cell transfection under a continuous flow of cells [31]–[33].

Biological cells are dielectric spheres that can steer external electric fields [34],[264]. When millions of T-cells are randomly positioned between two macro- or micro-scale electrodes, the presence of the cells alters the spatial distribution of the external electric field. As a result, the local electric field near and induced transmembrane potential of each cell varies from cell to cell. The total transmembrane potential, which is the addition of the induced transmembrane potential and resting membrane potential, is directly related to cell viability [29]. As stated above, the total transmembrane potential of roughly 1 V is necessary to produce pores on the cell membrane. Any deviation from 1 V can have significant detrimental effects on the cells, and studies have shown that significant irreversible damage to cell membranes and/or other organelles takes place at voltages >1 V [29]. Such damage can lead to apoptotic or necrotic-based cell death [29]. Therefore, significant numbers of cells are damaged or even killed during electroporation.

In the context of CAR T-cell manufacturing, electric field mediated cell damage is very severe. As a result, very poor cell viability results after electroporation have been reported [123]. For example, studies have shown that T-cell viability after electroporation is about 40% or less [102],[123]. A major technical challenge in CAR T-cell manufacturing is the lack of an efficient and effective method for removing the roughly 60% of non-viable T-cells. Non-viable (dead or dying) cells can significantly interact with living cells and tissues [140],[141]. For example, a process called ‘compensatory proliferation’ has been identified in which dying cells stimulate the proliferation of neighboring cells. In addition, studies have demonstrated that dying cells can also induce rapid stem cell differentiation [140],[141]. Such biological effects in a tumor could enhance

the growth of tumor cells, rendering CAR T-cell therapy detrimental to cancer patients. In addition, if dying cells induce proliferation in other immune cells, diseases such as autoimmune disease could ensue. For these reasons, there is an urgent need to remove dead or dying cells from cell samples and purify the CAR T-cell samples prior to expansion or infusion into patients.

Traditional cell purification techniques such as fluorescence- activated cell separation (FACS) and magnetic-activated cell separation (MACS) require unique target molecules such as a surface antigen or proteins on the cell surfaces to attach fluorophore tags or magnetic beads [142],[143]. The direct use of FACS in therapeutic applications is questionable because the FACS tubing cannot be changed from sample to sample. Therefore, cross contamination could occur from running multiple patient samples. For this reason, the FDA never approved FACS to be used in biomanufacturing. While there are magnetic beads that conjugate with apoptosis-mediated phosphatidylserine (PS) molecules on cell surfaces, there are no known magnetic beads for necrosis. Therefore, MACS is unable to completely purify a cell sample. Another issue with MACS is that it requires additional steps to remove magnetic beads before expansion or infusion into patients. Removing the magnetic beads requires additional assays; complete removal of magnetic beads may be challenging in clinical settings.

To purify cells after the electroporation, in this work, we investigated the use of dielectrophoretic cell separation (DCS). This technique has been applied in biomedical engineering [47],[265]–[267]. Some of its applications include the isolation of circulating tumor cells, platelets bacteria in blood and other biological fluids and analysis of proteins [55],[231],[268]–[271]. However, there have been no reports of DCS to separate cells that are identical in phenotype (both target and non-target cells are T-cells) but with different physiological properties (viable versus non-viable T-cells). Dielectrophoretic cell separation uses the

dielectrophoretic force (DEP force) of cells (e.g. viable and non-viable cells) to purify cells in a label-free manner. We have produced a simple microfluidics device that has interdigitated microelectrodes to produce electric field gradients and trap dead/dying cells while live cells flow out of the device without being trapped.

7.2. Materials and methods

Jurkat cells (TIB 152), human T lymphocyte cells, were used in the experiments. Jurkat cells closely resemble T-cells. The cells were gifted from the laboratory of Dr Glenn Dorsam at North Dakota State University. We cultured the cells in an incubator with 5% CO2 with RPMI media with 10% Fetal Bovine Serum and 1% Pen-Strep (Penicillin-Streptomycin) by volume. After 2–3 days of culture, we used the cells in experiments. To prepare the cells for the experiments, we measured their viability and made sure it was at least 99%. We then spun down the cells at 500g for 5 min and suspended the Jurkat cells in 0.01 × Phosphate Buffered Saline (PBS, conductivity: 0.03 S m^{-1}, ChemCruz catalog # SC-362182) to a final concentration of 2 $\times 10^6$ cells mL^{-1}. The cells were stored in ice when not being used in experiments.

To produce non-viable (dead and dying) cells to demonstrate cell purification using DCS, we electroporated cells using both DC pulses and low-frequency (100 Hz) AC electroporation; cell electroporation using both DC and AC electroporation has been widely used in biomanufacturing of cells. To electroporate the cells, we pipetted Jurkat cells on to interdigitated electrodes (IDEs) (200 000 cells) (Figure 7.3(d)). We patterned cells as single files between IDEs to apply electric fields (DC or AC) uniformly across all the cells in the sample. The details of the cell patterning can be found elsewhere [26]. To electroporate cells using DC electric fields, a DC pulse of 12 V (or electric field of 5×10^5 V m^{-1}) was applied for about 1 ms. Similarly, a low-frequency (100 Hz) AC potential of 6 Vpp (or an electric field of 1.25×10^5 V m^{-1}) was applied for about 150 ms.

These values are comparable to the electric field values used in electroporation experiments for manufacturing CAR T-cells [102],[123].

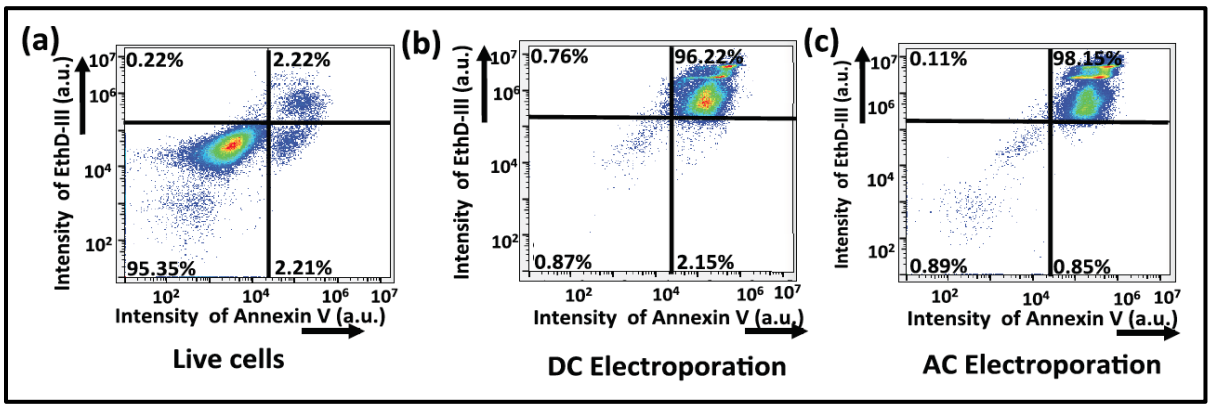

Figure 7.2. Preparation of non-viable cells for the experiments.
To represent all possible electroporation methods used in the transfection, we used DC and AC electric fields. After electroporation, electroporated cells were stained with fluorophore molecules that are representative of apoptotic and necrotic-based cell death. **(a)** FACS analysis of a cell sample before electroporation. Cells are not undergoing apoptotic or necrotic-based cell death, **(b)** FACS analysis of a cell sample that underwent electroporation by DC electric fields. Note that more than 96% cells underwent apoptotic and necrotic-based cell death, and **(c)** FACS analysis of a cell sample that was electroporated by AC electroporation. More than 98% cells underwent cell death by apoptosis and necrosis. We then mixed these cells with live cells and used these mixtures in experiments.

To compare and contrast damage to the cells caused by DC and AC electroporation, we used a commercially available reagent kit to stain the cells and quantify the percentages of cells undergoing cell death through apoptosis and necrosis. Briefly, positive fluorescent signals to Annexin V and Ethidium Homodimer III (EthD-III) indicate the apoptotic and necrotic cells, respectively [272]. Figure 7.2 ((a)–(c)) shows the expression of apoptosis and necrosis biomarkers of the cell samples before and after electroporated using DC and AC electric fields. One can conclude that majority (>90%) of cells that are electroporated using and AC and DC electric fields undergo apoptosis and necrosis. We then mixed the electroporated cells (treated with DC and AC separately) with live cells and performed cell purification experiments. Studies have shown that T-cell viability after electroporation is about 40% [102],[123]. To include all possible scenarios,

we produced cell mixtures by combining live cells with non-viable cells with viabilities ranging from 1%–99%. We kept the final cell count at 2×10^5 cells (viable + non-viable) to avoid cellular crowding over the electrodes during purification. Each cell sample was purified separately, and each purification experiment was repeated at least three times to calculate the statistical significance.

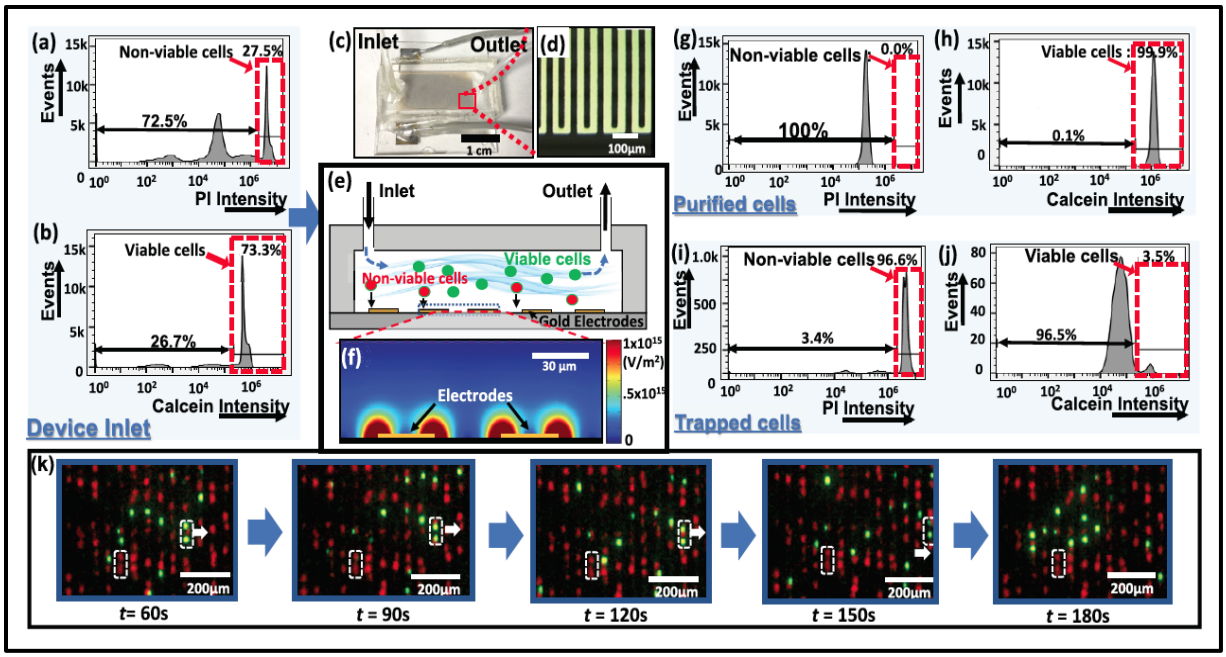

Figure 7.3. Systematic representation of cell purification using DCS after AC or DC electroporation.
(a) and (b) FACS analysis of a cell sample prior to purifying with DEP; roughly 27.5% of the cells were alive. (c) Microfluidics device used in the cell purification experiments (dimensions: length Å~ width Å~ height = 20 mm Å~ 10 mm Å~ .1 mm), (d) Section of interdigitated electrodes used to produce the electric field and electric field gradients necessary for producing the DEP forces on the cells, (e) schematic representation of cell purification device/method, (f) calculated electric field gradient near the electrodes, (g) and (h) FACS analysis of the purified sample that exited the device through the outlet; note that 99.9% of the cells were alive, (i) and (j) FACS analysis of the cell sample trapped in the device; note that about 96.6% of the cells were non-viable, and (k) time-lapsed images of the trapping of non-viable cells (red); note that viable cells (green) were not trapped on the electrodes and did flow into the outlet.

The microfluidics device used in the experiments is shown in Figure6.3 (c) and (d). To manufacture the microfluidics device, we used standard micro-fabrication methods such as photolithography, metal evaporation, lift-off and wafer dicing. The details of micro-fabrication

protocols are reported elsewhere [273]. Briefly, the IDE electrodes were fabricated on a glass substrate, and the flow channel was fabricated in polydimethylsiloxane (PDMS) and bonded together using the traditional oxygen plasma bonding technique [273]. The cell purification device had an inlet and an outlet (Figure6.3 (c)). Cell sample was introduced into device via the inlet with a NE-1002X microfluidics syringe pump (New Era Pump Systems, Inc., Farmingdale, NY). Cell samples were not clustered or grouped during the introduction to the microfluidics channel that has cross-sectional area of 200 mm^2 and the height of the channel was 100 μm. We expect a parabolic velocity profile for buffer solution in the microfluidics channel. To produce DEP force on cells, we used an AC potential (3 Vpp and 5 MHz) applied via a commercially available function generator (Keysight Technologies—33622A). Moreover, we varied the frequency of the AC potential from 0–20 MHz and measured the dielectrophoretic trapping of live and non-viable cells. At 5 MHz, non-viable cells are trapped on the electrode with a large DEP force; at the same time, live cells experience a weak DEP force at 5 MHz. We calculated the expected electric field gradients (COMSOL) near the electrodes (Figure6.3 (f)) and recorded maximum value of 1×10^{15} $V^2\ m^{-3}$; this electric field value produces a maximum attractive DEP force of about 1 nN on a 12 μm diameter cell. We then experimentally determined the buffer flow rate that produced a sufficient viscous drag force to carry (without trapping) live cells to the outlet of the device. The time-lapse images (Figure 7.3 (k)) demonstrate the selective trapping of non-viable cells (shown in red) in the device while viable cells (shown in green) flow out of the device via the outlet channel.

To quantitatively calculate the purity and recovery of the cell sample coming out of the device, we collected the cells coming out of the outlet channel. We also extracted and analyzed the cells that were trapped in the device. To extract the trapped cells, we turned off the DEP force

(by turning off the external potential) and collected the cells by flowing PBS buffer through the device. Briefly, purification measures the ratio between the number of live cells to the total number of cells (live and non-viable cells), and recovery measures the percentage live cells collected at the outlet to the number of live cells entered the device. After running a sample through the microfluidics device, we stained the cells using a commercially available assay to identify the live and non-viable cells. Briefly, live cells have intracellular esterase activity and intact plasma membranes; green-fluorescent calcein-AM staining is used to image the intracellular esterase activity of cells and non-viable cells with compromised plasma membranes, which allow for the influx of cell-impermeant DNA-binding dyes. Once the dye is bound to the DNA of the non-viable cells, they produce a strong orange fluorescence signal [274]. Finally, each sample was analyzed using a commercially available FACS tool (BD Accuri™ C6). The purity and recovery of each sample was calculated using FACS data.

7.3. Results

Figure 7.3 shows the experimental procedures discussed above for the purification of a cell sample that contained 27.5% live cells (Figure 7.3 (a) and (b)) introduced via the inlet of the microfluidics device. An external electric potential of 3 Vpp (5 MHz) was applied to produce a dominant pDEP force on the non-viable cells and capture non-viable cells on the electrodes; the sample flow rate was 7.5 $\mu Lmin^{-1}$. After trapping the non-viable cells in the device, the sample collected in the outlet of the device contained about 99.9% live cells (Figure 7.3 (g) and (h)). We also collected the trapped cells in the device and analyzed them (Figure 7.3 (i) and (j)); about 96.6% were non-viable cells in the device. This result clearly demonstrates the ability of the technology to isolate live cells from other unnecessary and non-viable cells.

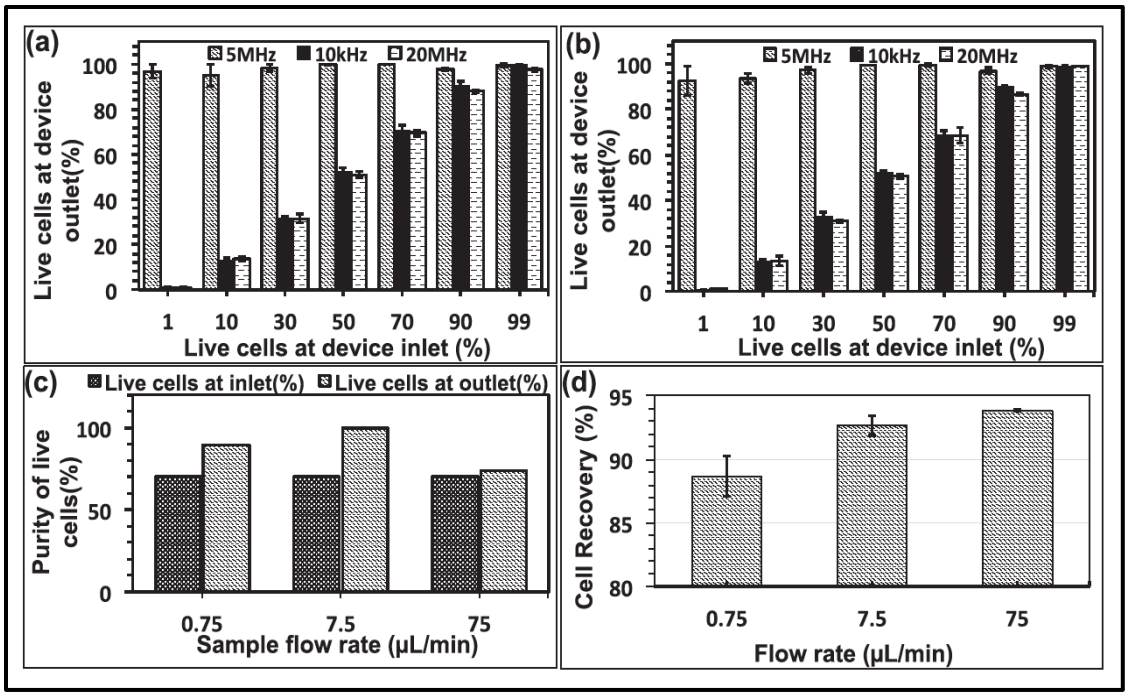

Figure 7.4. The results of the cell purification experiment.
(a) and (b) Variation in the purity of the samples (% of live cells) collected at the outlet of the device with different initial cell mixtures at the inlet and the frequency of the applied electric field used to produce the DEP forces on the cells. In (a), we used DC electroporation to produce non-viable cells and mixed them with viable cells. In (b), we used AC electroporation to produce non-viable cells. The sample flow rate was 7.5 µL min^{-1}, (c) variation in the purity of samples (% of live cells) collected at the outlet with the sample flow rate. A 3 Vpp and 5 MHz electric field was applied in the experiment to produce the DEP forces on the cells, and (d) variation in the recovery of samples (ratio of the number of live cells in the outlet to the number of live cells at the inlet) with the sample flow rate. A 3 Vpp and 5 MHz electric field was applied in the experiment to produce the DEP forces on the cells.

The cell purification in the microfluidics device uses the combination of DEP force and the viscous drag force of cells. We then studied how DEP force and the viscous drag force of the cells contribute to the purity and recovery of the purified cell sample. These experiments also provided information about how identical phenotypic cells with different physiological states produce differential DEP forces (Figure 7.4). Figure 7.4 (a) and (b) show the cell purification results for the cell mixtures varying from 1%–99% non-viable produced using DC and AC electroporation. Note that, regardless of the electroporation (AC or DC) or live: non-viable cell ratio, at 5 MHz, our cell purification method was able to produce cell mixtures at the outlet containing about 100%

live cells. Furthermore, the percentage of live cells in the outlet significantly varied with the frequency of the applied electric field (e.g. 10 kHz and 20 MHz); these results may be due to the fact that at these frequencies non-viable cells experience a weaker DEP force than at 5 MHz or that live cells experience a stronger DEP force. Figure 7.4 (c) shows the percentage of live cells in the cell mixtures collected at the outlet of the device; DEP forces were produced by applying an electric potential of 3 Vpp at 5 MHz. Note that the sample flow rate of 7.5 $\mu Lmin^{-1}$ yielded the best purity of the sample collected at the outlet. At sample flow rates lower than 7.5 $\mu Lmin^{-1}$, a weaker viscous drag force was produced on the cells and therefore some of the live cells were trapped in the device. As a result, there were fewer live cells in the outlet and therefore a reduced purity. Similarly, for higher sample flow rates (>7.5 $\mu Lmin^{-1}$), trapping non-viable cells was not very effective. As a result, there were a large number of dead or dying cells in the outlet. Moreover, our data revealed that almost no purification was observed at the sample flow rate of 75 $\mu Lmin^{-1}$.

Next, we studied the recovery of live cells during the isolation (Figure 7.4 (d)). Low live cell recovery is related to cell loss during purification. If live cells get trapped in the device during purification, the recovery of live cells at the outlet will be significantly less than the number of live cells that entered through the inlet of the device. Therefore, if the sample flow rate is less than 7.5 $\mu Lmin^{-1}$, more live cells will be trapped in the device, thereby decreasing the cell recovery. Similarly, if the sample flow rate is greater than 7.5 $\mu Lmin^{-1}$, larger viscous drag forces wil carry all of the live cells to the outlet, yielding higher recovery values.

7.4. Discussion

In this study, we have demonstrated that DCS can be used to separate identical cellular phenotypes with different physiological properties. In the context of CAR T-cells, this is an important unsolved problem. CAR T-cell purification has to be performed as quickly as possible

and the suspension time in the low-conductivity buffer must be minimized to decrease cell death. We have found that a sample flow rate of 7.5 μL min−1 and an electric field produced at 5 MHz yield the best purification (~100%) and recovery values for all of the cell mixtures we tested. Moreover, we found that cell recovery is difficult to control and may attributed to factors such as human error in counting cells, cell loss during handling, cell loss during the introduction to the microfluidics device and collecting cells back from the microfluidics device. The purity and recovery values could also depend on dimensions of the microfluidics device, especially the channel height. Moreover, to achieve large values for purity and recovery, there should be an inverse proportionality between channel depth and sample flow rate.

There are predictions about the origins of the fundamental physics behind the differential DEP forces of live and nonviable cells [52]. However, we measured the cell diameter of live cells and non-viable cells (after electroporation), and we found that the cell diameter increased from 11 μm to 14 μm after electroporation for non-viable cells. This increase could lead to an increase in the DEP force by about two-fold for non-viable cells compared with live cells. We are carrying out additional experiments to better understand how the physiological states of cells come into play during DEP. In addition, Dr Gerald Marx's group has reported similar results in which different physiological states such as live, dormant and dead bacterial cells produced pDEP at different frequencies [275].

In addition to T-lymphocytes, we have purified cultured live kidney cancer cells (ATCC: HTB-44) from the mixtures of viable and non-viable cells. Non-viable cells were prepared using the electroporation experiments indicated above. Under similar experimental conditions reported here, we have achieved high purity and recovery values (data not shown). The device developed for experiments in our study was simple and had only a single inlet and single outlet; no complex

machinery or expensive equipment was necessary to perform the cell purification. Therefore, this method can be easily implemented in clinics and other centralized biomanufacturing facilities by persons lacking technical training. In addition, the DCS device could easily integrate with electroporation devices for single-step cell transfection and purification. For these reasons, DCS provides a viable solution to address the T-cell purification necessary in CAR T-cell therapy.

CHAPTER 8. DIELECTROPHORETIC HIGH PURITY ISOLATION OF PRIMARY T-CELLS IN SAMPLES CONTAMINATED WITH LEUKEMIA CELLS, FOR BIOMANUFACTURING OF THERAPEUTIC CAR T-CELLS[6]

8.1. Introduction

Recent clinical studies have demonstrated that cancer patient's blood samples can have tumor cells. A small portion of these tumor cells can be in the isolated T-cell sample (either by accident or via nonspecific isolation). These tumor cells are subsequently genetically modified to produce CAR antibody molecules, and these modified cancer cells are mostly immune to CAR T-cells [276],[277]. This is because engineered CAR receptors in the tumor cells conjugate with other cancer cells and block access to CAR T-cells [276]. Moreover, these reprogrammed tumor cells can potentially develop into secondary tumors that are not recognized by CAR T-cells [276]. Ruella et al. and others have reported that a leukemia patient relapsed 9 months after targeted CAR T-cell infusion for leukemia cells that express CD19 antigen molecules [276]. It was discovered that the CAR gene was unintentionally introduced into a single leukemic B cell during T-cell manufacturing, and this cell produced a CAR antibody that masked it from recognition by CAR T-cells. This abnormal leukemia cell, which expressed CAR molecules, proliferated and produced a secondary tumor in the patient [276]. Although CAR T-cell therapy has great potential for the treatment of advanced-stage cancer patients, the current methods for CAR T-cell manufacturing have their limitations. In the absence of rapid and reliable cell purification methods to prevent tumor cell contamination, all the potential benefits may be potentially undermined.

[6] The material presented in this chapter is currently under review after submission to Analytical Chemistry journal and was co-authored by Beth Ringwelski, Vidura Jayasooriya, and Dharmakeerthi Nawarathna. Jayasooriya V. conducted experiments, analyzed results and co-drafted the paper. Reprinted with permission, from Ringwelski, Beth, Jayasooriya, Vidura, Nawarathna, Dharmakeerthi, "Dielectrophoretic High Purity Isolation of Primary T-cells in Samples Contaminated with Leukemia Cells, for Biomanufacturing of Therapeutic CAR T-cells"

Conventional methods like fluorescence-activated cell separation (FACS) and magnetic-activated cell separation (MACS) [142],[278] cannot be used due to the issues mentioned in chapter 7 section 7.1. To address this critical issue, we have utilized dielectrophoretic cell separation that is discussed in chapter 7. At a specific frequency, differential polarizability between the target cells (such as T-cells) and non-target cells (such as leukemia cells) can be used to trap target cells on the microfluidics device and flow non-target cells out of the device [279]. The differential polarizability is also used to trap the non-target cells in the device, and target cells flow into the outlet [55]. Dielectrophoretic cell separation has been used in a large number of cell separation applications. These include isolation of live cells from mixtures of live, dead, and dying cells [279], separation of circulating tumor cells from blood samples [55], and isolation of platelets from diluted whole blood samples [280]. In these studies, the quality of cell separation was determined using purity (the amount of non-target cell contamination in the cell sample), recovery (percentage of target cells in the output), and throughput (the number of target and non-target cells that can be analyzed in the microfluidic device within a specified amount of time).

Generally, dielectrophoretic cell separation experiments that produced high recovery values (greater than 90%) have been reported [281]. As the dielectrophoretic force is dependent on the cell size, the throughput of separation for mammalian cells is generally high [282]. Typically, depending on cell size, the dielectrophoretic cell separation method can separate a large number of cells. For example, Hu et al. reported a throughput of 10,000 cells per second [208]. With regards to purity, Thomas et al. separated green polystyrene beads from red beads with 100% purity [283]. In addition, a study conducted by Yildizhan et al. reported greater than 90% purity when isolating live human myeloid leukemia cells (U937) from a mixture of live and dead U937 cells [284]. This evidence indicates that dielectrophoretic cell separation is a potential candidate

for the purification of T-cell samples contaminated with cancer cells. Most importantly, purified T-cells need to be 100% pure to ensure that no tumor cell is present. Therefore, the experiments in this study were focused on sample purity values after separation.

In this study, to simulate real-world conditions, we spiked whole blood samples with tumor cells, then isolated T-cells using a commercially available T-cell isolation kit, and finally used the isolated T-cell samples as the input to the dielectrophoretic cell separation device. The tumor cells were selectively trapped on the electrodes by producing attractive dielectrophoretic forces on tumor cells, and T-cells were collected at the outlet of the device in real-time. The cell sample collected at the output was analyzed using flow cytometry, real-time quantitative reverse transcriptase polymerase chain reaction (real-time qRT-PCR)), and manual tumor cell counting. Experiments were carried out separately by spiking typical leukemia cells, either chronic myelogenous leukemia (K-562) cells, or acute lymphoblastic leukemia cells (ALL).

8.2. Materials and methods

8.2.1. Fabrication of the microfluidic cell separation device

The microfluidic device used in the experiments consisted of interdigitated electrodes (IDEs) and a microfluidic channel that had a single inlet and single outlet. The dimensions of the single pair of electrodes were 1 cm x 25 μm x 100 nm. The total electrode area on the device was 2 cm x 1 cm and the channel height was 100 μm. The IDEs were fabricated on a glass substrate using standard photolithography, and the flow channel was fabricated in polydimethylsiloxane (PDMS) and bonded together using oxygen plasma. Detailed manufacturing of each component was outlined in a previous study in chapter 7 [279]. Cell samples (composed of T-cells and cancer cells) were introduced into the device via the inlet with a NE-1002X microfluidic syringe pump (New Era Pump Systems, Inc., Farmingdale, NY) and collected in a centrifuge tube at the outlet

for analysis. Electric potential values were applied using a function generator (AFG3021B, Tektronix, Beaverton, OR).

8.2.2. Culturing chronic myelogenous leukemia (K-562) cells

Commercially available chronic myelogenous leukemia (K-562) cell line was purchased (ATCC Manassas, MA) and cultured in RPMI 1640 medium supplemented with 2 mM Glutamine and 10% FBS (by volume). Cells were cultured in an incubator at 37°C with 5% CO_2. Fresh cells were harvested, counted, and then used in experiments.

8.2.3. Culturing acute lymphoblastic leukemia cells (ALL)

ALL (SUP-B15) cells were purchased from American Type Culture Collection (ATCC, Manassas, VA) and cultured in complete medium containing Iscove's modified Dulbecco's medium with 4 mM L-glutamine and 1.5 g/L sodium bicarbonate. In addition, the cell culture medium was supplemented with 0.05 mM 2-mercaptoethanol (Sigma Aldrich, St. Louis, MO). Finally, 20% (by volume) fetal bovine serum (ATCC, Manassas, MA) was added to the cell culture medium. The culture samples were cultured in an incubator at 37°C in 5% CO_2 and sub-cultured 2–3 times a week. Fresh cells were harvested and counted before their use in experiments.

8.2.4. Preparation of cell samples and cell purification experiments

Commercially available pooled blood samples (Innovative Research, Novi, MI) from healthy individuals were used in the experiments. In cell purification experiments, approximately 2.0 x10^6 K-562 or SUP-B15 cancer cells were pipetted directly to the human whole blood sample, totaling 20 mL. The cancer cells were stained with Calcein AM (Thermo Fisher Scientific, Waltham, MA) before addition. Briefly, Calcein was added to the cell sample and allowed to incubate at room temperature for 30 min. Following incubation, the cancer cells were washed 3 times before being added to the blood sample. A verified T-cell isolation protocol (described

below) was applied to the whole blood sample (20 mL) after the addition of the cancer cells. The T-cell isolation yielded approximately 2 mL of sample volume, so 1mL of diluted phosphate-buffered saline (PBS 100x; Sigma Aldrich) solution was added. 3 mL of the sample was equally divided to perform four cell purification experiments (750 µL per experiment). Before adding the PBS, the osmolality of the PBS buffer was adjusted to 180 mOsm/l. The T-cell count per experiment was kept constant (approximately 10^5 cells).

The cell solutions were then separately flowed through the microfluidic chip device at three varying speeds (100, 10, and 1 µL/min) to determine which flow rate yielded the best result. The cancer cells were trapped on the electrode, while T-cells were able to flow over the top and collect at the end of the device. An electric field was produced in the device by applying an electric potential of 3 Vpeak-to-peak (Vpp), and 500 kHz and negative control experiments were performed without electric fields at 1 µL/min. Each sample was stained with Propidium Iodide (PI; Thermo Fisher Scientific, Waltham, MA) and analyzed using flow cytometry. The samples that were used for real-time qRT-PCR were not stained.

8.2.5. T-cell isolation

Cell isolation was performed using a commercially available human T-cell ($CD8^+$) isolation kit (STEMCELL Technologies, Cambridge, MA). For experiments involving cancer cells mixed with blood, approximately 2.0 x 10^6 leukemia cancer cells (K562 cells) were stained with Calcein AM. Calcein AM provided green fluorescence, which aided in the analysis process.

To begin the isolation process, 20 mL of Ficoll-Paque (Ficoll® Paque Plus, GE Healthcare, Chicago, IL) was added to a 50 mL centrifuge tube. The Ficoll-Paque created a cushion for the 10 mL sample of whole human blood to be slowly pipetted on to. The combined blood and Ficoll-Paque solution was centrifuged for 30 min (24°C; 400 x g), and the solution separated into distinct

layers. The bottom layer consisted of red blood cells, the middle layer had peripheral blood mononuclear cells (PBMC) and T-cells, and the top layer had plasma cells. To ensure the complete collection of all the T-cells, the entire top layer (PBMC and Plasma), approximately 6 mL, of the sample was extracted with a pipette and placed in a 15 mL centrifuge tube. The sample was then topped to 15 mL with sterile 1x phosphate-buffered saline solution (PBS). The tube was placed back into the centrifuge and was spun for 5 min (24°C; 300 x g). The supernatant was poured out of the centrifuge tube, and the remaining cells were noted to be red. The remaining red blood cells (RBC) were removed by the addition of 3 mL of RBC lysis buffer to the pellet and vortexed for 3 min. The sample was topped to 15 mL with PBS and put into the centrifuge for 5 min (24°C; 300 x g). The cells were then counted (9.0×10^7 cells in about 2 mL of solution), and this determined how much EasySep buffer (STEMCELL Technologies, Cambridge, MA) could be added later (1 mL per 5.0×10^7 cells). Following the count, the remaining cell solution was brought up to 15 mL with PBS and put back in the centrifuge for a final spin (5 min at 24°C; 300 x g). After removing the supernatant, 1.6 mL of EasySep buffer, which came with the T-cell isolation kit, was added to the cells and mixed. Isolation kit directions were then followed to finish the isolation of the $CD8^+$ T-cells using a cocktail mix, magnetic beads, and magnet device. Once the cells were isolated, the final count was found to be 3.45×10^6 $CD8^+$ T-cells. To quantify cell viability following cell isolation, a hematocytometer and trypan blue were used. The viability of the $CD8^+$ T-cells was found to be around 92%.

8.2.6. RNA isolation

The RNeasy Mini kit (Qiagen, Germantown, MD) was used to isolate the total RNA from the cell samples. Initially, the cell sample was lysed by adding 350 μL RLT buffer (Qiagen) and rigorous vortexing for up to 2–3 min. Then 350 μL of ethanol was added to the lysate to provide

ideal binding conditions. The lysate was then loaded onto the RNeasy mini spin column with a silica membrane and centrifuged for 15 s at 8000 x g, and the flow-through was discarded. Then 700 µL of RW1 buffer (stringent washing buffer, Qiagen) was added to the column and centrifuged for 15 s at 8000 x g. The column was washed twice with RPE buffer (mild washing buffer, Qiagen) for 15 s at 8000 x g in the first wash and an additional 2 min at 8000 x g. Finally, total concentrated RNA was eluted in 30 µL of DI water by adding the DI water to the silica membrane (which changed the pH) and spinning for 1 min at 8000 x g. Upon isolation, the RNA sample was quickly analyzed using real-time qRT-PCR or stored at -20°C for future use.

8.2.7. cDNA synthesis

iScript™ cDNA Synthesis Kit (BioRAD, Hercules, CA) was used to synthesize cDNA from the isolated total RNA. For 3 µL of total RNA, 4 µL of iScript RT Supermix, and 13 µL nuclease-free water was added to PCR tubes. The PCR tubes were placed in the real-time quantitative RT-PCR system (CFX96, BioRAD), and synthesis was performed. cDNA synthesis was performed according to the instructions of the manufacturer provided in the synthesis kit. First, priming of the reaction was performed by holding the sample temperature at 25°C for 5 min, then reverse transcription reaction was performed by keeping the sample temperature at 46°C for 20 min, and then the sample temperature was increased to 95°C and maintained for 1 min.

8.2.8. Real-time qRT-PCR reactions

Upon synthesizing the cDNA, samples were prepared for real-time qRT-PCR with SsoAdvanced Universal SYBR Green Supermix kit (BioRAD). The primers listed below were utilized to quantify the expression of BRC-ABL1 mRNA molecules and were commercially synthesized (Midland Certified Reagents company, Midland, TX).

BRC-ABL1 (forward): 5’ – ACTCCAGACTGTCCACAGCA - 3’

BCR-ABL1 (reverse): 5’ – TTGGGGTCATTTTCACTGG - 3’

The reaction mix was prepared by mixing 10 µL of SsoAdvanced Universal SYBR Green Supermix (2x) (BioRAD) with 250 nM from each primer and 6 µL of nuclease-free water. Then the reaction mixture was thoroughly mixed for homogeneity and pipetted into a 96-well PCR plate. Then, 2 µL of cDNA template was added to each well and thoroughly mixed with a pipette, and the well plate was tightly sealed with micro seal 'B' PCR Plate optical adhesive Sealing Film (BioRAD). The PCR plate was then placed in the PCR machine (CFX96, BioRAD). Forty reaction cycles of the following assay (a–b) were performed.

(a) Denaturation: 95°C for 15 s

(b) Annealing/Extension: 60°C for 30 s

Before temperature cycling, we activated the polymerase and denaturation of DNA primers by heating the sample to 95°C and maintaining the temperature for 30 s. Fluorescence intensity of each well after each cycle was recorded.

8.2.9. DNA denaturation analysis

After the real-time qRT-PCR reaction, the reaction temperature was varied from 65° C to 95°C in 0.5°C increments, and the temperature was maintained for 5 s. The fluorescence intensity of each well at each temperature was recorded.

8.2.10. Data

Two datasets, fluorescence intensity vs. cycle number and rate of fluorescence intensity change vs. temperature, were exported using Excel files by the CFX Manager software.

8.2.11. Flow cytometry

Flow cytometry was performed on a Fluorescence-Activated Cell Sorting (FACS) machine (AccuriC6; BD, Franklin Lakes, NJ). Propidium Iodide (PI; Invitrogen, Carlsbad, CA) was added to the cell samples before FACS to evaluate cell viability. The K-562 and SUP-B15 cells had been

stained previously with Calcein AM (Molecular probes, Eugene, OR) before being isolated from whole blood samples or isolated T-cell samples so that the green fluorescence would be accounted for as well. The compensation on the FACS device was adjusted for both dyes, FL1 was adjusted by 3.2% and FL2 by 7.5%. Bleach and water were run through the device to ensure the cleanliness of the machine before running the samples. Results were analyzed by looking at the FL1 and FL2 products using FlowJo software.

8.2.12. Manual cell counting

Cell samples were pipetted to a clean microscope glass slide, and a manual count of the number of green fluorescent cells was performed. Each count was repeated at least 3 times to ensure accuracy.

8.3. Results and discussion

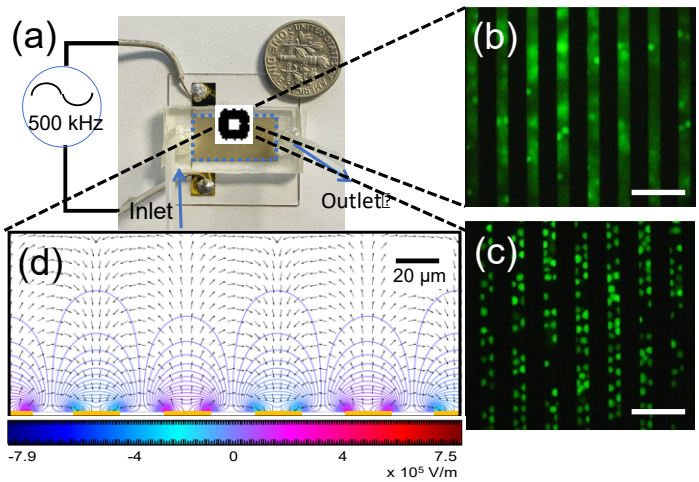

Figure 8.1. Dielectrophoretic T-cell separation device used in the experiments.
(a) A picture of the device with inlet, outlet, interdigitated electrodes (inside the rectangle with broken lines) and connection to the external function generator. (b and c) Fluorescence images of the trapped K-562 cells at 100 and 10 μL/min, respectively. Scale bars indicate 100 μm. (d) Finite Element Modeling (Comsol, Burlington, MA) results of the interdigitated electrodes used to produce DEP force on cells. Contours are the electric fields in the z-direction. Arrows are the electric field vectors in the x-z direction.

In this study, a frequency of 500 kHz was used, and this produced the largest differential polarizability between cancer cells and T-cells, allowing us to trap the cancer cells on the

electrodes. This frequency was experimentally obtained by examining frequency values from 1 kHz to 1 MHz. Yildizan et al. have reported that human myeloid leukemia cells could produce large polarizability and DEP force at frequencies between $10-10^4$ kHz [20]. We used an attractive DEP force to trap the cancer cells on the electrodes. The attractive DEP force concentrates on cancer cells in the regions that have the largest electric field gradient. Figure 1(a) shows a picture of the microfluidic device used in the experiments. Figure 1(b) shows the trapped K-562 cells at 10 μL/min. Note that cells are trapped on the electrodes or electrode edges, which indicate that positive DEP force was produced on the cells. Figure 1(c) shows an image of trapped K-562 cells at 100 μL/min. There are few cells are trapped on the electrodes by positive DEP force and a larger number of cells are flowing over electrodes (out of focus objects) without trapping on the electrodes. Similarly, we found that at 100 and 10 μL/min, the majority of T-cells flowed without trapping by DEP force (data not shown). Figure 1(d) shows the calculated electric fields in the microfluidics channel (x-z plane). Contours show the electric field in z-direction, which is used to pull the cancer cells toward the electrodes that are located at the bottom of the microfluidic channel. Arrow plot illustrates the electric field values in the x-z plane that polarize the cells and produce DEP force.

Since the DEP force is dependent on the cell volume, the expected DEP force that pulled the cells towards the electrode for K-562 cells (approximate diameter = 20 μm) was about 37 times the DEP force of T-cells (approximate diameter = 6μm). Similarly, the DEP force on the ALL cells was about 8 times the DEP force of T-cells. The viscous drag force, which is dependent on the cell radius, carries the cell horizontally towards the outlet of the device. The cells trapped (e.g., K-562) on the electrode experienced both DEP and viscous drag forces. Moreover, stronger DEP force than the viscous grad force is expected on trapped cells. Similarly, T-cells experienced a larger

viscous drag force than the DEP force, so T-cells flow into the outlet without getting trapped on the electrodes. This cell trapping strategy is different from traditional continuous cell purification, where target cells are separated from non-target cells using the combination of DEP and viscous drag force. When electric potentials of 3Vpp at 500 kHz were used to produce DEP forces, sample flow rates in µL/min were required to trap the cancer cells on the electrodes. Experiments were conducted using sample flow rates of 100 µL/min, 10 µL/min, and 1µL/min, and we found that 10 µL/min and 1 µL/min were sufficient for selectively trapping cancer cells (e.g., K-562) on the electrodes.

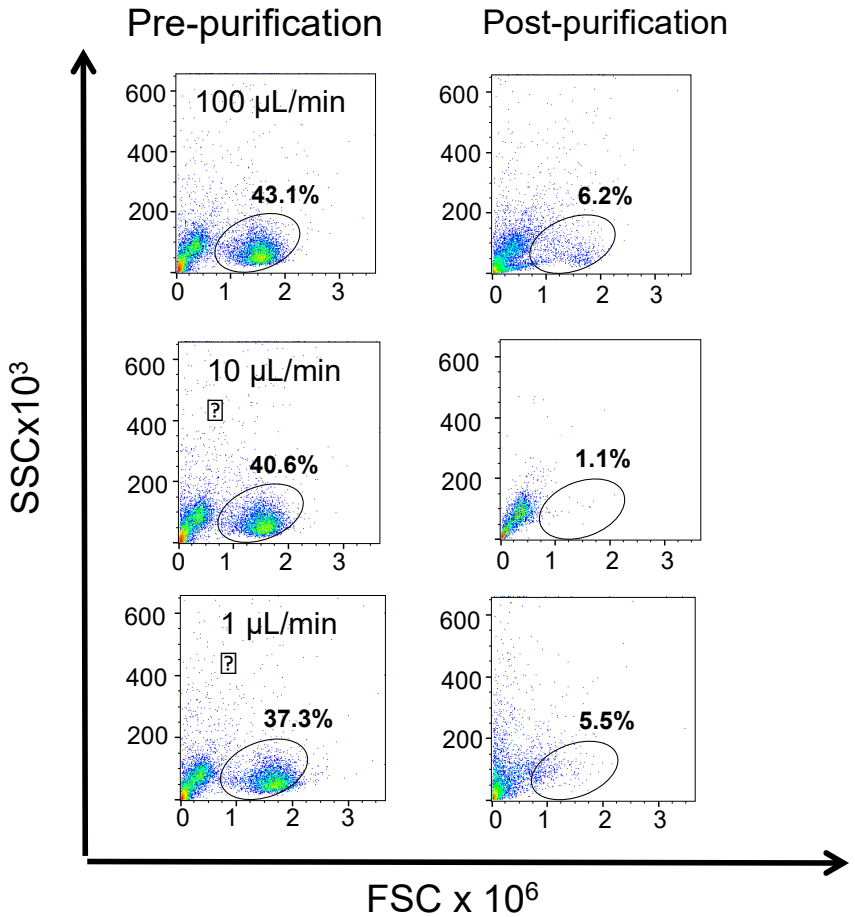

Figure 8.2. Flow cytometry results of the purification of T-cells that have spiked K-562 cells. The first column indicates the cell mixture before purification and the second column shows the cell mixture after purification. Negative control experiments were performed without applying DEP force and flowing cell samples at 10 µL/min (data not shown). The purity of the negative control sample was 88.4%.

To demonstrate the ability of dielectrophoretic cell separation to purify T-cells, a sample of isolated primary T-cells was spiked with the cultured K-562 cells and purified. We performed purification experiments by flowing the cell samples at 100, 10, and 1 μL/min. Additionally, we also performed experiments without DEP force. Figure 2 illustrates a summary of these results. When we applied the electric potential value of 3Vpp at 500 kHz and a sample flow rate of 10 μL/min, the majority of cancer cells (purity = 98.9%) were trapped in the device (row 2 of Figure 2). The viability of the purified T-cells at 10 μL/min was about 91.6%. We have also performed control experiments by flowing samples without applying any electric potential or no DEP force and found that the purity of the sample collected at the output was 88.4% (data not shown). A flow rate of 1 μL/min also produced a high level of purification (94.5%), but the viability of T-cells collected at the outlet was approximately 31.3%. When the sample flow rate was 100 μL/min, the purity and cell viability values were 93.8% and 89.3%, respectively. At 100 μL/min, a high viscous drag force could carry some of the cancer cells into the outlet. These results show that 10 μL/min produces an optimal balance between DEP and viscous drag force. Therefore, we used these experimental conditions in the rest of the cell purification experiments.

In the next set of cell purification experiments, we studied the effectiveness of DEP cell purification in simulated samples, which is more relevant to the clinical issue outlined above. We added about 2 x 10^6 K-562 cells to whole blood samples and isolated the T-cells. We did not stain the samples with Calcein AM for these experiments. We then divided the cell samples equally and prepared 100 μL of cell samples for purification. It was found that there were about 32 K-562 cells and approximately 100,000 T-cells in a 100 μL cell sample. The cell samples were purified by flowing at both 100 and 10 μL/min, and an electric potential value of 3Vpp (frequency of 500 kHz)

was applied to produce the DEP force. The entire 100 µL sample was flown through the microfluidic device, and an additional 400 µL of PBS buffer was added to the collected samples.

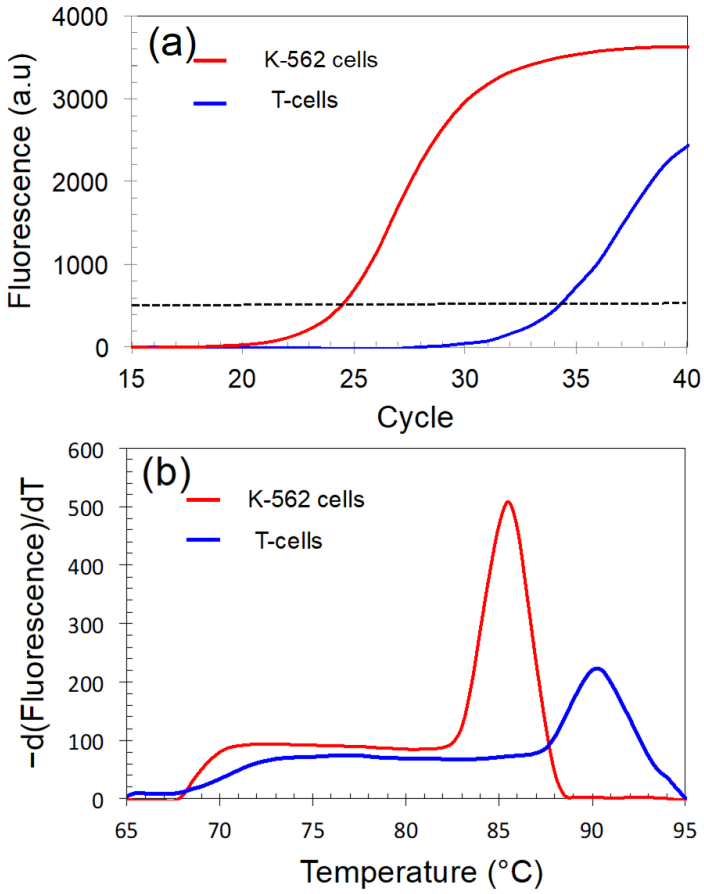

Figure 8.3. The expression analysis of BCR-ABL mRNA in K-562 and T-cells, which was performed using real-time quantitative reverse transcriptase polymerase chain reaction. (a) Fluorescence vs cycle number produced by 10^6 K-652 cell and 10^5 T-cells. (b) Melting of amplified double-stranded DNA from K-562 and T-cells. The initial DNA was produced by reverse transcribing the BCR-ABL mRNA molecules.

Since there are no fluorophore tags that could be used in flow cytometry, accurate detection of a small quantity of cancer cells in a sample with FSC-SSC is difficult. Therefore, we used the real-time qRT-PCR method to analyze the cell samples and quantify the cancer cells. Domingo et al. have shown that PCR could be 1-log sensitive than flow cytometry [285]. A recent report by Guo et al. demonstrated that real-time qRT-PCR could be used to detect rare cells (e.g., circulating tumor cells) in the blood samples [286]. Moreover, the study demonstrated the detection of single

circulating breast cancer cells[286]. We assumed that the expression of mRNA does not vary during the experiments. We designed the real-time qRT-PCR experiments to detect the presence of BCR-ABL mRNA molecules as an indirect method for detecting K-562 cells in samples. Studies have reported that specific leukemia cells containing a fusion of portions of the BCR gene and the ABL gene produce unique chimeric BCR-ABL mRNAs [287]. Guo et al. have shown that the BCR-ABL gene is highly expressed in myelogenous leukemia cells [287]. In addition, Yu et al. showed that real-time qRT-PCR was able to detect the mRNA produced by the BCR-ABL gene [288].

We first studied the expression of BCR-ABL mRNA in K-562 and T-cells. We have performed real-time qRT-PCR experiments of known quantities for K-562 (10^6 cells) and T-cell (10^5 cells) samples and evaluated the expression of BCR-ABL mRNA in each cell type. Briefly, we lysed the cells in each sample, isolated total RNA, and performed real-time quantitative qRT-PCR reactions. Figure 3(a) shows the fluorescence vs. cycle number for 10^6 K-562 and 10^5 T-cells. We calculated critical threshold values (C_t) for each cell sample and compared the values. The C_t is the cycle number in the exponential region at which fluorescence intensity is equal to 500 (a.u) (Figure 3 (a)). The C_t values for K-562 and T-cells were 24 and 34, respectively. We then calculated the expected Ct value for 10^6 cells, which is ~30.7(34 −3.3) for T-cells. By comparison, K-562 has about 100 fold higher expression of BCR-ABL than T-cells. To further understand the expression of the BCR-ABL gene in K-562 and T-cells, we performed the melt curve analysis after the real-time qRT-PCR reaction (Figure 3(b)). The double-stranded molecules synthesized during the real-time qRT-PCR reaction were used in the generation of the melt curve. During the generation of the melt curve, the sample temperature is gradually increased, and the fluorescence intensity is measured at different temperatures [289]. The intercalating dye (SYBR Green)

selectively conjugates to the double-stranded DNA molecules and produces over 1000 times the fluorescence intensity compared with the free molecules [289]. Therefore, double-stranded molecules are significantly brighter. When the double-stranded molecules reach their melting temperature, they dissociate into single-strands, and the fluorescence intensity decreases. The melting curves are useful for identifying the melting temperatures of double-stranded molecules. Surprisingly, the melting temperature of BCR-ABL mRNA from T-cells was 90°C compared to that from K-562 cells, which was 85°C. Guo et al. reported that the ABL gene is expressed in leukocytes, including T-cells [287]. These data suggest that the fluorescence intensity of T-cells could be coming from the BCR or ABL mRNA molecules.

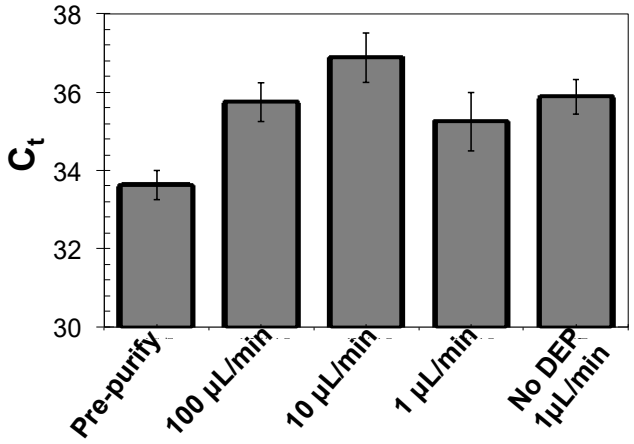

Figure 8.4. Critical threshold (C_t) values calculated using the real-time quantitative reverse transcriptase polymerase chain reaction results.
The Ct value is the cycle number that produces the fluorescence intensity of 500 (a.u) and the lower Ct value indicates the higher starting DNA quantity.

In the next set of experiments, we spiked K-562 cells to whole blood samples, isolated T-cells, performed purification experiments, analyzed each sample with real-time qRT-PCR and calculated Ct values (Figure 4). We have compared the Ct values produced by the initial cell mixture before flowing (Ct=33.63) through the microfluidic device to the output cell samples collected by flowing the samples at 100 µL/min (Ct, approximately 35.75), 10 µL/min (Ct, approximately 36.9) and 1 µL/min (Ct, approximately 35.25). By comparing these Ct values, we

estimated that 100 µL/min and 1 µL/min should have about 4 times less K-562 cells, and 10 µL/min should have about 10 times less K-562 cells than in the initial sample. Since the initial sample had about 32 K-562 cells, purified samples at 100, and 10 µL/min should have about 8 and 3 cells, respectively. We have found that Ct value of the sample purified with DEP force at 1 µL/min, was 35.9. As we described earlier, the majority of cells are killed (viability ~30%) in this sample (1 µL/min). So, higher Ct value may attribute to the low cell numbers in this sample. As we demonstrated earlier, both K-562 (to a higher degree) and T-cells (to a lesser degree) could also contribute to the Ct values. The calculated K-562 cell numbers could be more than the actual K-562 cell numbers present in these samples. Since the real-time qRT-PCR experiments provide approximate cell numbers in purified samples, to find the exact cell numbers, we manually counted the K-562 cells in each sample.

Table 8.1. Chronic myelogenous leukemia (K-562) cell numbers before and after purification using dielectrophoresis.

	Experiment 1	Experiment 2	Experiment3
Pre-purified mixture	32	31	32
3 Vpp (500kHz) and 100 µL/min	14	12	13
3 Vpp (500kHz) and 10 µL/min	0	0	2
3 Vpp (500kHz) and 1 µL/min	0	0	0
No DEP and 1 µL/min	12	13	15

As we stated earlier, for manual cell counting experiments, we have used the K-562 cells were stained with Calcein AM, which emits green fluorescence. Therefore, we were able to identify and count K-562 cells. We carefully counted the cells that emitted green fluorescence. Table 1 shows the results from the manual cell counting. We found that there were about 13 K-562 cells in the samples purified by flowing at 100 µL/min. In contrast, we found no K-562 cells in the samples purified by flowing at 10 µL/min. In comparison, real-time qRT-PCR results detected 8 and 3 cells for 100 and 10 µL/min, respectively. As discussed earlier, real-time qRT-

PCR may not be sensitive enough for detecting such low cell numbers. In addition, there can be contributions to the Ct value from BCR mRNA molecules of the T-cells. Diercks et al. have reported that the detection sensitivity of real-time quantitative RT-PCR in analyzing small amounts of mRNA could be affected by inherent statistical fluctuations in samples [290]. The same study predicted that the improvements to the cell lysis, mRNA extraction, and reverse transcription efficiency could help to improve the accuracy of mRNA detection [290]. For these reasons, we believe that manual cell counting provides a more accurate answer.

Table 8.2. Acute lymphoblastic leukemia (ALL) cell numbers before and after purification using dielectrophoresis.

	Experiment 1	Experiment 2	Experiment3
Pre-purified mixture	37	40	39
3 Vpp (500kHz) and 100 μL/min	18	20	15
3 Vpp (500kHz) and 10 μL/min	0	0	2
3 Vpp (500kHz) and 1 μL/min	0	0	0
No DEP and 1 μL/min	22	19	17

To demonstrate the broad applicability of our cell purification method, we performed cell purification experiments for T-cell samples contaminated with ALL cells. ALL (diameter~11μm) cells are smaller than K-562 cells (diameter ~ 17μm). Therefore, the DEP force of K-562 could be about 3.7 times that of ALL cells. Smaller DEP force was not sufficient to trap ALL cells in the device with a 10 μL/min sample flow rate. Moreover, when we conducted the purification experiments using 3 Vpp (at 500 kHz and 10 μL/min), we found some cancer cells (0-2) in the purified sample (Table 2). In the next experiment, we increased the electric potential value to 5 Vpp and kept all other experimental parameters unchanged from previous experiments. Moreover, we found that theoretically, DEP force with 5 Vpp was about 3 times greater than the DEP force produced by 3 Vpp. Table 3 shows the purification results, and 100% purity value for the cell sample flown at 10 μL/min, were obtained.

8.4. Conclusions

In this work, we showed that dielectrophoretic cell separation could be used to purify T-cell samples contaminated with cancer cells. We demonstrated the proof of concept using samples contaminated with leukemia cells (e.g., K-562 and ALL cells). We selected leukemia cells because CAR T-cell therapy is currently approved for ALL cells. The purification technology is based on differences in cell size between T-cells and cancer cells, and therefore, it can be applied to any cancer cell type that is bigger than T-cells. In comparison with other competing technologies, dielectrophoretic cell purification may potentially be a better fit for point-of-care settings with limited access to technology. One of the great advantages of this method is the absence of cell labeling. The performance of cell purification experiments is relatively simple, as one only needs to apply an electric potential and set up the sample flow through the device. Therefore, any non-technical experimenter can perform cell purification experiments. The manufacturing cost of the cell purification device will potentially be less than $100. This is because the device has a microelectrode array that is easy to manufacture. In addition, a microfluidic channel is manufactured from low-cost PDMS polymeric materials that are FDA-approved. A function generator and a microfluidic pump are also required to apply the electric potentials and flow the samples over the electrodes, respectively. The combined cost of the equipment will be about $3000. With this method, cell viability values greater than 90% were achieved after purification. If higher cell viability is required, an increase of the sample flow rate, a slight decrease in the electric potentials, or covering of the device externally with ice to maintain the proper temperature could further improve the cell viability. Additionally, there exist different cell-separation methods that are capable of removing the dead or dying cells present in the samples [279].

CHAPTER 9. OVERALL CONCLUSION

In this research, MEA, microfluidic, and DEP technologies were utilized to develop studies to quantitatively measure DEP, to investigate iDEP technologies. Further, those technologies were used to develop two potential biosensor techniques and to develop a technique for biomanufacturing cells for therapy.

Chapter two discussed the method of using an Atomic Force Microscope (AFM) to take quantitative measurements of FDEP in conventional parallel interdigitated electrode array devices. The spatial distribution of DEP, its strong dependence on the nanoscale structure of the electrode and the nanoscale separation distance from the electrode edge were observed in the study. These precise measurements of DEP are useful for quantitative comparisons, among the competing forces, such as viscous drag force, Brownian force, and hydrodynamic forces, to determine the dominant forces, which are governing the movements of biomolecules. Usage of these techniques in biomedical engineering demands precise knowledge of DEP, to design micro/nano electronic devices, and tune the operating parameters associated with other interfering forces, for the effective manipulation of the target.

In chapter three, the development of iDEP-based molecular tweezers, by linking an insulator glass needle and conventional dielectrophoretic method was discussed. These developed iDEP tweezers were successfully utilized to trap, carry, reposition, and release the submicron particles and DNA. Utilization of these iDEP techniques allows simple and effective biomolecule manipulation in a fluid environment, without the potential issues associated with traditional DEP methods, such as fouling, electrolysis, and joule heating.

In the study reported in chapter four, a parallel interdigitated microelectrode array was utilized to quantify protein molecules. Surface modification methodologies were used to

concentrate molecules in between electrodes for detection. Impedimetric measurements were taken for different concentrations of protein molecules. The results show an improved detection limit compared to traditional methods. Furthermore, in this report, it has been discussed how the electrode dimensions and the number of electrode pairs determine the sensitivity of such interdigitated electrode arrays, using a theoretical model. However, it was understood that the surface modification is not an effective way of quantifying other molecules, as it's a complex, time-consuming process, which might involve toxic materials. Thus, in the next chapter, it has been discussed how the DEP principles were utilized to effectively concentrate different types of biomolecules, with the innate ability of dielectrophoresis, to distinguish molecules with its dielectric signature.

In chapter five, a potential, universal, disposable, biosensing technology has been demonstrated, which has proven a detection limit of clinically relevant biomarker levels (< 1 pM) in diluted serum samples. The utilization of dielectrophoresis has improved the capabilities to address the downsides of the biosensor, mentioned in chapter one. The study has proven usage with miRNA and antigen-antibody complexes and has the potential to detect short DNA molecules. The devices mentioned in the report have a fabrication cost of $15, and thus can be used at the point of care settings easily, as a disposable sensor. The device has reported quick response time for detection. The conjugation step mentioned in the report was observed to be a key factor, that determines the specificity performed outside the device. As a suggestion to improve the sensitivity and the specificity, usage of commercially available antigen, miRNA, or DNA isolation kits for isolating the biomarkers of interest, is encouraged.

Chapter six, envisages a potential, non-viral, personalized, and low-cost device, which was developed to safely manufacture cells for CAR T-cell therapy. Here, CAR mRNA electroporation

was selected as the method to engineer CAR T-cell, due to the transient nature of the CAR mRNA. It was noted as an effective way to address the issues associated with viral vectors, like permanent gene modifications and CRS. DEP was utilized to pattern cells before electroporation, enabling cells to be exposed to a uniform and controllable electroporation. With the introduction of the new method, salient improvements were observed in terms of transfection efficiency, controllable transfection, improved CAR-expressing time, faster target cell lysing, and higher viability, upon electroporation, over the conventional methods.

Chapter seven described an approach we have investigated, to utilize dielectrophoretic cell sorting (DCS) methods to separate dead cells from live cells with identical cellular phenotypes. In our approach to develop an effective manufacturing method in cellular therapy, this remains an important unsolved problem. Also, it was noted that CAR T-cell purification has to be performed as quickly as possible and the suspension time in the low-conductivity buffer must be minimized to decrease cell death. Here, the increase of the cell size upon necrosis was observed as a potential reason, which could lead to an increment in the DEP force, by about two-fold, for non-viable cells, compared with live cells. The developed device consists of relatively simple steps to use and can be easily implemented in clinics as well as other centralized biomanufacturing facilities. Furthermore, this device can be easily integrated with electroporation devices for integrated cell transfection and purification Lab on a chip device, in mRNA based cellular engineering applications.

Chapter eight described a label free cell separation methodology that could be used to purify T-cell samples contaminated with cancer cells. The purification technology is based on differences in cell size between T-cells and cancer cells, and therefore, it can be applied to any

cancer cell type that is bigger than T-cells. With this method, cells were purified with a purity value of 100% and a cell viability greater than 90% was achieved after purification.

In conclusion, the report envisages research methodologies with proven results, which successfully utilize MEA, micro-fluidic, and DEP technologies, to bridge a few major gaps that exist in clinical settings and LOC technologies.

REFERENCES

(1) Maheshwari, N.; Chatterjee, G.; Ramgopal Rao, V. *A Technology Overview and Applications of Bio-MEMS*; 2014; Vol. 3.

(2) Frazier, A. B.; Warrington, R. O.; Friedrich, C. The Miniaturization Technologies: Past, Present, and Future. *IEEE Trans. Ind. Electron.* **1995**, *42* (5), 423–430. https://doi.org/10.1109/41.464603.

(3) Keyes, R. W. MINIATURIZATION OF ELECTRONICS AND ITS LIMITS. *IBM J. Res. Dev.* **1988**, *32* (1), 24–28. https://doi.org/10.1147/rd.321.0024.

(4) Wise, K. D.; Najafi, K. Microfabrication Techniques for Integrated Sensors and Microsystems. *Science (80-.).* **1991**, *254* (5036), 1335–1342. https://doi.org/10.1126/science.1962192.

(5) Sonetha, V.; Agarwal, • Poorvi; Doshi, S.; Kumar, R.; Mehta, B. Microelectromechanical Systems in Medicine. https://doi.org/10.1007/s40846-017-0265-x.

(6) Cheung, K. C.; Renaud, P. BioMEMS for Medicine: On-Chip Cell Characterization and Implantable Microelectrodes. https://doi.org/10.1016/j.sse.2006.03.023.

(7) Menon, K.; Reenu, &; Joy, A.; Sood, N.; Mittal, R. K. The Applications of BioMEMS in Diagnosis, Cell Biology, and Therapy: A Review. https://doi.org/10.1007/s12668-013-0112-7.

(8) Zhang, Z.; Nagrath, S. Microfluidics and Cancer: Are We There Yet? *Biomed. Microdevices* **2013**, *15* (4), 595–609. https://doi.org/10.1007/s10544-012-9734-8.

(9) Wang, W.; Soper, S. A. *Bio-MEMS: Technologies and Applications*; 2007.

(10) Dielectrophoresis in Microfluidics Technology. https://doi.org/10.1002/elps.201100167.

(11) Zhang, C.; Khoshmanesh, K.; Mitchell, A.; Kalantar-Zadeh, K. Dielectrophoresis for Manipulation of Micro/Nano Particles in Microfluidic Systems. *Analytical and Bioanalytical Chemistry*. 2010. https://doi.org/10.1007/s00216-009-2922-6.

(12) Martinez-Vega, J. *Dielectric Materials for Electrical Engineering*; [Martinez-Vega, J., Ed.]; John Wiley & Sons, Inc.: Hoboken, NJ USA, 2013. https://doi.org/10.1002/9781118557419.

(13) Sihvola, A. Dielectric Polarization and Particle Shape Effects. *J. Nanomater.* **2007**, *45090*. https://doi.org/10.1155/2007/45090.

(14) Hippel, A. R. von; Morgan, S. O. Dielectric Materials and Applications. *J. Electrochem. Soc.* **1955**, *102* (3), 68C-68C. https://doi.org/10.1149/1.2430014.

(15) Pethig, R. Publisher's Note: "Review Article—Dielectrophoresis: Status of the Theory, Technology, and Applications" [Biomicrofluidics 4, 022811 (2010)]. *Biomicrofluidics* **2010**. https://doi.org/10.1063/1.3474458.

(16) Gupta, T. Dielectric Materials. In *Copper Interconnect Technology*; 2009. https://doi.org/10.1007/978-1-4419-0076-0_2.

(17) Sihvola, A. Dielectric Polarization and Particle Shape Effects. *Journal of Nanomaterials*. 2007. https://doi.org/10.1155/2007/45090.

(18) Pethig, R. R.; Goethe, J. W. V; Pethig, R. R. *Dielectrophoresis*; 2017. https://doi.org/10.1007/978-1-4614-5491-5_319.

(19) Belkin, A.; Bezryadin, A.; Hendren, L.; Hubler, A. Recovery of Alumina Nanocapacitors after High Voltage Breakdown. *Sci. Rep.* **2017**, *7* (1), 1–8. https://doi.org/10.1038/s41598-017-01007-9.

(20) Pohl, H. A.; Ackland, H. T. Factors Affecting Separations of Suspensions in Nonuniform Electric Fields. *Fields J. Appl. Phys.* **1958**, *29*, 69. https://doi.org/10.1063/1.1723398.

(21) Pohl, H. A. The Motion and Precipitation of Suspensoids in Divergent Electric Fields. *J. Appl. Phys.* **1951**, *22* (7), 869–871. https://doi.org/10.1063/1.1700065.
(22) Mottelay, P. Bibliographical History of Electricity and Magnetism. **2008**.
(23) Pethig, R. Review Article—Dielectrophoresis: Status of the Theory, Technology, and Applications. *Biomicrofluidics* **2010**, *4* (2). https://doi.org/10.1063/1.3456626.
(24) Çetin, B.; Li, D. Dielectrophoresis in Microfluidics Technology. *Electrophoresis*. 2011. https://doi.org/10.1002/elps.201100167.
(25) Voldman, J. Electrical Forces for Microscale Cell Manipulation. *Annu. Rev. Biomed. Eng.* **2006**, *8* (1), 425.
(26) Zheng, L.; Brody, J. P.; Burke, P. J. Electronic Manipulation of DNA, Proteins, and Nanoparticles for Potential Circuit Assembly. In *Biosensors and Bioelectronics*; 2004. https://doi.org/10.1016/j.bios.2004.03.029.
(27) Pethig, R. Review—Where Is Dielectrophoresis (DEP) Going? *J. Electrochem. Soc.* **2017**, *164* (5), B3049–B3055. https://doi.org/10.1149/2.0071705jes.
(28) Hughes, M. P. Fifty Years of Dielectrophoretic Cell Separation Technology. *Biomicrofluidics* **2016**, *10* (3). https://doi.org/10.1063/1.4954841.
(29) DeBruin, K. A.; Krassowska, W. Modeling Electroporation in a Single Cell. I. Effects of Field Strength and Rest Potential. *Biophys. J.* **1999**, *77* (3), 1213–1224. https://doi.org/10.1016/S0006-3495(99)76973-0.
(30) Ry, L. J. I.; Tsong, T. Y. *Electroporation of Cell Membranes ,~~~~~~~I Lt L3 IstR*; Vol. 60. https://doi.org/10.1016/S0006-3495(91)82054-9.
(31) Lu, H.; A. Schmidt, M.; F. Jensen, K. A Microfluidic Electroporation Device for Cell Lysis. *Lab Chip* **2005**, *5* (1), 23–29. https://doi.org/10.1039/B406205A.
(32) Zhan, Y.; Wang, J.; Bao, N.; Lu, C. Electroporation of Cells in Microfluidic Droplets. *Anal. Chem.* **2009**, *81* (5), 2027–2031. https://doi.org/10.1021/ac9001172.
(33) Nawarathna, D.; Unal, K.; Wickramasinghe, H. K. Localized Electroporation and Molecular Delivery into Single Living Cells by Atomic Force Microscopy. *Appl. Phys. Lett.* **2008**, *93* (15), 153111. https://doi.org/10.1063/1.2981568.
(34) Westerhoff, W.; Westerhoff, H. V. Mechanisms for the Interaction between Nonstationary Electric Fields and Biological Systems i. Linear Dielectric Theory and Its Limitations. *Ferroelectrics* **1988**, *86* (1), 59–78. https://doi.org/10.1080/00150198808227004.
(35) Pohl, H. A.; Crane, J. S. Dielectrophoresis of Cells. *Biophys. J.* **1971**. https://doi.org/10.1016/S0006-3495(71)86249-5.
(36) Pethig, R.; Markx, G. H. Applications of Dielectrophoresis in Biotechnology. *Trends Biotechnol.* **1997**, *15* (10), 426–432. https://doi.org/10.1016/S0167-7799(97)01096-2.
(37) Pethig, R. Dielectrophoresis: Status of the Theory, Technology, and Applications. *Biomicrofluidics* **2010**, *4* (2). https://doi.org/10.1063/1.3456626.
(38) Pohl, H. A. *Dielectrophoresis: The Behavior of Neutral Matter in Nonuniform Electric Fields (Cambridge Monographs on Physics)*; Cambridge University Press: Cambridge, 1978.
(39) Lee, D.; Hwang, B.; Kim, B. The Potential of a Dielectrophoresis Activated Cell Sorter (DACS) as a next Generation Cell Sorter. *Micro Nano Syst. Lett.* **2016**. https://doi.org/10.1186/s40486-016-0028-4.
(40) Qian, C.; Huang, H.; Chen, L.; Li, X.; Ge, Z.; Chen, T.; Yang, Z.; Sun, L. Dielectrophoresis for Bioparticle Manipulation. *International Journal of Molecular Sciences*. 2014. https://doi.org/10.3390/ijms151018281.

(41) Urdaneta, M.; Smela, E. Multiple Frequency Dielectrophoresis. *Electrophoresis* **2007**. https://doi.org/10.1002/elps.200600786.
(42) Ino, K.; Ito, A.; Honda, H. Cell Patterning Using Magnetite Nanoparticles and Magnetic Force. *Biotechnol. Bioeng.* **2007**, *97* (5), 1309–1317. https://doi.org/10.1002/bit.21322.
(43) Voldman, J. ELECTRICAL FORCES FOR MICROSCALE CELL MANIPULATION. *Annu. Rev. Biomed. Eng.* **2006**, *8* (1), 425–454. https://doi.org/10.1146/annurev.bioeng.8.061505.095739.
(44) Takao, M.; Takeda, K. Enumeration, Characterization, and Collection of Intact Circulating Tumor Cells by Cross Contamination-Free Flow Cytometry. **2011**, No. 2, 107–117. https://doi.org/10.1002/cyto.a.21014.
(45) Faradji, A.; Bohbot, A.; Schmitt-Goguel, M.; Siffert, J. C.; Dumont, S.; Wiesel, M. L.; Piemont, Y.; Eischen, A.; Bergerat, J. P.; Bartholeyns, J.; et al. Large Scale Isolation of Human Blood Monocytes by Continuous Flow Centrifugation Leukapheresis and Counterflow Centrifugation Elutriation for Adoptive Cellular Immunotherapy in Cancer Patients. *J. Immunol. Methods* **1994**, *174* (1–2), 297–309. https://doi.org/10.1016/0022-1759(94)90033-7.
(46) Millner, L. M.; Linder, M. W.; Valdes, R. Circulating Tumor Cells: A Review of Present Methods and the Need to Identify Heterogeneous Phenotypes. *Ann. Clin. Lab. Sci.* **2013**, *43* (3), 295–304.
(47) Gascoyne, P. R. C.; Wang, X. B.; Huang, Y.; Becker, R. F. Dielectrophoretic Separation of Cancer Cells from Blood. *IEEE Trans. Ind. Appl.* **1997**, *33* (3), 670–678. https://doi.org/10.1109/28.585856.
(48) Koller, M. R.; Hanania, E. G.; Stevens, J.; Eisfeld, T. M.; Sasaki, G. C.; Fieck, A.; Palsson, B. Ø. High-Throughput Laser-Mediated in Situ Cell Purification with High Purity and Yield. *Cytom. Part A* **2004**, *61A* (2), 153–161. https://doi.org/10.1002/cyto.a.20079.
(49) Park, S.; Koklu, M.; Beskok, A. Particle Trapping in High-Conductivity Media with Electrothermally Enhanced Negative Dielectrophoresis. *Anal. Chem.* **2009**, *81* (6), 2303–2310. https://doi.org/10.1021/ac802471g.
(50) Doh, I.; Cho, Y.-H. A Continuous Cell Separation Chip Using Hydrodynamic Dielectrophoresis (DEP) Process. *Sensors Actuators A Phys.* **2005**, *121* (1), 59–65. https://doi.org/10.1016/j.sna.2005.01.030.
(51) Varshney, M.; Li, Y.; Srinivasan, B.; Tung, S. A Label-Free, Microfluidics and Interdigitated Array Microelectrode-Based Impedance Biosensor in Combination with Nanoparticles Immunoseparation for Detection of Escherichia Coli O157:H7 in Food Samples. *Sensors Actuators, B Chem.* **2007**. https://doi.org/10.1016/j.snb.2007.03.045.
(52) Patel, S.; Showers, D.; Vedantam, P.; Tzeng, T. R.; Qian, S.; Xuan, X. Microfluidic Separation of Live and Dead Yeast Cells Using Reservoir-Based Dielectrophoresis. *Biomicrofluidics* **2012**, *6* (3). https://doi.org/10.1063/1.4732800.
(53) Puttaswamy, S. V.; Sivashankar, S.; Chen, R.-J.; Chin, C.-K.; Chang, H.-Y.; Liu, C. H. Enhanced Cell Viability and Cell Adhesion Using Low Conductivity Medium for Negative Dielectrophoretic Cell Patterning. *Biotechnol. J.* **2010**, *5* (10), 1005–1015. https://doi.org/10.1002/biot.201000194.
(54) Demircan, Y.; Özgür, E.; Külah, H. Dielectrophoresis: Applications and Future Outlook in Point of Care. *Electrophoresis* **2013**, *34* (7), 1008–1027. https://doi.org/10.1002/elps.201200446.

(55) Gupta, V.; Jafferji, I.; Garza, M.; Melnikova, V. O.; Hasegawa, D. K.; Pethig, R.; Davis, D. W. ApoStream^{TM}, a New Dielectrophoretic Device for Antibody Independent Isolation and Recovery of Viable Cancer Cells from Blood. *Biomicrofluidics* **2012**, *6* (2). https://doi.org/10.1063/1.4731647.
(56) Chikkaveeraiah, B. V; Bhirde, A. A.; Morgan, N. Y.; Eden, H. S.; Chen, X. Electrochemical Immunosensors for Detection of Cancer Protein Biomarkers. **2012**. https://doi.org/10.1021/nn3023969.
(57) Velmanickam, L.; Bains, M.; Fondakowski, M.; Dorsam, G. P.; Nawarathna, D. ILluminate-MiRNA: Paradigm for High-Throughput, Low-Cost, and Sensitive MiRNA Detection in Serum Samples at Point-of-Care. *J. Phys. D. Appl. Phys.* **2019**, *52* (5), 055401. https://doi.org/10.1088/1361-6463/AAED97.
(58) Sasanpour, M.; Azadbakht, A.; Mollaei, P.; Reihani, S. N. S. Proper Measurement of Pure Dielectrophoresis Force Acting on a RBC Using Optical Tweezers. *Biomed. Opt. Express* **2019**, *10* (11), 5639. https://doi.org/10.1364/boe.10.005639.
(59) Hong, S.; Kim, C.; Song, H.; An, S.; Yoon, H.; Jhe, W. Measuring Dielectrophoresis Force for Metallic and Non-Metallic Particle Manipulations via a Quartz Tuning Fork Atomic Force Microscope. *J. Korean Phys. Soc.* **2019**, *75* (12), 1021–1027. https://doi.org/10.3938/jkps.75.1021.
(60) Castellanos, A.; Ramos, A.; González, A.; Green, N. G.; Morgan, H. *Electrohydrodynamics and Dielectrophoresis in Microsystems: Scaling Laws*; 2003; Vol. 36.
(61) Martin, Y.; Wickramasinghe, H. K. Magnetic Imaging by "Force Microscopy" with 1000 Å Resolution. *Appl. Phys. Lett.* **1987**, *50* (20), 1455–1457. https://doi.org/10.1063/1.97800.
(62) Nonnenmacher, M.; O'Boyle, M. P.; Wickramasinghe, H. K. Kelvin Probe Force Microscopy. *Appl. Phys. Lett.* **1991**, *58* (25), 2921–2923. https://doi.org/10.1063/1.105227.
(63) Jones, P. V; Salmon, G. L.; Ros, A. Continuous Separation of DNA Molecules by Size Using Insulator-Based Dielectrophoresis. *Anal. Chem.* **2017**, *89* (3), 1531–1539. https://doi.org/10.1021/acs.analchem.6b03369.
(64) Bhattacharya, S.; Chao, T. C.; Ros, A. Insulator-Based Dielectrophoretic Single Particle and Single Cancer Cell Trapping. *Electrophoresis* **2011**, *32* (18), 2550.
(65) Chaurey, V.; Rohani, A.; Su, Y.-H. H.; Liao, K.-T. T.; Chou, C.-F. F.; Swami, N. S. Scaling down Constriction-Based (Electrodeless) Dielectrophoresis Devices for Trapping Nanoscale Bioparticles in Physiological Media of High-Conductivity. **2013**, *34* (7), 1097–1104. https://doi.org/10.1002/elps.201200456.
(66) Masuda, S.; Washizu, M.; Nanba, T. Novel Method of Cell Fusion in Field Constriction Area in Fluid Integration Circuit. *IEEE Trans. Ind. Appl.* **1989**, *25* (4), 732–737. https://doi.org/10.1109/28.31255.
(67) Chou, C. F.; Zenhausern, F. Electrodeless Dielectrophoresis for Micro Total Analysis Systems. *IEEE Eng. Med. Biol. Mag.* **2003**. https://doi.org/10.1109/MEMB.2003.1266048.
(68) Regtmeier, J.; Eichhorn, R.; Viefhues, M.; Bogunovic, L.; Anselmetti, D. Electrodeless Dielectrophoresis for Bioanalysis: Theory, Devices and Applications. *Electrophoresis* **2011**, *32* (17), 2253–2273. https://doi.org/10.1002/elps.201100055.

(69) Strimbu, K.; Tavel, J. A. What Are Biomarkers? *Current Opinion in HIV and AIDS*. 2010. https://doi.org/10.1097/COH.0b013e32833ed177.
(70) Daniels, J. S.; Pourmand, N. Label-Free Impedance Biosensors: Opportunities and Challenges. *Electroanalysis*. June 2007, pp 1239–1257. https://doi.org/10.1002/elan.200603855.
(71) Thévenot, D. R.; Toth, K.; Durst, R. A.; Wilson, G. S. ELECTROCHEMICAL BIOSENSORS: RECOMMENDED DEFINITIONS AND CLASSIFICATION *. *Anal. Lett.* **2001**, *34* (5), 121–131. https://doi.org/10.1081/AL-100103209.
(72) Drummond, T. G.; Hill, M. G.; Barton, J. K. Electrochemical DNA Sensors. *Nature Biotechnology*. October 1, 2003, pp 1192–1199. https://doi.org/10.1038/nbt873.
(73) Katz, E.; Willner, I.; Wang, J. Electroanalytical and Bioelectroanalytical Systems Based on Metal and Semiconductor Nanoparticles. *Electroanalysis* **2004**, *16* (12), 19–44. https://doi.org/10.1002/elan.200302930.
(74) Thompson, I. M.; Pauler, D. K.; Goodman, P. J.; Tangen, C. M.; Lucia, M. S.; Parnes, H. L.; Minasian, L. M.; Ford, L. G.; Lippman, S. M.; Crawford, E. D.; et al. Prevalence of Prostate Cancer among Men with a Prostate-Specific Antigen Level ≤4.0 Ng per Milliliter. *N. Engl. J. Med.* **2004**, *350* (22), 2239–2246. https://doi.org/10.1056/NEJMoa031918.
(75) Qureshi, A.; Gurbuz, Y.; Niazi, J. H. Biosensors for Cardiac Biomarkers Detection: A Review. *Sensors and Actuators, B: Chemical*. August 2012, pp 62–76. https://doi.org/10.1016/j.snb.2012.05.077.
(76) Balasubramanian, K.; Burghard, M. Biosensors Based on Carbon Nanotubes. *Analytical and Bioanalytical Chemistry*. June 2006, pp 452–468. https://doi.org/10.1007/s00216-006-0314-8.
(77) R. A. Goldsby, T. J. Kindt, B. A. O. *Immunology*, 5th Edition.; W. H. Freeman: New York, 2003.
(78) Chikkaveeraiah, B. V; Bhirde, A. A.; Morgan, N. Y.; Eden, H. S.; Chen, X. Electrochemical Immunosensors for Detection of Cancer Protein Biomarkers. **2012**. https://doi.org/10.1021/nn3023969.
(79) Cissell, K. A.; Deo, S. K. Trends in MicroRNA Detection. *Anal. Bioanal. Chem.* **2009**, *394* (4), 1109–1116. https://doi.org/10.1007/s00216-009-2744-6.
(80) Jiang, J.; Lee, E. J.; Gusev, Y.; Schmittgen, T. D. Real-Time Expression Profiling of MicroRNA Precursors in Human Cancer Cell Lines. *Nucleic Acids Res.* **2005**. https://doi.org/10.1093/nar/gki863.
(81) Wu, R.; Wood, M.; Thrush, A.; Walton, E. F.; Varkonyi-Gasic, E. Real-Time PCR Quantification of Plant MiRNAs Using Universal ProbeLibrary Technology. *Biochemica* **2007**.
(82) Wen, Y.; Pei, H.; Shen, Y.; Xi, J.; Lin, M.; Lu, N.; Shen, X.; Li, J.; Fan, C. DNA Nanostructure-Based Interfacial Engineering for PCR-Free Ultrasensitive Electrochemical Analysis of MicroRNA. *Sci. Rep.* **2012**. https://doi.org/10.1038/srep00867.
(83) Chen, Y.; Gelfond, J. A. L.; McManus, L. M.; Shireman, P. K. Reproducibility of Quantitative RT-PCR Array in MiRNA Expression Profiling and Comparison with Microarray Analysis. *BMC Genomics* **2009**. https://doi.org/10.1186/1471-2164-10-407.
(84) Roy, S.; Soh, J. H.; Gao, Z. A Microfluidic-Assisted Microarray for Ultrasensitive Detection of MiRNA under an Optical Microscope. *Lab Chip* **2011**. https://doi.org/10.1039/c0lc00638f.

(85) Varshney, M.; Li, Y. Interdigitated Array Microelectrode Based Impedance Biosensor Coupled with Magnetic Nanoparticle-Antibody Conjugates for Detection of Escherichia Coli O157:H7 in Food Samples. *Biosens. Bioelectron.* **2007**, *22* (11), 2408–2414. https://doi.org/10.1016/j.bios.2006.08.030.
(86) Rana, S.; Page, R. H.; McNeil, C. J. Comparison of Planar and 3-D Interdigitated Electrodes as Electrochemical Impedance Biosensors. *Electroanalysis* **2011**, *23* (10), 2485–2490. https://doi.org/10.1002/elan.201100353.
(87) Taylor, R. F.; Marenchic, I. G.; Spencer, R. H. Antibody- and Receptor-Based Biosensors for Detection and Process Control. *Anal. Chim. Acta* **1991**, *249* (1), 67–70. https://doi.org/10.1016/0003-2670(91)87009-V.
(88) Siegel, R. L.; Miller, K. D.; Jemal, A. Cancer Statistics, 2020. *CA. Cancer J. Clin.* **2020**, *70* (1), 7–30. https://doi.org/10.3322/caac.21590.
(89) Weir, H. K.; Thompson, T. D.; Soman, A.; Møller, B.; Leadbetter, S. The Past, Present, and Future of Cancer Incidence in the United States: 1975 through 2020. *Cancer* **2015**. https://doi.org/10.1002/cncr.29258.
(90) Siegel, R. L.; Miller, K. D. Cancer Statistics , 2019. **2019**, *69* (1), 7–34. https://doi.org/10.3322/caac.21551.
(91) Hunter, P. The Fourth Pillar. *EMBO Rep.* **2017**, *18* (11), 1889–1892. https://doi.org/10.15252/embr.201745172.
(92) Kaufman, H. L.; Atkins, M. B.; Subedi, P.; Wu, J.; Chambers, J.; Joseph Mattingly, T.; Campbell, J. D.; Allen, J.; Ferris, A. E.; Schilsky, R. L.; et al. The Promise of Immuno-Oncology: Implications for Defining the Value of Cancer Treatment. *J. Immunother. Cancer* **2019**, *7* (1). https://doi.org/10.1186/s40425-019-0594-0.
(93) Fischbach, M. A.; Bluestone, J. A.; Lim, W. A. Cell-Based Therapeutics: The next Pillar of Medicine. *Science Translational Medicine*. April 3, 2013. https://doi.org/10.1126/scitranslmed.3005568.
(94) Takeuchi, E. E.; Mrcp, C.; Alison, D. L. What's New in Oncology: Targeted Therapy. https://doi.org/10.1093/bjaceaccp/mkm053.
(95) Trastuzumab and Imatinib Mesylate in Treating Patients With Recurrent or Metastatic HER2/Neu-Expressing Cancer - Full Text View - ClinicalTrials.gov https://www.clinicaltrials.gov/ct2/show/NCT00084513 (accessed Jun 21, 2020).
(96) Fischer, O. M.; Streit, S.; Hart, S.; Ullrich, A. Beyond Herceptin and Gleevec. *Current Opinion in Chemical Biology*. Elsevier Ltd 2003, pp 490–495. https://doi.org/10.1016/S1367-5931(03)00082-6.
(97) Esfahani, K.; Roudaia, L.; Buhlaiga, N.; Del Rincon, S. V.; Papneja, N.; Miller, W. H. A Review of Cancer Immunotherapy: From the Past, to the Present, to the Future. *Curr. Oncol.* **2020**, *27* (S2), 87–97. https://doi.org/10.3747/co.27.5223.
(98) Lee, S.; Margolin, K. Cytokines in Cancer Immunotherapy. *Cancers*. Cancers (Basel) December 2011, pp 3856–3893. https://doi.org/10.3390/cancers3043856.
(99) O'Donnell, J. S.; Teng, M. W. L.; Smyth, M. J. Cancer Immunoediting and Resistance to T Cell-Based Immunotherapy. *Nature Reviews Clinical Oncology*. Nature Publishing Group March 1, 2019, pp 151–167. https://doi.org/10.1038/s41571-018-0142-8.
(100) Sommermeyer, D.; Hudecek, M.; Kosasih, P. L.; Gogishvili, T.; Maloney, D. G.; Turtle, C. J.; Riddell, S. R. Chimeric Antigen Receptor-Modified T Cells Derived from Defined CD8+ and CD4+ Subsets Confer Superior Antitumor Reactivity in Vivo. *Leukemia* **2016**, *30* (2), 492–500. https://doi.org/10.1038/leu.2015.247.

(101) Krug, C.; Wiesinger, M.; Abken, H.; Schuler-Thurner, B.; Schuler, G.; Dörrie, J.; Schaft, N. A GMP-Compliant Protocol to Expand and Transfect Cancer Patient T Cells with MRNA Encoding a Tumor-Specific Chimeric Antigen Receptor. *Cancer Immunol. Immunother.* **2014**, *63* (10), 999–1008. https://doi.org/10.1007/s00262-014-1572-5.
(102) Birkholz, K.; Hombach, A.; Krug, C.; Reuter, S.; Kershaw, M.; Kämpgen, E.; Schuler, G.; Abken, H.; Schaft, N.; Dörrie, J. Transfer of MRNA Encoding Recombinant Immunoreceptors Reprograms CD4+ and CD8+ T Cells for Use in the Adoptive Immunotherapy of Cancer. *Gene Ther.* **2009**, *16* (5), 596–604. https://doi.org/10.1038/gt.2008.189.
(103) Park, J. H.; Geyer, M. B.; Brentjens, R. J. CD19-Targeted CAR T-Cell Therapeutics for Hematologic Malignancies: Interpreting Clinical Outcomes to Date. *Blood*. American Society of Hematology June 30, 2016, pp 3312–3320. https://doi.org/10.1182/blood-2016-02-629063.
(104) Maude, S. L.; Teachey, D. T.; Porter, D. L.; Grupp, S. A. CD19-Targeted Chimeric Antigen Receptor T-Cell Therapy for Acute Lymphoblastic Leukemia. *Blood* **2015**, *125* (26), 4017–4023. https://doi.org/10.1182/blood-2014-12-580068.
(105) Davila, M. L.; Brentjens, R. J. CD19-Targeted CAR T Cells as Novel Cancer Immunotherapy for Relapsed or Refractory B-Cell Acute Lymphoblastic Leukemia. *Clin. Adv. Hematol. Oncol.* **2016**, *14* (10), 802–808.
(106) Kymriah vs. Yescarta [UPDATED] | Nucleus Biologics https://nucleusbiologics.com/resources/kymriah-vs-yescarta/ (accessed Jul 4, 2020).
(107) Adoptive Cell Therapy: CAR T, TCR, TIL, NK – Cancer Research Institute (CRI) https://www.cancerresearch.org/immunotherapy/treatment-types/adoptive-cell-therapy (accessed Jun 14, 2020).
(108) FDA-approved CAR T-cell Therapies | UPMC Hillman https://hillman.upmc.com/mario-lemieux-center/treatment/car-t-cell-therapy/fda-approved-therapies (accessed Jul 4, 2020).
(109) FDA approves CAR-T cell therapy to treat adults with certain types of large B-cell lymphoma | FDA https://www.fda.gov/news-events/press-announcements/fda-approves-car-t-cell-therapy-treat-adults-certain-types-large-b-cell-lymphoma (accessed Jul 4, 2020).
(110) Shi, J.; Ma, Y.; Zhu, J.; Chen, Y.; Sun, Y.; Yao, Y.; Yang, Z.; Xie, J. A Review on Electroporation-Based Intracellular Delivery. *Molecules*. MDPI AG November 21, 2018. https://doi.org/10.3390/molecules23113044.
(111) Jensen, M. C.; Riddell, S. R. Designing Chimeric Antigen Receptors to Effectively and Safely Target Tumors. *Current Opinion in Immunology*. Elsevier Ltd April 1, 2015, pp 9–15. https://doi.org/10.1016/j.coi.2015.01.002.
(112) Eshhar, Z.; Waks, T.; Gross, G.; Schindler, D. G. Specific Activation and Targeting of Cytotoxic Lymphocytes through Chimeric Single Chains Consisting of Antibody-Binding Domains and the γ or ζ Subunits of the Immunoglobulin and T-Cell Receptors. *Proc. Natl. Acad. Sci. U. S. A.* **1993**, *90* (2), 720–724. https://doi.org/10.1073/pnas.90.2.720.
(113) Benmebarek, M. R.; Karches, C. H.; Cadilha, B. L.; Lesch, S.; Endres, S.; Kobold, S. Killing Mechanisms of Chimeric Antigen Receptor (CAR) T Cells. *International Journal of Molecular Sciences*. MDPI AG March 2, 2019. https://doi.org/10.3390/ijms20061283.
(114) Martinez, M.; Moon, E. K. CAR T Cells for Solid Tumors: New Strategies for Finding, Infiltrating, and Surviving in the Tumor Microenvironment. *Front. Immunol.* **2019**, *10* (FEB), 128. https://doi.org/10.3389/fimmu.2019.00128.

(115) Kalos, M.; Levine, B. L.; Porter, D. L.; Katz, S.; Grupp, S. A.; Bagg, A.; June, C. H. T Cells with Chimeric Antigen Receptors Have Potent Antitumor Effects and Can Establish Memory in Patients with Advanced Leukemia. *Sci. Transl. Med.* **2011**, *3* (95). https://doi.org/10.1126/scitranslmed.3002842.
(116) Kochenderfer, J. N.; Rosenberg, S. A.; Rosenberg, A. Treating B-Cell Cancer with T Cells Expressing Anti-CD19 Chimeric Antigen Receptors. *Exp. Transplant. Immunol. Branch (J. N. Kochenderfer)*. https://doi.org/10.1038/nrclinonc.2013.46.
(117) Barrett, D. M.; Zhao, Y.; Liu, X.; Jiang, S.; Carpenito, C.; Kalos, M.; Carroll, R. G.; June, C. H.; Grupp, S. A. Treatment of Advanced Leukemia in Mice with MRNA Engineered T Cells. https://doi.org/10.1089/hum.2011.070.
(118) Wiehe, J. M.; Ponsaerts, P.; Rojewski, M. T.; Homann, J. M.; Greiner, J.; Kronawitter, D.; Schrezenmeier, H.; Hombach, V.; Wiesneth, M.; Zimmermann, O.; et al. MRNA-Mediated Gene Delivery Into Human Progenitor Cells Promotes Highly Efficient Protein Expression. *J. Cell. Mol. Med.* **2007**, *11* (3), 521–530. https://doi.org/10.1111/j.1582-4934.2007.00038.x.
(119) Gene Therapy Viral Vectors Explained http://www.genetherapynet.com/viral-vectors.html (accessed Jun 22, 2020).
(120) Schaffer, D. V.; Koerber, J. T.; Lim, K. Molecular Engineering of Viral Gene Delivery Vehicles. *Annu. Rev. Biomed. Eng.* **2008**, *10* (1), 169–194. https://doi.org/10.1146/annurev.bioeng.10.061807.160514.
(121) Pfeifer, A.; Verma, I. M. G ENE T HERAPY : Promises and Problems . *Annu. Rev. Genomics Hum. Genet.* **2001**, *2* (1), 177–211. https://doi.org/10.1146/annurev.genom.2.1.177.
(122) Foster, J. B.; Choudhari, N.; Perazzelli, J.; Storm, J.; Hofmann, T. J.; Jain, P.; Storm, P. B.; Pardi, N.; Weissman, D.; Waanders, A. J.; et al. Purification of MRNA Encoding Chimeric Antigen Receptor Is Critical for Generation of a Robust T-Cell Response. *Hum. Gene Ther.* **2019**, *30* (2), 168–178. https://doi.org/10.1089/hum.2018.145.
(123) Barrett, D. M.; Zhao, Y.; Liu, X.; Jiang, S.; Carpenito, C.; Kalos, M.; Carroll, R. G.; June, C. H.; Grupp, S. A. Treatment of Advanced Leukemia in Mice with MRNA Engineered T Cells. *Hum. Gene Ther.* **2011**, *22* (12), 1575–1586. https://doi.org/10.1089/hum.2011.070.
(124) Zheng, P. P.; Kros, J. M.; Li, J. Approved CAR T Cell Therapies: Ice Bucket Challenges on Glaring Safety Risks and Long-Term Impacts. *Drug Discovery Today*. Elsevier Ltd June 1, 2018, pp 1175–1182. https://doi.org/10.1016/j.drudis.2018.02.012.
(125) Sadelain, M. CD19 CAR T Cells. *Cell*. Cell Press December 14, 2017, p 1471. https://doi.org/10.1016/j.cell.2017.12.002.
(126) Hacein-Bey-Abina, S.; Garrigue, A.; Wang, G. P.; Soulier, J.; Lim, A.; Morillon, E.; Clappier, E.; Caccavelli, L.; Delabesse, E.; Beldjord, K.; et al. Insertional Oncogenesis in 4 Patients after Retrovirus-Mediated Gene Therapy of SCID-X1. *J. Clin. Invest.* **2008**, *118* (9), 3132–3142. https://doi.org/10.1172/JCI35700.
(127) Braun, C. J.; Boztug, K.; Paruzynski, A.; Witzel, M.; Schwarzer, A.; Rothe, M.; Modlich, U.; Beier, R.; Göhring, G.; Steinemann, D.; et al. Gene Therapy for Wiskott-Aldrich Syndrome-Long-Term Efficacy and Genotoxicity. *Sci. Transl. Med.* **2014**, *6* (227), 227ra33-227ra33. https://doi.org/10.1126/scitranslmed.3007280.
(128) Lee, D. W.; Gardner, R.; Porter, D. L.; Louis, C. U.; Ahmed, N.; Jensen, M.; Grupp, S. A.; Mackall, C. L. Current Concepts in the Diagnosis and Management of Cytokine Release Syndrome. *Blood* **2014**, *124* (2), 188–195. https://doi.org/10.1182/blood-2014-05-552729.

(129) Teachey, D. T.; Lacey, S. F.; Shaw, P. A.; Melenhorst, J. J.; Maude, S. L.; Frey, N.; Pequignot, E.; Gonzalez, V. E.; Chen, F.; Finklestein, J.; et al. Identification of Predictive Biomarkers for Cytokine Release Syndrome after Chimeric Antigen Receptor T-Cell Therapy for Acute Lymphoblastic Leukemia. *Cancer Discov.* **2016**, *6* (6), 664–679. https://doi.org/10.1158/2159-8290.CD-16-0040.
(130) Krug, C.; Wiesinger, M.; Abken, H.; Schuler-Thurner, B.; Schuler, G.; Dörrie, J.; Schaft, N. A GMP-Compliant Protocol to Expand and Transfect Cancer Patient T Cells with MRNA Encoding a Tumor-Specific Chimeric Antigen Receptor. *Cancer Immunol Immunother* **2014**, *3*, 999–1008. https://doi.org/10.1007/s00262-014-1572-5.
(131) Avci-Adali, M.; Behring, A.; Steinle, H.; Keller, T.; Krajeweski, S.; Schlensak, C.; Wendel, H. P. In Vitro Synthesis of Modified MRNA for Induction of Protein Expression in Human Cells. *J. Vis. Exp.* **2014**, No. 93, 51943. https://doi.org/10.3791/51943.
(132) Jani, B.; Fuchs, R. In Vitro Transcription and Capping of Gaussia Luciferase MRNA Followed by HeLa Cell Transfection. *J. Vis. Exp.* **2012**, No. 61. https://doi.org/10.3791/3702.
(133) Barrett, D. M.; Zhao, Y.; Liu, X.; Jiang, S.; Carpenito, C.; Kalos, M.; Carroll, R. G.; June, C. H.; Grupp, S. A. Treatment of Advanced Leukemia in Mice with MRNA Engineered T Cells. *Hum. Gene Ther.* **2011**, *22* (12), 1575–1586. https://doi.org/10.1089/hum.2011.070.
(134) Barrett, D. M.; Zhao, Y.; Liu, X.; Jiang, S.; Carpenito, C.; Kalos, M.; Carroll, R. G.; June, C. H.; Grupp, S. A. Treatment of Advanced Leukemia in Mice with MRNA Engineered T Cells. *Hum. Gene Ther.* **2011**, *22* (12), 1575–1586. https://doi.org/10.1089/hum.2011.070.
(135) Knochelmann, H. M.; Smith, A. S.; Dwyer, C. J.; Wyatt, M. M.; Mehrotra, S.; Paulos, C. M. CAR T Cells in Solid Tumors: Blueprints for Building Effective Therapies. *Frontiers in immunology*. NLM (Medline) July 27, 2018, p 1740. https://doi.org/10.3389/fimmu.2018.01740.
(136) Karikó, K.; Muramatsu, H.; Welsh, F. A.; Ludwig, J.; Kato, H.; Akira, S.; Weissman, D. Incorporation of Pseudouridine into MRNA Yields Superior Nonimmunogenic Vector with Increased Translational Capacity and Biological Stability. *Mol. Ther.* **2008**, *16* (11), 1833–1840. https://doi.org/10.1038/mt.2008.200.
(137) Rhizobium, G. E. Complete Genome Sequence of the Sesbania Symbiont and Rice. *Nucleic Acids Res.* **2013**, *1* (1256879), 13–14. https://doi.org/10.1093/nar.
(138) Santra, T.; Tseng, F. Recent Trends on Micro/Nanofluidic Single Cell Electroporation. *Micromachines* **2013**, *4* (3), 333–356. https://doi.org/10.3390/mi4030333.
(139) Chang, L.; Li, L.; Shi, J.; Sheng, Y.; Lu, W.; Gallego-Perez, D.; James Lee, L. Micro-/Nanoscale Electroporation. *Lab Chip* **2016**, *16* (21), 4047–4062. https://doi.org/10.1039/C6LC00840B.
(140) Fan, Y.; Bergmann, A. Apoptosis-Induced Compensatory Proliferation. The Cell Is Dead. Long Live the Cell! *Trends in Cell Biology*. October 2008, pp 467–473. https://doi.org/10.1016/j.tcb.2008.08.001.
(141) Bergmann, A.; Steller, H. Apoptosis, Stem Cells, and Tissue Regeneration. *Science Signaling*. October 26, 2010. https://doi.org/10.1126/scisignal.3145re8.
(142) Miltenyi, S.; Müller, W.; Weichel, W.; Radbruch, A. High Gradient Magnetic Cell Separation with MACS. *Cytometry* **1990**, *11* (2), 231–238. https://doi.org/10.1002/cyto.990110203.

(143) Sutermaster, B. A.; Darling, E. M. Considerations for High-Yield, High-Throughput Cell Enrichment: Fluorescence versus Magnetic Sorting. *Sci. Rep.* **2019**, *9* (1). https://doi.org/10.1038/s41598-018-36698-1.
(144) Ruella, M.; Xu, J.; Barrett, D. M.; Fraietta, J. A.; Reich, T. J.; Ambrose, D. E.; Klichinsky, M.; Shestova, O.; Patel, P. R.; Kulikovskaya, I.; et al. Induction of Resistance to Chimeric Antigen Receptor T Cell Therapy by Transduction of a Single Leukemic B Cell. *Nat. Med.* **2018**, *24* (10), 1499–1503. https://doi.org/10.1038/s41591-018-0201-9.
(145) Zheng, G.; Patolsky, F.; Cui, Y.; Wang, W. U.; Lieber, C. M. Multiplexed Electrical Detection of Cancer Markers with Nanowire Sensor Arrays. *Nat. Biotechnol.* **2005**, *23* (10), 1294. https://doi.org/10.1038/nbt1138.
(146) Joo, C.; Balci, H.; Ishitsuka, Y.; Buranachai, C.; Ha, T. Advances in Single-Molecule Fluorescence Methods for Molecular Biology. *Annu. Rev. Biochem.* **2008**, *77* (1), 51. https://doi.org/10.1146/annurev.biochem.77.070606.101543.
(147) Stern, E.; Vacic, A.; Rajan, N. K.; Criscione, J. M.; Park, J.; Ilic, B. R.; Mooney, D. J.; Reed, M. A.; Fahmy, T. M. Label-Free Biomarker Detection from Whole Blood. *Nat. Nanotechnol.* **2010**, *5* (2), 138.
(148) Pethig, R. Dielectrophoresis: Using Inhomogeneous AC Electrical Fields to Separate and Manipulate Cells. *Crit. Rev. Biotechnol.* **1996**, *16* (4), 331–348. https://doi.org/10.3109/07388559609147425.
(149) Morgan, H.; Hughes, M. P.; Green, N. G. Separation of Submicron Bioparticles by Dielectrophoresis. *Biophys. J.* **1999**. https://doi.org/10.1016/S0006-3495(99)76908-0.
(150) Li, H.; Bashir, R. *Dielectrophoretic Separation and Manipulation of Live and Heat-Treated Cells of Listeria on Microfabricated Devices with Interdigitated Electrodes*; Elsevier, 2002; Vol. 86, pp 215–221. https://doi.org/10.1016/S0925-4005(02)00172-7.
(151) Chou, C.-F.; Tegenfeldt, J. O.; Bakajin, O.; Chan, S. S.; Cox, E. C.; Darnton, N.; Duke, T.; Austin, R. H. Electrodeless Dielectrophoresis of Single- and Double-Stranded DNA. *Biophys. J.* **2002**, *83* (4), 2170–2179. https://doi.org/10.1016/S0006-3495(02)73977-5.
(152) Washizu, M.; Kurosawa, O. Electrostatic Manipulation of DNA in Microfabricated Structures. *IEEE Trans. Ind. Appl.* **1990**, *26* (6), 1165–1172. https://doi.org/10.1109/28.62403.
(153) Jones, T. B. *Electromechanics of Particles*; Cambridge University Press: Cambridge, 1995.
(154) Gascoyne, P. R. C.; Vykoukal, J. Particle Separation by Dielectrophoresis. *Electrophoresis* **2002**, *23* (13). https://doi.org/10.1002/1522-2683(200207)23:13<1973::AID-ELPS1973>3.0.CO;2-1.
(155) Becker, F. F.; Wang, X. B.; Huang, Y.; Pethig, R.; Vykoukal, J.; Gascoyne, P. R. C. Separation of Human Breast Cancer Cells from Blood by Differential Dielectric Affinity. *Proc. Natl. Acad. Sci. U. S. A.* **1995**, *92* (3), 860. https://doi.org/10.1073/pnas.92.3.860.
(156) Jones, T. B. Basic Theory of Dielectrophoresis and Electrorotation. *IEEE Eng. Med. Biol. Mag.* **2003**, *22* (6), 33–42. https://doi.org/10.1109/MEMB.2003.1304999.
(157) Gong, J.-R. Label-Free Attomolar Detection of Proteins Using Integrated Nanoelectronic and Electrokinetic Devices. *Small* **2010**, *6* (8), 967–973. https://doi.org/10.1002/smll.200902132.
(158) Jackson, J. D. *Classical Electrodynamics Third Edition*; john wiley & sons. Inc., 1999.

(159) Ramos, A.; Morgan, H.; Green, N. G.; Castellanos, A. *Ac Electrokinetics: A Review of Forces in Microelectrode Structures*; 1998; Vol. 31. https://doi.org/10.1088/0022-3727/31/18/021.
(160) Morgan, H.; Izquierdo, A. G.; Bakewell, D.; Green, N. G.; Ramos, A.; García Izquierdo, A.; Bakewell, D.; Green, N. G.; Ramos, A. The Dielectrophoretic and Travelling Wave Forces Generated by Interdigitated Electrode Arrays: Analytical Solution Using Fourier Series. *J. Phys. D Appl. Phys.* **2001**, *34* (10), 1553.
(161) Velmanickam, L.; Laudenbach, D.; Nawarathna, D. Dielectrophoretic Label-Free Immunoassay for Rare-Analyte Quantification in Biological Samples. *Phys. Rev. E* **2016**, *94* (4). https://doi.org/10.1103/PhysRevE.94.042408.
(162) Voigtländer, B. *Scanning Probe Microscopy: Atomic Force Microscopy and Scanning Tunneling Microscopy*; 2015.
(163) Martin, Y.; Williams, C. C.; Wickramasinghe, H. K. Atomic Force Microscope-Force Mapping and Profiling on a Sub 100-Å Scale. *J. Appl. Phys.* **1987**, *61* (10), 4723–4729. https://doi.org/10.1063/1.338807.
(164) S. N. Magonov, V. Elings, and M. H. W. Phase Imaging and Stiffness in Tapping-Mode Atomic Force Microscopy. *Surf. Sci.* **1997**, *375* (2–3), L385–L391.
(165) Green, N. G.; Ramos, A.; Morgan -Electrohydrodynamics, H.; in microsystems Castellanos, D. A.; González, A.; -, al; Morgan, H.; Castellanos, A. *Physics To Cite This Article: A Ramos et Al*; 1998; Vol. 31.
(166) Wei, M. T.; Junio, J.; Ou-Yang, D. H. Direct Measurements of the Frequency-Dependent Dielectrophoresis Force. In *Biomicrofluidics*; American Institute of Physics Inc., 2009; Vol. 3, p 012003. https://doi.org/10.1063/1.3058569.
(167) Imasato, H.; Yamakawa, T. Measurement of Dielectrophoretic Force by Employing Controllable Gravitational Force. *J. Electrophor.* **2008**, *52* (1), 1–8. https://doi.org/10.2198/jelectroph.52.1.
(168) Freedman, K. J.; Otto, L. M.; Ivanov, A. P.; Barik, A.; Oh, S. H.; Edel, J. B. Nanopore Sensing at Ultra-Low Concentrations Using Single-Molecule Dielectrophoretic Trapping. *Nat. Commun.* **2016**, *7*, 10217.
(169) Barik, A.; Zhang, Y.; Grassi, R.; Nadappuram, B. P.; Edel, J. B.; Low, T.; Koester, S. J.; Oh, S.-H. Graphene-Edge Dielectrophoretic Tweezers for Trapping of Biomolecules. *Nat. Commun.* **2017**, *8* (1), 1867. https://doi.org/10.1038/s41467-017-01635-9.
(170) Khoshmanesh, K.; Baratchi, S.; Tovar-Lopez, F. J.; Nahavandi, S.; Wlodkowic, D.; Mitchell, A.; Kalantar-zadeh, K. On-Chip Separation of Lactobacillus Bacteria from Yeasts Using Dielectrophoresis. *Microfluid. Nanofluid.* **2012**, *12* (1), 597.
(171) Markx, G. H.; Dyda, P. A.; Pethig, R. Dielectrophoretic Separation of Bacteria Using a Conductivity Gradient. *J. Biotechnol.* **1996**, *51* (2), 175.
(172) Shafiee, H.; Caldwell, J. L.; Sano, M. B.; Davalos, R. V. Contactless Dielectrophoresis: A New Technique for Cell Manipulation. *Biomed. Microdevices* **2009**, *11* (5), 997.
(173) Gossett, D. R.; Weaver, W. M.; Mach, A. J.; Hur, S. C.; Tse, H. T. K.; Lee, W.; Amini, H.; Di Carlo, D. Label-Free Cell Separation and Sorting in Microfluidic Systems. *Anal. Bioanal. Chem.* **2010**, *397* (8), 3249–3267. https://doi.org/10.1007/s00216-010-3721-9.
(174) Essevaz-Roulet, B.; Bockelmann, U.; Heslot, F. Mechanical Separation of the Complementary Strands of DNA. *Proc. Natl. Acad. Sci. U. S. A.* **1997**, *94* (22), 11935.
(175) Singh-Zocchi, M.; Dixit, S.; Ivanov, V.; Zocchi, G. Single-Molecule Detection of DNA Hybridization. *Proc. Natl. Acad. Sci. U. S. A.* **2003**, *100*, 7605.

(176) Perkins, T.; Dalal, R.; Mitsis, P.; Block, S. Sequence-Dependent Pausing of Single Lambda Exonuclease Molecules. *Sci. (Washington, DC, U. S.)* **2003**, *301*, 1914.
(177) Neuman, K. C.; Lionnet, T.; Allemand, J.-F. Single-Molecule Micromanipulation Techniques. *Annu. Rev. Mater. Res.* **2007**, *37* (1), 33.
(178) Ritort, F. Single-Molecule Experiments in Biological Physics: Methods and Applications. *J. Phys. Condens. Matter* **2006**, *18* (32), R531.
(179) Neuman, K. C.; Nagy, A. Single-Molecule Force Spectroscopy: Optical Tweezers, Magnetic Tweezers and Atomic Force Microscopy. *Nat. Methods* **2008**, *5* (6), 491.
(180) Brown, K. A.; Westervelt, R. M. Triaxial AFM Probes for Noncontact Trapping and Manipulation. *Nano Lett.* **2011**, *11* (8), 3197.
(181) Brown, K. A.; Aguilar, J. A.; Westervelt, R. M. Coaxial Atomic Force Microscope Tweezers. *Appl. Phys. Lett.* **2010**, *96* (12), 123109.
(182) Tao, Y.; Kumar Wickramasinghe, H. Coaxial Atomic Force Microscope Probes for Dielectrophoresis of DNA under Different Buffer Conditions. *Appl. Phys. Lett.* **2017**, *110* (7), 73701.
(183) Zhou, P. L.; Yu, H. B.; Yang, W. G.; Wen, Y. D.; Wang, Z. D.; Li, W. J.; Liu, L. Q. Spatial Manipulation and Assembly of Nanoparticles by Atomic Force Microscopy Tip-Induced Dielectrophoresis. *ACS Appl. Mater. Interfaces* **2017**, *9* (19), 16715.
(184) Clarke, R. W.; White, S. S.; Zhou, D.; Ying, L.; Klenerman, D. Trapping of Proteins under Physiological Conditions in a Nanopipette. *Angew. Chemie Int. Ed.* **2005**, *44* (24), 3747–3750. https://doi.org/10.1002/anie.200500196.
(185) Ying, L.; White, S. S.; Bruckbauer, A.; Meadows, L.; Korchev, Y. E.; Klenerman, D. Frequency and Voltage Dependence of the Dielectrophoretic Trapping of Short Lengths of DNA and DCTP in a Nanopipette. *Biophys. J.* **2004**, *86* (2), 1018–1027. https://doi.org/10.1016/S0006-3495(04)74177-6.
(186) Froberg, J.; Jayasooriya, V.; You, S.; Nawarathna, D.; Choi, Y. Quantitative Measurements of Dielectrophoresis in a Nanoscale Electrode Array with an Atomic Force Microscopy. *Appl. Phys. Lett.* **2017**, *110* (20), 203701. https://doi.org/10.1063/1.4983785.
(187) Morgan, H.; Izquierdo, A. G.; Bakewell, D.; Green, N. G.; Ramos, A. The Dielectrophoretic and Travelling Wave Forces Generated by Interdigitated Electrode Arrays: Analytical Solution Using Fourier Series. *J. Phys. D Appl. Phys.* **2001**, *34* (10), 1553.
(188) Jayasooriya, V.; Nawarathna, D. Design of Micro-Interdigitated Electrodes and Detailed Impedance Data Analysis for Label-Free Biomarker Quantification. *Electroanalysis* **2017**, *29* (2), 330–338. https://doi.org/10.1002/elan.201600364.
(189) Bakewell, D. J.; Vergara-Irigaray, N.; Holmes, D. Dielectrophoresis of Biomolecules. *JSM Nanotechnol. Nanomed.* **2013**, *1* (1), 1003.
(190) Regtmeier, J.; Duong, T. T.; Eichhorn, R.; Anselmetti, D.; Ros, A. Dielectrophoretic Manipulation of DNA: Separation and Polarizability. *Anal. Chem.* **2007**, *79* (10), 3925.
(191) Bakewell, D. J.; Morgan, H. Dielectrophoresis of DNA: Time- and Frequency-Dependent Collections on Microelectrodes. *IEEE Trans. Nanobiosci.* **2006**, *5* (2), 139.
(192) Regtmeier, J.; Eichhorn, R.; Bogunovic, L.; Ros, A.; Anselmetti, D. Dielectrophoretic Trapping and Polarizability of DNA: The Role of Spatial Conformation. *Anal. Chem.* **2010**, *82* (17), 7141.

(193) Tuukkanen, S.; Toppari, J. J.; Kuzyk, A.; Hirviniemi, L.; Hytonen, V. P.; Ihalainen, T.; Torma, P. Carbon Nanotubes as Electrodes for Dielectrophoresis of DNA. *Nano Lett.* **2006**, *6* (7), 1339.
(194) Bone, S.; Small, C. A. Dielectric Studies of Ion Fluctuation and Chain Bending in Native DNA. *Biochim. Biophys. Acta, Gene Struct. Expr.* **1995**, *1260* (1), 85.
(195) Sung, K. E.; Burns, M. A. Optimization of Dielectrophoretic DNA Stretching in Microfabricated Devices. *Anal. Chem.* **2006**, *78* (9), 2939.
(196) Chiou, C.-H.; Chien, L.-J.; Kuo, J.-N. Nanoconstriction-Based Electrodeless Dielectrophoresis Chip for Nanoparticle and Protein Preconcentration. *Appl. Phys. Express* **2015**, *8* (8), 85201.
(197) Green, N. G.; Jones, T. B. Numerical Determination of the Effective Moments of Non-Spherical Particles. *J. Phys. D Appl. Phys.* **2007**, *40* (1), 78.
(198) Gan, L.; Camacho-Alanis, F.; Ros, A. Polarizability of Six-Helix Bundle and Triangle DNA Origami and Their Escape Characteristics from a Dielectrophoretic Trap. *Anal. Chem.* **2015**, *87* (24), 12059.
(199) Bakewell, D. J.; Ermolina, I.; Morgan, H.; Milner, J.; Feldman, Y. Dielectric Relaxation Measurements of 12 Kbp Plasmid DNA. *Biochim. Biophys. Acta, Gene Struct. Expr.* **2000**, *1493* (1), 151.
(200) Tuukkanen, S.; Kuzyk, A.; Jussi Toppari, J.; Häkkinen, H.; Hytönen, V. P.; Niskanen, E.; Rinkiö, M.; Törmä, P. Trapping of 27 Bp-8 Kbp DNA and Immobilization of Thiol-Modified DNA Using Dielectrophoresis. *Nanotechnology* **2007**. https://doi.org/10.1088/0957-4484/18/29/295204.
(201) Martinez-Duarte, R.; Camacho-Alanis, F.; Renaud, P.; Ros, A. Dielectrophoresis of Lambda-DNA Using 3D Carbon Electrodes. *Electrophoresis* **2013**, *34* (7), 1113–1122. https://doi.org/10.1002/elps.201200447.
(202) Teraoka, I. No Title. *Polym. Solut. Introd. to Phys. Prop.* **2002**, 360.
(203) Määttänen, L.; Auvinen, A.; Stenman, U.-H.; Tammela, T.; Rannikko, S.; Aro, J.; Juusela, H.; Hakama, M. *BRIEF COMMUNICATION Three-Year Results of the Finnish Prostate Cancer Screening Trial Downloaded From*; 2001; Vol. 93.
(204) L. Lasseter, T.; Cai, W.; J. Hamers, R. Frequency-Dependent Electrical Detection of Protein Binding Events. *Analyst* **2004**, *129* (1), 3–8. https://doi.org/10.1039/B307591E.
(205) Berggren, C.; Stålhandske, P.; Brundell, J.; Johansson, G. A Feasibility Study of a Capacitive Biosensor for Direct Detection of DNA Hybridization. *Electroanalysis* **1999**, *11* (3), 156–160. https://doi.org/10.1002/(SICI)1521-4109(199903)11:3<156::AID-ELAN156>3.0.CO;2-O.
(206) Bargmann, V.; Michel Ecole Polytechnigue, L.; Telegdi, V. L. *PHYSICAL REVIEW LETTERS Mxv 15, 1959 PRECESSION OF THE POLARIZATION OF PARTICLES MOVING IN A HOMOGENEOUS ELECTROMAGNETIC FIELD*; Vol. 2.
(207) H. J. Levinson. *Principles of Lithography*, 2nd Edition.; SPIE: Bellingham, 2005.
(208) Hu, X.; Bessette, P. H.; Qian, J.; Meinhart, C. D.; Daugherty, P. S.; Soh, H. T. Marker-Specific Sorting of Rare Cells Using Dielectrophoresis. *Proc. Natl. Acad. Sci. U. S. A.* **2005**, *102* (44), 15757–15761. https://doi.org/10.1073/pnas.0507719102.
(209) Nawarathna, D.; Turan, T.; Kumar Wickramasinghe, H. Selective Probing of MRNA Expression Levels within a Living Cell. *Appl. Phys. Lett* **2009**, *95*, 83117. https://doi.org/10.1063/1.3213343.

(210) Maupas, H.; Saby, C.; Martelet, C.; Jaffrezic-Renault, N.; Soldatkin, A. P.; Charles, M. H.; Delair, T.; Mandrand, B. Impedance Analysis of Si/SiO2 Heterostructures Grafted with Antibodies: An Approach for Immunosensor Development. *J. Electroanal. Chem.* **1996**, *406* (1–2), 53–58. https://doi.org/10.1016/0022-0728(95)04443-4.
(211) Gebbert, A.; Alvarez-Icaza, M.; Stocklein, W.; Schmid, R. D. *Real-Time Monitoring of Immunochemical Interactions with a Tantalum Capacitance Flow-Through Cell*; 1992; Vol. 64.
(212) G. Rizzoni. *Principles and Applications of Electrical Engineering*; McGraw-Hill Science/Engineering/Math, 2005.
(213) Wang, J. C. Realizations of Generalized Warburg Impedance with RC Ladder Networks and Transmission Lines. **1987**, *134* (8), 1915–1920. https://doi.org/10.1149/1.2100789.
(214) Zetterberg, H.; Burnham, S. C. Blood-Based Molecular Biomarkers for Alzheimer's Disease. *Mol. Brain* **2019**, *12* (1), 26. https://doi.org/10.1186/s13041-019-0448-1.
(215) O'Reilly, E.; Tuzova, A. V.; Walsh, A. L.; Russell, N. M.; O'Brien, O.; Kelly, S.; Dhomhnallain, O. N.; DeBarra, L.; Dale, C. M.; Brugman, R.; et al. EpiCaPture: A Urine DNA Methylation Test for Early Detection of Aggressive Prostate Cancer. *JCO Precis. Oncol.* **2019**, No. 3, 1–18. https://doi.org/10.1200/po.18.00134.
(216) Herreros-Villanueva, M.; Duran-Sanchon, S.; Martín, A. C.; Pérez-Palacios, R.; Vila-Navarro, E.; Marcuello, M.; Diaz-Centeno, M.; Cubiella, J.; Diez, M. S.; Bujanda, L.; et al. Plasma MicroRNA Signature Validation for Early Detection of Colorectal Cancer. *Clin. Transl. Gastroenterol.* **2019**, *10* (1), e00003. https://doi.org/10.14309/ctg.0000000000000003.
(217) Niu, Y.; Su, M.; Wu, Y.; Fu, L.; Kang, K.; Li, Q.; Li, L.; Hui, G.; Li, F.; Gou, D. Circulating Plasma MiRNAs as Potential Biomarkers of Non-Small Cell Lung Cancer Obtained by High-Throughput Real-Time PCR Profiling. *Cancer Epidemiol. Biomarkers Prev.* **2019**, *28* (2), 327–336. https://doi.org/10.1158/1055-9965.EPI-18-0723.
(218) Selvamani, Amutha 1; Lewis, Debbie 2; Lewis, Brandon 3; Spohn, MIcheal J 3; Sohrabji, F. 1. No Title. *Abstr. WP196 MicroRNA IGF-1 as Predict. Biomarkers Stroke Outcomes* **2019**, *Stroke. 50*, AWP196.
(219) Chen, C.; Ridzon, D. A.; Broomer, A. J.; Zhou, Z.; Lee, D. H.; Nguyen, J. T.; Barbisin, M.; Xu, N. L.; Mahuvakar, V. R.; Andersen, M. R.; et al. Real-Time Quantification of MicroRNAs by Stem-Loop RT-PCR. *Nucleic Acids Res.* **2005**, *33* (20). https://doi.org/10.1093/nar/gni178.
(220) Friedländer, M. R.; Chen, W.; Adamidi, C.; Maaskola, J.; Einspanier, R.; Knespel, S.; Rajewsky, N. Discovering MicroRNAs from Deep Sequencing Data Using MiRDeep A N A LY S I S. *Nat. Biotechnol. Vol.* **2008**, *26* (4). https://doi.org/10.1038/nbt1394.
(221) Lodes, M. J.; Caraballo, M.; Suciu, D.; Munro, S.; Kumar, A.; Anderson, B. Detection of Cancer with Serum MiRNAs on an Oligonucleotide Microarray. *PLoS One* **2009**, *4* (7). https://doi.org/10.1371/journal.pone.0006229.
(222) Bettazzi, F.; Hamid-Asl, E.; Esposito, C. L.; Quintavalle, C.; Formisano, N.; Laschi, S.; Catuogno, S.; Iaboni, M.; Marrazza, G.; Mascini, M.; et al. Electrochemical Detection of MiRNA-222 by Use of a Magnetic Bead-Based Bioassay. *Anal. Bioanal. Chem.* **2013**, *405* (2–3), 1025–1034. https://doi.org/10.1007/s00216-012-6476-7.
(223) Jiao, L.; Zhang, L.; Du, W.; Li, H.; Yang, D.; Zhu, C. Au@Pt Nanodendrites Enhanced Multimodal Enzyme-Linked Immunosorbent Assay †. **2019**. https://doi.org/10.1039/c8nr08741e.

(224) Lai, S.-C.; Huang, Y.-Y.; Shu, P.-Y.; Chang, S.-F.; Hsieh, P.-S.; Wey, J.-J.; Tsai, M.-H.; Ben, R.-J.; Hsu, Y.-M.; Fang, Y.-C.; et al. *Development of an Enzyme-Linked Immunosorbent Assay for Rapid Detection of Dengue Virus (DENV) NS1 and Differentiation of DENV Serotypes during Early Infection Downloaded From*; 2019; Vol. 57.
(225) Akter, T.; Atanelishvili, I.; Noguchi, A.; Silver, R. M.; Bogatkevich, G. S. Establishment of an Indirect ELISA for Detection of the Novel Antifibrotic Peptide M10. *PLoS One* **2017**, *12* (11). https://doi.org/10.1371/journal.pone.0188588.
(226) Nelson, R.J., Hooper, H.H., Hauser, A.K., Singh, S., Williams, S. J. and S. Microfluidic Method for Nucleic Acid Amplification. 6074827, February 5, 2000. https://doi.org/10.1016/s0294-3506(98)80053-7.
(227) Acquah, C.; Chan, Y. W.; Pan, S.; Agyei, D.; Udenigwe, C. C. Structure-Informed Separation of Bioactive Peptides. *J. Food Biochem.* **2019**, *43* (1), e12765. https://doi.org/10.1111/jfbc.12765.
(228) Margalit, S.; Avraham, S.; Shahal, T.; Michaeli, Y.; Gilat, N.; Magod, P.; Caspi, M.; Loewenstein, S.; Lahat, G.; Friedmann-Morvinski, D.; et al. 5-Hydroxymethylcytosine as a Clinical Biomarker: Fluorescence-based Assay for High-throughput Epigenetic Quantification in Human Tissues. *Int. J. Cancer* **2020**, *146* (1), 115–122. https://doi.org/10.1002/ijc.32519.
(229) Zhang, H.; Chang, H.; Neuzil, P. DEP-on-a-Chip: Dielectrophoresis Applied to Microfluidic Platforms. *Micromachines* **2019**, *10* (6), 423. https://doi.org/10.3390/mi10060423.
(230) Sanghavi, B. J.; Wolfbeis, O. S.; Hirsch, T.; Swami, N. S. Nanomaterial-Based Electrochemical Sensing of Neurological Drugs and Neurotransmitters. *Microchimica Acta*. Springer-Verlag Wien July 8, 2015, pp 1–41. https://doi.org/10.1007/s00604-014-1308-4.
(231) Fernandez, R. E.; Rohani, A.; Farmehini, V.; Swami, N. S. *Review: Microbial Analysis in Dielectrophoretic Microfluidic Systems*; Elsevier B.V., 2017; Vol. 966, pp 11–33. https://doi.org/10.1016/j.aca.2017.02.024.
(232) Kim, H. J.; Ahn, H.; Lee, D. S.; Park, D.; Kim, J. H.; Kim, J.; Yoon, D. S.; Hwang, K. S. Highly Sensitive Micropatterned Interdigitated Electrodes for Enhancing the Concentration Effect Based on Dielectrophoresis. *Sensors* **2019**, *19* (19), 4152. https://doi.org/10.3390/s19194152.
(233) Lentz, C. J.; Hidalgo-Caballero, S.; Lapizco-Encinas, B. H. Low Frequency Cyclical Potentials for Fine Tuning Insulator-Based Dielectrophoretic Separations. *Biomicrofluidics* **2019**, *13* (4), 044114. https://doi.org/10.1063/1.5115153.
(234) Ladik, L. S. G. B. J.; Seprödi, L.; Biczó, G.; Ladik, J. The Effect of Electric Field on the Electronic Structure of DNA. I. Calculation of the Polarizability and of the Permanent Dipole Moment for the Nucleotide Bases and Base Pairs. *Int. J. Quantum Chem.* **1969**, *3* (5), 621–634. https://doi.org/10.1002/qua.560030509.
(235) Goldak, J.; Chakravarti, A.; Bibby, M. *A New Finite Element Model for Welding Heat Sources*.
(236) Reichl, M.; Herzog, M.; Greiss, F.; Wolff, M.; Braun, D. Understanding the Similarity in Thermophoresis between Single-and Double-Stranded DNA or RNA. *Phys. Rev. E* **2015**, *91*, 62709. https://doi.org/10.1103/PhysRevE.91.062709.

(237) Chicas, M.; Roman, R.; Sevedge, K.; Kenna, J.; Miller, A.; Beaupre, L.; Zubia, J.; Smith, C. B.; Pauls, A.; Walczer, T. The Effect of Early Detection and Treatment of Early-Stage Lung Cancer on the Thoracic Navigator Role...Tenth Annual AONN+ Navigation & Survivorship Conference, November 6-10, 2019, Nashville, TN. *J. Oncol. Navig. Surviv.* **2019**, *10* (11), 454–455.
(238) Chen, D. Q.; Cao, G.; Chen, H.; Argyopoulos, C. P.; Yu, H.; Su, W.; Chen, L.; Samuels, D. C.; Zhuang, S.; Bayliss, G. P.; et al. Identification of Serum Metabolites Associating with Chronic Kidney Disease Progression and Anti-Fibrotic Effect of 5-Methoxytryptophan. *Nat. Commun.* **2019**, *10* (1). https://doi.org/10.1038/s41467-019-09329-0.
(239) Gençay Can, A.; Ekşioğlu, E.; Çakçl, F. A. Early Detection and Treatment of Subclinical Lymphedema in Patients with Breast Cancer. *Lymphat. Res. Biol.* **2019**, *17* (3), 368–373. https://doi.org/10.1089/lrb.2018.0033.
(240) Kim, T. K.; Eberwine, J. H. Mammalian Cell Transfection: The Present and the Future. **2010**. https://doi.org/10.1007/s00216-010-3821-6.
(241) Glover, D. J.; Lipps, H. J.; Jans, D. A. Towards Safe, Non-Viral Therapeutic Gene Expression in Humans. *Nature Reviews Genetics*. Nature Publishing Group April 10, 2005, pp 299–310. https://doi.org/10.1038/nrg1577.
(242) Recillas-Targa, F. *Mammalian Gene Transfer and Expression 337 MOLECULAR BIOTECHNOLOGY Abstract Multiple Strategies for Gene Transfer, Expression, Knockdown, and Chromatin Influence in Mammalian Cell Lines and Transgenic Animals*; 2006.
(243) Verma, I. M.; Weitzman, M. D. GENE THERAPY: Twenty-First Century Medicine. *Annu. Rev. Biochem.* **2005**, *74* (1), 711–738. https://doi.org/10.1146/annurev.biochem.74.050304.091637.
(244) Gene Therapy Viral Vectors Explained http://www.genetherapynet.com/viral-vectors.html (accessed Jun 18, 2020).
(245) Oncology's Fifth Pillar: Cellular Immunotherapy https://www.genengnews.com/magazine/august-2019-vol-39-no-8/oncologys-fifth-pillar-cellular-immunotherapy/ (accessed Jun 21, 2020).
(246) Wadhwa, P. D.; Zielske, S. P.; Roth, J. C.; Ballas, C. B.; Bowman, J. E.; Gerson, S. L. Cancer Gene Therapy: Scientific Basis. *Annu. Rev. Med.* **2002**, *53* (1), 437–452. https://doi.org/10.1146/annurev.med.53.082901.104039.
(247) Production of CAR-T Cells Using mRNA Transfection | Bioradiations https://www.bioradiations.com/gmp-compliant-production-of-car-t-cells-using-mrna-transfection/ (accessed Jul 1, 2020).
(248) Singh, K.; Lin, J.; Zhong, Y.; Burčul, A.; Mohan, P.; Jiang, M.; Sun, L.; Yong-Gonzalez, V.; Viale, A.; Cross, J. R.; et al. C-MYC Regulates MRNA Translation Efficiency and Start-Site Selection in Lymphoma. *J. Exp. Med.* **2019**, *216* (7), 1509–1524. https://doi.org/10.1084/jem.20181726.
(249) Ghartey-Tagoe, E. B.; Morgan, J. S.; Ahmed, K.; Neish, A. S.; Prausnitz, M. R. Electroporation-Mediated Delivery of Molecules to Model Intestinal Epithelia. *Int. J. Pharm.* **2004**, *270* (1), 127–138. https://doi.org/10.1016/j.ijpharm.2003.10.009.
(250) Rubinsky, B.; Onik, G.; Mikus, P. Irreversible Electroporation: A New Ablation Modality - Clinical Implications. *Technol. Cancer Res. Treat.* **2007**, *6* (1), 37–48. https://doi.org/10.1177/153303460700600106.

(251) Irreversible Electroporation (NanoKnife) - Medical Clinical Policy Bulletins | Aetna http://www.aetna.com/cpb/medical/data/800_899/0828.html (accessed Jun 22, 2020).
(252) Saulis, G.; Venslauskas, M. S. Cell Electroporation: Part 1. Theoretical Simulation of the Process of Pore Formation in a Cell. *Bioelectrochemistry Bioenerg.* **1993**, *32* (3), 221–235. https://doi.org/10.1016/0302-4598(93)80047-X.
(253) Dermol, J.; Pakhomova, O. N.; Pakhomov, A. G.; Miklavčič, D. Cell Electrosensitization Exists Only in Certain Electroporation Buffers. *PLoS One* **2016**, *11* (7), e0159434. https://doi.org/10.1371/journal.pone.0159434.
(254) Miklavč, D.; Kotnik, T. *Electroporation for Electrochemotherapy and Gene Therapy*.
(255) Weaver, J. C.; Chizmadzhev, Y. A. Theory of Electroporation: A Review. *Bioelectrochemistry Bioenerg.* **1996**, *41* (2), 135–160. https://doi.org/10.1016/S0302-4598(96)05062-3.
(256) Gehl, J. Electroporation: Theory and Methods, Perspectives for Drug Delivery, Gene Therapy and Research. *Acta Physiol. Scand.* **2003**, *177* (4), 437–447. https://doi.org/10.1046/j.1365-201X.2003.01093.x.
(257) Krassowska, W.; Filev, P. D. Modeling Electroporation in a Single Cell. *Biophys. J.* **2007**, *92* (2), 404–417. https://doi.org/10.1529/biophysj.106.094235.
(258) Bilska, A. O.; DeBruin, K. A.; Krassowska, W. Theoretical Modeling of the Effects of Shock Duration, Frequency, and Strength on the Degree of Electroporation. *Bioelectrochemistry* **2000**, *51* (2), 133–143. https://doi.org/10.1016/S0302-4598(00)00066-0.
(259) Brenner, M. K.; Heslop, H. E. Adoptive T Cell Therapy of Cancer. *Current Opinion in Immunology*. April 2010, pp 251–257. https://doi.org/10.1016/j.coi.2010.01.020.
(260) Kalos, M.; June, C. H. Adoptive T Cell Transfer for Cancer Immunotherapy in the Era of Synthetic Biology. *Immunity*. July 25, 2013, pp 49–60. https://doi.org/10.1016/j.immuni.2013.07.002.
(261) O'connell, J.; O'sullivan, G. C.; Collins, J. K.; Shanahan, F. *The Fas Counterattack: Fas-Mediated T Cell Killing by Colon Cancer Cells Expressing Fas Ligand*.
(262) Zhan, Y.; Cao, Z.; Bao, N.; Li, J.; Wang, J.; Geng, T.; Lin, H.; Lu, C. Low-Frequency Ac Electroporation Shows Strong Frequency Dependence and Yields Comparable Transfection Results to Dc Electroporation. *J. Control. Release* **2012**, *160* (3), 570–576. https://doi.org/10.1016/j.jconrel.2012.04.006.
(263) Kim, S. K.; Kim, J. H.; Kim, K. P.; Chung, T. D. Continuous Low-Voltage Dc Electroporation on a Microfluidic Chip with Polyelectrolytic Salt Bridges. *Anal. Chem.* **2007**, *79* (20), 7761–7766. https://doi.org/10.1021/ac071197h.
(264) Kell, D. B.; Astumian, R. D. Mechanisms for the Interaction between Nonstationary Electric Fields and Biological Systems Ii. Nonlinear Dielectric Theory and Free-Energy Transduction. *Ferroelectrics* **1988**, *86* (1), 79–101. https://doi.org/10.1080/00150198808227005.
(265) Li, Y.; Dalton, C.; Crabtree, H. J.; Nilsson, G.; Kaler, K. V. I. S. Continuous Dielectrophoretic Cell Separation Microfluidic Device. *Lab Chip* **2007**, *7* (2), 239–248. https://doi.org/10.1039/b613344d.
(266) Adams, T. N. G.; Jiang, A. Y. L.; Vyas, P. D.; Flanagan, L. A. Separation of Neural Stem Cells by Whole Cell Membrane Capacitance Using Dielectrophoresis. *Methods*. Academic Press Inc. January 15, 2018, pp 91–103. https://doi.org/10.1016/j.ymeth.2017.08.016.

(267) Xing, X.; Ng, C. N.; Chau, M. L.; Yobas, L. Railing Cells along 3D Microelectrode Tracks for Continuous-Flow Dielectrophoretic Sorting. *Lab Chip* **2018**, *18* (24), 3760–3769. https://doi.org/10.1039/c8lc00805a.
(268) Pommer, M. S.; Zhang, Y.; Keerthi, N.; Chen, D.; Thomson, J. A.; Meinhart, C. D.; Soh, H. T. Dielectrophoretic Separation of Platelets from Diluted Whole Blood in Microfluidic Channels. *Electrophoresis* **2008**, *29* (6), 1213–1218. https://doi.org/10.1002/elps.200700607.
(269) Rohani, A.; Moore, J. H.; Kashatus, J. A.; Sesaki, H.; Kashatus, D. F.; Swami, N. S. Label-Free Quantification of Intracellular Mitochondrial Dynamics Using Dielectrophoresis. *Anal. Chem.* **2017**, *89* (11), 5757–5764. https://doi.org/10.1021/acs.analchem.6b04666.
(270) Nakano, A.; Ros, A. Protein Dielectrophoresis: Advances, Challenges, and Applications. *Electrophoresis* **2013**, *34* (7), 1085–1096. https://doi.org/10.1002/elps.201200482.
(271) Nakano, A.; Luo, J.; Ros, A. Temporal and Spatial Temperature Measurement in Insulator-Based Dielectrophoretic Devices. *Anal. Chem.* **2014**, *86* (13), 6516–6524. https://doi.org/10.1021/ac501083h.
(272) Nin, D. F.; Sodhi, C. P.; Egan, C. E.; Zhou, Q.; Lin, J.; Lu, P.; Yamaguchi, Y.; Jia, H.; Martin, L. Y.; Good, M.; et al. Retinoic Acid Improves Incidence and Severity of Necrotizing Enterocolitis by Lymphocyte Balance Restitution and Repopulation of Lgr5 + Intestinal Stem Cells. *Shock* **2017**, *47* (1), 22–32. https://doi.org/10.1097/SHK.0000000000000713.
(273) Velmanickam, L.; Nawarathna, D. *Design and Fabrication of a Dielectrophoretic Cell Trap Array*.
(274) Richard P. HauglandIan C. MacCoubreyPatrick L. Moore and Molecular Probes Inc. Dual-Fluorescence Cell Viability Assay Using Ethidium Homodimer and Calcein AM. US Patent 5,314,805, 1994.
(275) Zhu, K.; Kaprelyants, A. S.; Salina, E. G.; Markx, G. H. Separation by Dielectrophoresis of Dormant and Nondormant Bacterial Cells of Mycobacterium Smegmatis. *Biomicrofluidics* **2010**, *4* (2). https://doi.org/10.1063/1.3435335.
(276) Ruella, M.; Xu, J.; Barrett, D. M.; Fraietta, J. A.; Reich, T. J.; Ambrose, D. E.; Klichinsky, M.; Shestova, O.; Patel, P. R.; Kulikovskaya, I.; et al. Induction of Resistance to Chimeric Antigen Receptor T Cell Therapy by Transduction of a Single Leukemic B Cell. *Nat. Med.* **2018**, *24* (10), 1499–1503. https://doi.org/10.1038/s41591-018-0201-9.
(277) Panagopoulou, T. I.; Rafiq, Q. A. CAR-T Immunotherapies: Biotechnological Strategies to Improve Safety, Efficacy and Clinical Outcome through CAR Engineering. *Biotechnology Advances*. Elsevier Inc. November 15, 2019, p 107411. https://doi.org/10.1016/j.biotechadv.2019.06.010.
(278) Suzuki, A.; Nakauchi, H.; Taniguchi, H. Prospective Isolation of Multipotent Pancreatic Progenitors Using Flow-Cytometric Cell Sorting. *Diabetes* **2004**, *53* (8), 2143–2152. https://doi.org/10.2337/diabetes.53.8.2143.
(279) Jayasooriya, V. D.; Nawarathna, D. Label-Free Purification of Viable Human T-Lymphocyte Cells from a Mixture of Viable and Non-Viable Cells after Transfection by Electroporation. *J. Phys. D. Appl. Phys.* **2019**, *52* (36). https://doi.org/10.1088/1361-6463/ab2b81.
(280) Pommer, M. S.; Zhang, Y.; Keerthi, N.; Chen, D.; Thomson, J. A.; Meinhart, C. D.; Soh, H. T. Dielectrophoretic Separation of Platelets from Diluted Whole Blood in Microfluidic

Channels. *Electrophoresis* **2008**, *29* (6), 1213–1218. https://doi.org/10.1002/elps.200700607.
(281) Faraghat, S. A.; Hoettges, K. F.; Steinbach, M. K.; Van Der Veen, D. R.; Brackenbury, W. J.; Henslee, E. A.; Labeed, F. H.; Hughes, M. P. High-Throughput, Low-Loss, Low-Cost, and Label-Free Cell Separation Using Electrophysiology-Activated Cell Enrichment. *Proc. Natl. Acad. Sci. U. S. A.* **2017**, *114* (18), 4591–4596. https://doi.org/10.1073/pnas.1700773114.
(282) Velmanickam, L.; Nawarathna, K. Dielectrophoretic Cell Isolation in Microfluidics Channels for High-Throughput Biomedical Applications. In *IEEE International Conference on Electro Information Technology*; IEEE Computer Society, 2016; Vol. 2016-August, pp 302–306. https://doi.org/10.1109/EIT.2016.7535256.
(283) Thomas, R. S. W.; Mitchell, P. D.; Oreffo, R. O. C.; Morgan, H.; Green, N. G. Image-based Sorting and Negative Dielectrophoresis for High Purity Cell and Particle Separation. *Electrophoresis* **2019**, *40* (20), 2718–2727. https://doi.org/10.1002/elps.201800489.
(284) Yildizhan, Y.; Erdem, N.; Islam, M.; Martinez-Duarte, R.; Elitas, M. Dielectrophoretic Separation of Live and Dead Monocytes Using 3D Carbon-Electrodes. *Sensors* **2017**, *17* (11), 2691. https://doi.org/10.3390/s17112691.
(285) Domingo, E.; Moreno, C.; Sánchez-Ibarrola, A.; Panizo, C.; Páramo, J. A.; Merino, J. Enhanced Sensitivity of Flow Cytometry for Routine Assessment of Minimal Residual Disease. *Haematologica*. Ferrata Storti Foundation April 2010, pp 691–692. https://doi.org/10.3324/haematol.2009.018911.
(286) Guo, M.; Li, X.; Zhang, S.; Song, H.; Zhang, W.; Shang, X.; Zheng, Y.; Jiang, H.; Lv, Q.; Jiang, Y.; et al. Real-Time Quantitative RT-PCR Detection of Circulating Tumor Cells from Breast Cancer Patients. *Int. J. Oncol.* **2015**, *46* (1), 281–289. https://doi.org/10.3892/ijo.2014.2732.
(287) Guo, J. Q.; Wang, J. Y. J.; Arlinghaus, R. B. Detection of BCR-ABL Proteins in Blood Cells of Benign Phase Chronic Myelogenous Leukemia Patients. *Cancer Res.* **1991**, *51* (11).
(288) Sidorova, J. Y.; Saltykova, L. B.; Lyschov, A. A.; Zaritskey, A. Y.; Abdulkadyrov, K. M.; Blinov, M. N. A Rapid RT-PCR Based Method for the Detection of BCR-ABL Translocation. *J. Clin. Pathol. - Mol. Pathol.* **1997**, *50* (5), 266–268. https://doi.org/10.1136/mp.50.5.266.
(289) Genes, A.; Edwards, T.; Williams, C.; Teethaisong, Y. 2; Sealey, J.; Sasaki, S.; Hobbs, G.; Cuevas, L. E.; Evans, K. A Highly Multiplexed Melt-Curve Assay for Detecting the Most Prevalent Carbapenemase, ESBL and AmpC Genes. *bioRxiv* **2019**, 842963. https://doi.org/10.1101/842963.
(290) Diercks, A.; Kostner, H.; Ozinsky, A. Resolving Cell Population Heterogeneity: Real-Time PCR for Simultaneous Multiplexed Gene Detection in Multiple Single-Cell Samples. *PLoS One* **2009**, *4* (7), e6326. https://doi.org/10.1371/journal.pone.0006326.